**Laser Diagnostics of Turbulent Flames in High Speed Flows**

By

Nathan Grady

Dissertation

Submitted to the Faculty of the

Graduate School of Vanderbilt University

In partial fulfillment of the requirements

For the degree of

DOCTOR OF PHILOSOPHY

in

Mechanical Engineering

August, 2015

Nashville, Tennessee

Committee:

Robert Pitz, Chair

Joseph Wehrmeyer

Greg Walker

A.V. Anilkumar

Suresh Menon

## ACKNOWLEDGEMENTS

First I would like to thank my advisor Dr. Pitz for his guidance and patience over my tenure as a graduate student, and my Vanderbilt colleagues Marc Ramsay, Carl Hall, and Darren Tinker for tolerating my constant interruptions and questions. I would also like to thank my Georgia Tech colleague Brad Ochs and technicians Chris Ballance and Seth Hutchins for the assistance and company during my lengthy visits in Atlanta.

Financial support for the premixed flame kernel and flow tagging development experiments was provided by the Air Force Office of Scientific Research, Combustion and Diagnostics Program (Chiping Li, Manager) under contract FA9550-12-1-0107/RC657. Financial support for the UV Raman measurements was granted through the summer fellowship research program at Wright-Patterson Air Force Base under the Air Force contractor, Universal Technologies Corporation. Additional financial support was provided by the Air Force Office of Scientific Research, Combustion and Diagnostics Program (Julian Tishkoff, Manager) under contract FA9550-09-1-0205.

Finally, I would like my family for their support and confidence. Thanks Mom, Dad, Michael, Maegan, and Kelly.

**TABLE OF CONTENTS**

## List of Figures

## List of Tables

# CHAPTER 1: INTRODUCTION

Turbulent flames are ubiquitous in combustors, particularly in propulsion devices. Naturally generated turbulence is caused by high Reynolds numbers or fuel-air injection. Additionally, some devices purposefully cause turbulence to increase flame speed and reduce the requisite combustor size. While premixed flames are capable of more efficient and compact combustors, achieving a true premixture in a real combustion device, especially an aerospace propulsion device where mixing time may be limited, may not be feasible and non-premixed modes of combustion are unavoidable. This thesis investigates diffusion flames in complex geometric conditions in an applied study of supersonic combustion, the development of a new diagnostic technique intended for use in flames, and premixed turbulent flames with the absence of any real geometry constraints in a phenomenological study of combustion.

## Phenomenological premixed flame study

Premixed combustion has various advantages over non-premixed combustion: no mixing time, less pollutants, improved fuel economy, and theoretically smaller/lighter combustors thus increasing thrust-to-weight ratios in propulsion systems. Additionally, even in non-premixed combustors there are regions of either partially premixed or fully premixed combustion. However, premixed combustion is subject to flashbacks, auto-ignition and instabilities (all of which can destroy the combustor), and extinction. Furthermore, the occurrence and severity of these instabilities changes with the turbulence level. Therefore the study of turbulent premixed combustion is relevant to all practical combustion and propulsion devices.

Steady flames that are stabilized over a burner or a jet are a common means of studying premixed turbulent flames and a thorough review of these experiments is provided by Driscoll [1]. In general, these burner flames offer nearly unrestricted optical access allowing for an arbitrary number of simultaneous measurements (e.g. temperature, velocity, fluorescent imaging of minor species, etc.). However, the flame properties measured over these burners are geometry dependent [1] and therefore are not universal values. Driscoll [1] attributes these differences between burners due to the flames having a memory of any previous flame front wrinkling that could change downstream conditions (e.g. preheating of reactants, recirculation of products, pilot-flame induced auto-ignition, etc.). Since burners use different stabilization devices (e.g. bluff body, swirl flow, pilot flames, etc.) each burner will induce unique geometry-dependent flame propagation thereby confounding a phenomenological understanding of the interaction between premixed flames and turbulence.

Alternatively, devices known as flame bombs, which use spherically propagating flame kernels are also used to study premixed turbulent combustion. Since flame kernels are neither stabilized nor have mean shear, the use of flame bombs eliminates most geometry dependent effects (for kernels sufficiently smaller than the bomb size [2, 3]). Although geometry-dependence has been removed, flame kernels still have a memory effect due to the relative size differences between the turbulent length scale and intensity, $\ell$ and u' respectively, and the kernel propagation time (i.e. $t_{kernel}/(\ell/u')$) [1, 4]. Nevertheless, this memory effect is only related to turbulent-flame interaction and not to any burner induced effects.

However while flame bombs provide a reliable means of studying flame kernels [3-16], they do have minor drawbacks. Flame bombs are constant volume vessels using fan stirred turbulence. Typically, the fans are in an orthogonal arrangement to increase the homogeneity

of the flow field with the resultant air flow pointing into the vessel (although some experiments reverse the fan direction [15, 16]). This results in a radial mean inflow which would effectively impede flame front propagation especially if the fans are left on (as is the case for Chaudhuri et al. [5-7]). Furthermore since these vessels are constant volume devices, the flame kernels will create a rise in pressure (although some bombs can be considered roughly isobaric [3, 5-7]). Moreover, flame bombs offer limited optical access and diagnostic techniques are usually limited to Schlieren imaging [5, 6, 12] or a single laser sheet [7]. While it may be possible to add more diagnostics to these devices, there are clear limitations to the number of simultaneous measurements that can be made as opposed to burner stabilized flames. Finally, the frequency of flame bomb testing can be very low due to the need to fill the bomb with a homogenous combustible mixture (~5 minutes for flame bomb data comparison [17]) and evacuate the post-combustion mixture (pumped down and filled with air twice before mixtures insertion [17]).

Therefore in this work, a premixed wind tunnel in which flame kernels freely propagate in the mean flow has been developed to alleviate the limitations of flame bombs. My approach generates turbulence via the interaction of a high speed mean flow through either passive or active devices, and therefore doesn't have any mean radial flow component which could potentially impede flame propagation. Furthermore, the tunnel has been designed to have full optical access from all sides allowing for multiple simultaneous diagnostics. Additionally, kernels can be sparked at much higher frequencies than in bombs since the mean flow constantly purges the reacted gases. Repetition rates of 10 Hz are presented in the current work, which is three orders-of-magnitude higher than flame bomb studies. In addition, this apparatus was designed for future studies of freely propagating kernels in supersonic flows to study flame kernel-shock interactions. Typically, shock-kernel interactions have been studied in shock tubes

[18, 19] which have an even slower repetition rate than flame bombs, and have a limited test times to observe shock-kernel interactions.

Previous authors have studied freely propagating kernels with 1) a focus on laser spark ignition [20, 21], 2) at the exit of a fully developed pipe flow [22] that would not produce the homogenous, isotropic turbulence necessary to study phenomenological turbulent premixed flame behaviour, and 3) in 4 m/s mean flows with homogenous, isotropic turbulence generated with passive grids but used spark electrodes that would cause flow inhomogeneities especially in compressible flows [23, 24]. Furthermore, to my knowledge, no freely propagating flame kernel system has systematically compared their turbulent flame speed data to flame bomb correlations, which is necessary to properly compare data between the two systems.

This thesis will present flame kernel data collected over a wide range of turbulent flow fields and mean flow velocities. These results are compared with traditional flame bomb measurements to assess the performance of the wind tunnel, and to determine if this new apparatus can be used to reliably determine the phenomenological behaviour of premixed turbulent flame propagation.

### Non-premixed flames in scramjet combustors

Like ramjets, supersonic ramjets (scramjets) use their forward momentum to compress air instead of doing so mechanically via compressors which become inefficient at supersonic and hypersonic cruising velocities. Unlike ramjets, scramjets do not decelerate the flow to subsonic conditions inside the combustor thus making them more efficient with fewer shock induced total pressure losses. However, this also severely reduces the residence time inside the combustor and makes sustaining/achieving combustion difficult. Since scramjets have low

combustor residence times and poor flame holding capabilities, any realistic combustor needs to address these issues.

While serial experimentation (i.e. the process of making minor improvements each iteration) can optimize certain aspects of scramjet flame holding and design, this process is slow and very expensive. Additionally, such experiments are generally scaled-down versions of actual scramjet designs, and due to the supersonic mixing aspect of these jets, scale-up of these designs isn't trivial. Therefore, there is a need for computational models to design scramjets. The current Reynolds-Averaged Navier-Stokes (RANS) CFD codes used to design scramjet combustors have simplified physics in order to calculate the complex geometry with detailed chemistry and unsteady compressible turbulent flow. While these models generally provide guidelines for future experimental efforts, they fail to capture the phenomenological flow patterns. Therefore, the use of large-eddy-simulations (LES), which promise to give improved prediction of turbulent combustion [25, 26] in supersonic flows [27], have been proposed. LES simulations are more computationally efficient than direct numerical simulations (DNS) because they directly compute only the large scale features that contain the bulk of the kinetic energy and dominate the overall flow. LES models require subgrid closure methods to predict events that occur below the grid resolution for momentum, energy, and scalar transport.

In order to verify the ability of these numerical models to predict turbulence-chemistry interaction, *in situ* and temporally resolved experimental measurements of temperature and species are needed in compressible flows with realistic combustors. In this thesis, UV spontaneous Raman scattering measurements in a Mach 2 air flow over a ramp-closeout wall-cavity flame-holder fueled from the ramp are presented. Mean, RMS fluctuation, and scatter plots of temperature, species concentration, and mixture fraction are discussed. In addition, analysis of local fuel consumption and product formation is provided.

**Development of a velocimetry technique for turbulent flames**

Both Particle Imaging Velocimetry (PIV) and Molecular Tagging Velocimetry (MTV) have been successful in obtaining quantitative velocity measurements in an array of flow fields. PIV particles are easily tracked by strong particle light scattering giving PIV higher spatial resolution than MTV grids that are tracked by molecular fluorescence. However, the ability of PIV particles to follow the gas velocity may be inhibited by shock waves, thermophoretic effects, and seeding non-uniformities [28, 29]. In addition, PIV particle seeding can cause rapid obscuration of test section windows and damage the experimental apparatus [30, 31]. Therefore, MTV methods which track the flow velocity with molecular grids have been developed for experiments where the application of PIV is not practical [32].

One issue that has plagued unseeded MTV is obtaining usable signal-to-noise ratios in hot gas or combustion regions where there may be high backgrounds of the chosen tracer, insufficient quantities of the write molecule, or other interferences. For example in conventional hydroxyl tagging velocimetry (HTV), an ArF laser photodissociates $H_2O$ into ground state grid of OH (v=0) that may be obscured in high temperature flames by naturally occurring background OH [33]. In laminar flames or in environments that are highly repeatable, a mean image without the write laser can be subtracted from a mean image with the write laser to obtain mean velocity data. However, mean data are often insufficient in turbulent flames and single-shot data are required to obtain instantaneous velocities. This thesis details a new MTV technique that can obtain measurements in turbulent premixed and non-premixed combustion.

# CHAPTER 2: PREMIXED TURBULENT FLAME KERNELS

In this section the experimental results for freely propagating, premixed flame kernels from two different configurations will be presented for subsonic incompressible turbulent flows ($M \leq 0.3$).Two different turbulence generation techniques are presented, and the turbulent flow fields and resultant flame propagation they produced are compared with traditional flame bomb measurements. First, a brief overview of premixed flame phenomena will be provided, followed by a description of the turbulent flame properties that were measured. Then the experimental results will be given for 1) a large-scale, anisotropic turbulent flow field and for 2) small_+scale, isotropic turbulent flow.

While some basic relations between turbulence and flame propagation were observed for the large-scale, anisotropic case, the length scales present in these experiments were unable to effectively wrinkle the flame front thereby reducing the flame speeds below flame bomb correlations. Additionally, the length scales and turbulence intensities could not be independently varied further complicating the data analysis and preventing a systematic study of turbulent premixed flames. However, when the kernels were observed in the small-scale, isotropic flow field, flame propagation rates followed similar trends with data taken from non-propagating kernels (i.e. in flame bombs) and correlated well with slow speed ($M < 0.1$) data thereby demonstrating the capability of the current system to supplement and/or replace traditional flame bomb measurements.

## Premixed flames background

### Regime diagram

The different regimes of turbulent premixed combustion have been of interest to researchers for decades [1, 34-36]. These regimes of turbulent premixed combustion have been identified theoretically as seen in Figure 1 (known as a Borghi plot) using the revisions developed by Peters [35] where the effects of normalized turbulence and integral length scale are plotted. Here, flames can be visualized as planar sheets which are then perturbed by turbulence. A brief overview of the reasoning behind the different regimes in this plot will be given here. Then, experimental and numerical observations will be discussed to indicate where the assumptions of the Borghi plots fail and highlight the active areas of research.

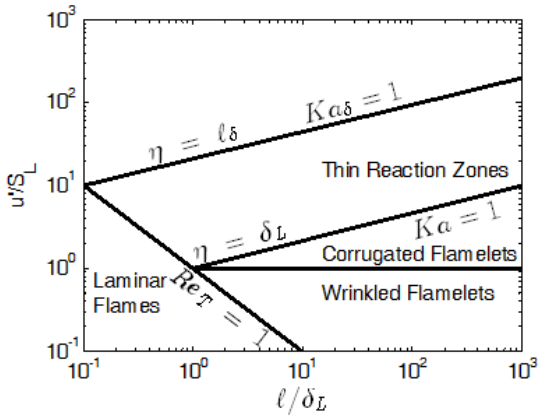


Figure 1: Borghi plot as refined by and found in Peters [35] showing the various regimes of turbulent premixed combustion.

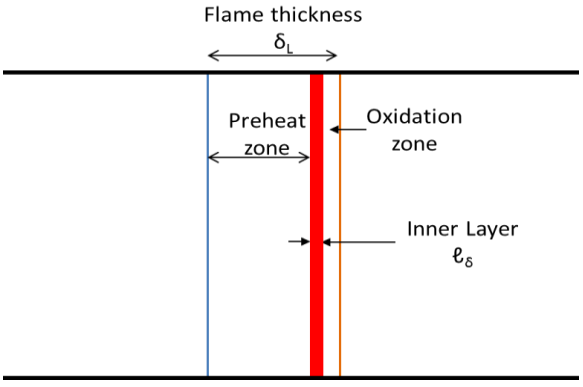


Figure 2: Schematic of the flame zone thickness, $\delta_L$, and sub-layers including $\ell_\delta$.

Laminar flames are those which do not exhibit any wrinkling and/or thickening of the flame, and are defined by the region where the turbulent Reynolds number ($Re_T$) is less than one, where $Re_T$ is defined as:

$$Re_T = \frac{u'\ell}{\nu} \quad (1)$$

Here u' is the RMS velocity fluctuations, $\ell$ is the integral length scale of the turbulence (i.e. characteristic turbulent eddy size), and v is the kinematic viscosity of the unburned gas. The laminar flame thickness, $\delta_L$ is defined as:

$$\delta_L = \frac{D}{S_L} = \frac{\nu/Sc}{S_L} \quad (2)$$

where D is the molecular diffusivity, $S_L$ is the laminar flame speed, and Sc is the Schmidt number ($Sc = \nu/D$).

However, for $Re_T > 1$, the turbulent flame interactions can be divided into two cases: 1) where the flame front is locally laminar but wrinkled, and 2) the local flame front is distorted by turbulence (i.e. the different layers/zones shown in Figure 2 are no longer parallel). It is assumed for the current discussion that eddy size is smaller than the overall flame front length (which may not be true for flame kernels). The simpler of these two cases, known as the flamelet regime, is the result of global wrinkling of the flame front but locally the flame front propagates in a quasi-steady state at $S_L$ in the form of flamelets. The flamelet regime is defined for Karlovitz number (Ka) less than one. For laminar flames, Ka is defined as:

$$Ka = \frac{K}{S_L/\delta_L} = \frac{u'/\ell_T}{S_L/\delta_L} \quad (3)$$

where K is the stretch rate. For turbulent flames (r.h.s. of Equation 3), the stretch rate can be calculated using the turbulence intensity and the Taylor's length scale, $\ell_T$:

$$\ell_T = \left(\frac{\nu}{u'/\ell}\right)^{1/2} \quad 4$$

Using the definition suggested by Driscoll [1], Ka can be expressed in terms that are either known or rely only on the measured velo city fluctuations by assuming unity Lewis number (Le = α/D) and thermal diffusivity, α, scaled by the average temperature $\alpha_{avg} = \alpha_{300K}[(T_P+T_R)/2/300K]^{3\backslash 2}$:

$$Ka = \left(\frac{u'}{S_L}\right)^{3/2} \left(\frac{S_L \ell}{\alpha_{300K}}\right)^{-1/2} \left(\frac{(T_P + T_R)/2}{300K}\right)^{-3/2} \quad 5$$

where $\alpha_{300K}$ is the thermal diffusivity at 300 K (the value of 0.15 $cm^2/s$ for $N_2$ at 300 K is suggested [1]).

Alternatively, the upper limit of the flamelet regime ($Re_T > 1$, Ka <1) can be defined when the Kolmogorov scale, η, is commensurate with the flame thickness (i.e. $\eta = \delta_L * Sc^{1/2}$). The Kolmogorov scales represent the smallest, least energetic eddies in the turbulent energy spectrum and these scales are quickly dissipated by viscosity. Since $Sc^{1/2} \approx 1$ for most mixtures, unity Schmidt number is assumed by most authors and will be used in the current explanation (and as a result the limit of the flamelet regime can be defined as $\eta = \delta_L$). As can be seen in the Borghi plot, the flamelet regime is split into two sub-regimes called wrinkled flamelets (WF) with $u' < S_L$ and corrugated flamelets (CF) with $u' > S_L$. To conceptualize this difference, u' is treated as the circumferential velocity of largest eddies. In the WF, the laminar propagation of the flamelets is faster than the turbulent eddy circulation and hence the wrinkling process. Therefore, in this sub-regime flame propagation tends to smooth out the wrinkles induced by

turbulence. In the CF sub-regime, the eddy velocity is faster than $S_L$ thus creating large distortions which can result in pockets of unburned reactants. In this regime, the primary effect of turbulence is to increase the laminar flame surface area, $A_L$, to some higher value turbulent flame surface area, $A_T$, on account of the wrinkling. Since the flamelets locally propagate at $S_L$, the resultant turbulent flame speed, $S_T$, must be proportional to the increase of area as a result of the wrinkling (i.e. $A_T/A_L$).

To describe the final two regimes, a more detailed description of a flame surface is required and is shown in Figure 2. The flame zone thickness, $\delta_L$, is comprised of three separate zones: 1) preheat zone indicative of a chemically inert temperature rise in the reactants, 2) an inner layer where reactants are consumed by radicals, and 3) an oxidation layer where the final products (namely $H_2O$ and $CO_2$) are formed. The existence of these layers becomes important when $\eta \leq \delta_L$ (i.e. $Ka \geq 1$) and small turbulent eddies are able to "penetrate" the flame zone.

In the thin reaction zone regime (TRZ), eddies are capable of penetrating the preheat zone of the flame front but not the inner layer. The zone is bounded by $Ka > 1$ and $Ka_\delta < 1$ (where $Ka_\delta = Ka*.01$), or alternatively $\delta_L > \eta > \ell_\delta$ where $\ell_\delta$ is the thickness of the inner layer. The inner layer is usually expressed as a function of $\delta_L$ in the form of:

$$\ell_\delta = \delta_L * \delta \qquad 6$$

where $\delta \sim 0.1$ as estimated by Peters [35]. Therefore, eddies in the TRZ are capable of penetrating and broadening the preheat zone but not the inner reacting layer. As a result of this preheat zone broadening, the layers shown in Figure 2 are no longer parallel and the quasi-steady state assumptions are no longer valid. The final regime indicated on the Borghi plot is the distributed reaction zone regime (DRZ) where $Ka_\delta > 1$. In this regime, eddies can penetrate

into the reacting inner layer and result in either “shredded flamelets/flame front” or a “well stirred reactor”.

However, recent experiments [1] investigating the so-called DRZ regimes have not observed the shredding of the flame fronts. Additionally, while numerical results indicate that preheat zone broadening and distributed reactions do occur [37-39], they happen at higher turbulence intensities than indicated on the Borghi plots. The conclusion of these experiments, is that heat release from the flame front results in an increase in viscosity and thermal expansion both of which attenuate the eddies at or near the Kolmogorov scale. Therefore, the small scale structures/eddies theorized to break apart the reaction zone don’t have sufficient energy to survive in either the preheat or reaction zones.

**Markstein number and curvature effects on flame propagation**

Even in the absence of turbulence, flame speeds can be affected by the flow field due to either curvature or aerodynamic strain (i.e. flame stretch). The effects of curvature and strain on the flame surface are a mixture specific property and can be characterized by the Markstein number (Ma):

$$Ma = \frac{\delta_M}{\delta_L} \qquad 7$$

where $\delta_M$ is the Markstein length and $\delta_L$ is the laminar flame thickness. Here, a flame is said to have positive curvature if it is convex towards the reactants and *vice versa* for negative curvature. For mixtures with positive Markstein lengths, negative curvature propagates faster than positive curvature as shown in Figure 3. This flame speed enhancement in negative curvature regions results in the closure of flame wrinkles effectively decreasing turbulence

flame speed. Furthermore, this dissipative flame wrinkling effect is stronger for higher values of Markstein length.

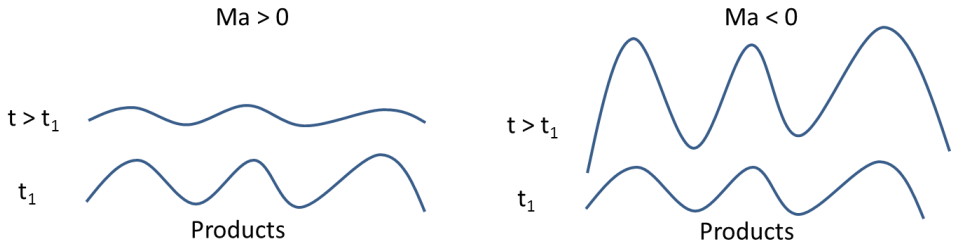


Figure 3: Markstein effects on flame curvature and topology

The effects of curvature on laminar flame speed was first proposed by Markstein [40] with a simple linear approximation:

$$S_L = S_{L,0}(1 - \delta_M \kappa) \qquad 8$$

where $S_{L,0}$ laminar flame speed at zero curvature and stretch, and κ is the curvature of the flame front. In Equation 8, $\delta_M$ is not a physical length, but a parameter to account for the effects of curvature (which is in units of 1/m) on flame speed (which is in units of m/s). As shown by other authors [6, 41], the $\delta_M$ is proportional to both thermal expansion, which is a function of stoichiometry, and the Lewis number, Le = α/D (~1 for $CH_4$-air mixtures), which accounts for nonequidiffusion of heat and species. The curvature dependence, in part, can be explained by Le effects due to the focused diffusion of temperature and minor species (which have a different Le than the fuel) in negative curvature regions. The effects of both stretch and curvature on flame speed can be combined into a single equation using both the Ma and Ka as shown in Equation 9.

$$S_L = \frac{S_{L,0}}{1 + MaKa} \quad (9)$$

As can be seen in Equation 9, for positive Markstein numbers any stretch (i.e. positive Ka) will reduce the laminar flame speed.

Typically, $\delta_M$ derived from flame speed measurements of laminar flame kernels that have a known stretch rate of (2/R)dR/dt. The measured flame speeds are then extrapolated to a theoretical zero-stretch condition to calculate $\delta_M$. However, the assumptions used in this extrapolation (i.e. linear or nonlinear) affects the calculated value of $\delta_M$. In general, the values in Table 2 from Halter et al. [41] that use a nonlinear approximation are used, however, a comparison with linearly approximated values of $\delta_M$ from Aung et al. [42] is also shown.

**Relevant turbulent premixed flame quantities of interest**

Of primary interest to premixed turbulent combustion is the turbulent flame speed, $S_T$, as a function of turbulence [43] . $S_T$ is one of the main quantities measured in most experimental papers. Unfortunately, there is no one definition of turbulent flame speed and three different variations have been developed. For consistency with the literature the definitions found in Driscoll [1] will be used:

$S_{T,GC}$ = Global consumption speed = $\frac{\dot{m}_R}{\rho_R A_{\bar{c}=0.5}}$ (10)

$S_{T,C}$ = Local consumption speed = $S_L I_0 \int FSD dn \propto FSD_{max}\delta_T$ (11)

$S_{T,D}$ = Global displacement speed $\alpha$ dR/dt (12)

where $\dot{m}_R$ is the mass flow of the reactants, $\rho_R$ is the density of the reactants, $A_{\bar{c}=0.5}$ is the area of the $\bar{c}$ = 0.5 contour defined below, FSD is the flame surface density (area of the flame surface per volume), and $\delta_T$ is the (turbulent) flame thickness. These values of turbulent flame speed

are not necessarily equal; in fact, they frequently are not equal. The global consumption speed is only viable when all of the reactants travel through the flame zone such as in a Bunsen burner which is not the case for flame kernels and most other burners. Therefore, the rest of the paper will primarily use the latter two definitions. $S_{T,D}$ is defined as the relative growth rate of the kernel and is a function of time and radius due to the self-accelerating nature of spherical flames. $S_{T,C}$ is intrinsically related to the actual reaction rate/consumption of reactants, and as a value of the local flame speed is independent of either the radius or time so long as $R_{kernel} > \ell$ (i.e. all of the turbulent length scales are able to wrinkle the flame front).

It should be noted that these two velocities are determined relative to different locations in the flame front defined by the mean progress variable c:

$$c = \frac{T - T_R}{T_P - T_R} \tag{13}$$

where $S_{T,D}$ is defined relative to c = 0.1 and $S_{T,C}$ is defined at the maximum value of FSD which is usually around c = 0.5. In Equation 13, T is the temperature, $T_R$ is the reactant temperature, and $T_P$ is the product temperature.

There have been multiple different formulations used to correlate $S_T/S_L$ to $u'/S_L$, however, in general it is believed that as the turbulence intensity increases so does the turbulent flame speed. While there have been attempts to correlate flame speeds across all types of flames [4, 35, 43] as shown in Figure 4, these correlations aren't well suited for spherical flames for two primary reasons: 1) spherical flames are known to accelerate with respect to time even in laminar cases due to hydrodynamic instabilities [44] while most correlations assume a steady burning rate, and 2) flame kernels are only affected by the turbulence length scales which can fit inside them while all larger scales merely convect the kernel and don't create an increase in flame surface area. This scale dependence reduces the

total turbulence energy of a flow field to an “effective turbulence energy” as shown in Figure 5. A correlation which accounts for the self-accelerating nature of flame kernels is also shown in Figure 4.

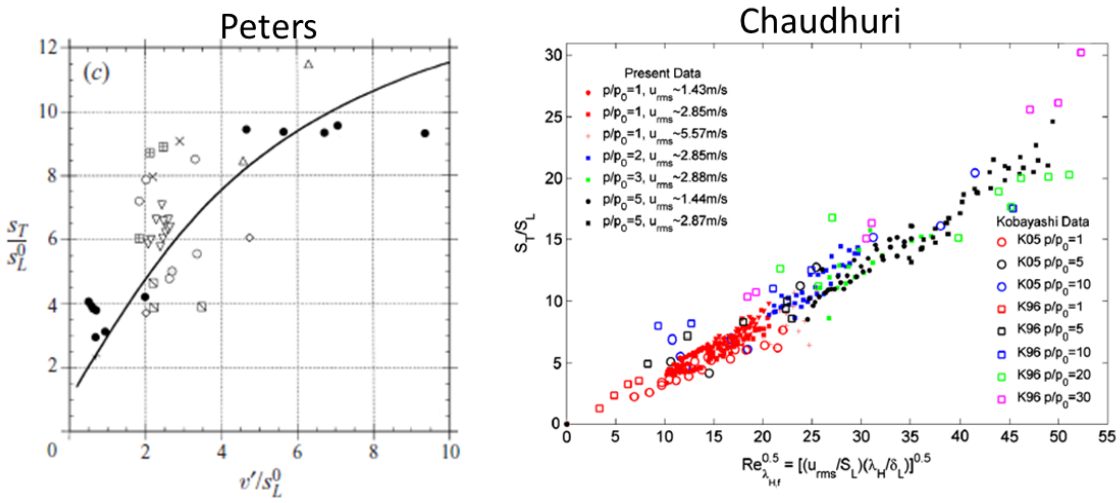


Figure 4: Typical turbulent flame speed correlation by Peters [35] (left), and spherical correlation by Chaudhuri et al. [5] (right).

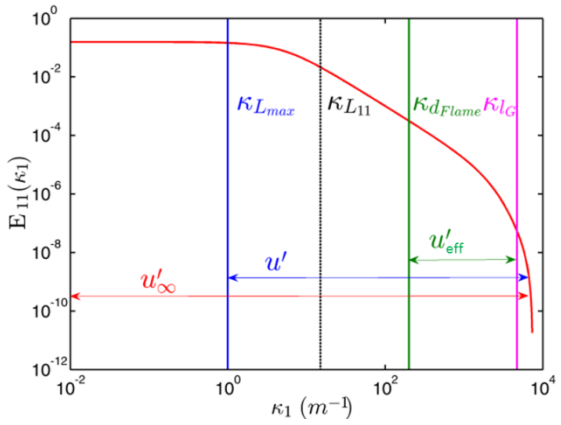


Figure 5: Comparison of total turbulence energy, u’, to effective turbulence energy, u’$_{eff}$.

## Experimental systems

The following section details both the turbulence generators and the wind tunnel facility used to observe freely propagating flame kernels. Pre-nozzle passive grid, and blown grid turbulence generation descriptions and experimental results are provided in Appendix A.

### Vane grid generation: large-scale anisotropic turbulence

The tunnel configuration used for the large-scale anisotropic turbulence is shown in Figure 6. Pressurized air enters into a settling chamber and is connected to the test section with a fuel mixing and turbulence generation section. Fuel was injected upstream of the turbulence generation (described below) to ensure proper mixing, and flow conditioners are installed between these two elements so that turbulence in the test section was a function of the generation section and not affected from any potential upstream sources. The facility supplied a steady stream of natural gas (mainly $CH_4$) up to ~0.1 kg/s. After turbulence generation, the flow was accelerated to compressible conditions via a 9.3:1 area ratio nozzle with a 5 cm x 5 cm constant area test section. After the nozzle, laser ignition was used to create the flame kernel before entering the optically accessible test section.

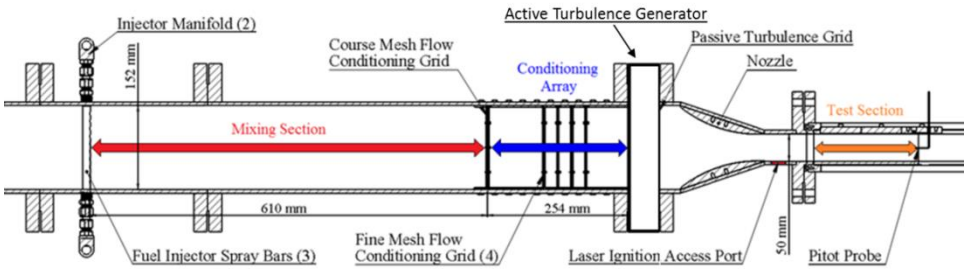


Figure 6: Schematic of wind tunnel facility with the active turbulence generator shown.

A vane grid generator as shown in Figure 7 [45-49] was used in place of the blown grid (see Appendix A) to: 1) to eliminate the need to match the equivalence ratio between the main flow and the jets, and 2) increase flow homogeneity. For each of the turbulence generation schemes, determination of the flow/turbulence properties (e.g. $\bar{u}$, $u'$, $\ell$, etc.) were determined *via* hot wire anemometry using a Constant Temperature Anemometry (CTA).

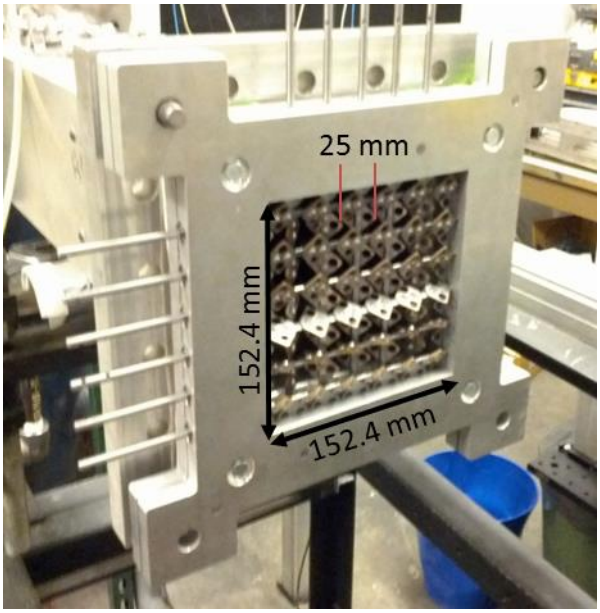


Figure 7: Picture of the vane stirred turbulence generator.

**Small-scale isotropic turbulence**

Since the previous turbulence schemes used pre-nozzle generation, any turbulence they generate is susceptible to stretching in the longitudinal direction the nozzle [50]. This causes very large scales in this direction, and highly energetic scales in the orthogonal direction thus yielding anisotropic turbulence with length scales larger than the tunnel width. Therefore, to produce small scale isotropic turbulence, a post-nozzle passive grid (PNPG) turbulence generation scheme was implemented. Previous authors who tested passive grids in

compressible or near compressible flows [49, 51] found that a higher solidity can increase turbulence; however, high solidity grids can also result in inhomogeneous turbulence occurring at a solidity ratio of 40-50%. Therefore, for the current studies a solidity ratio of 38% was chosen with a hole diameter of ~3 mm. A picture of this generator and its location in the tunnel are shown in Figure 8.

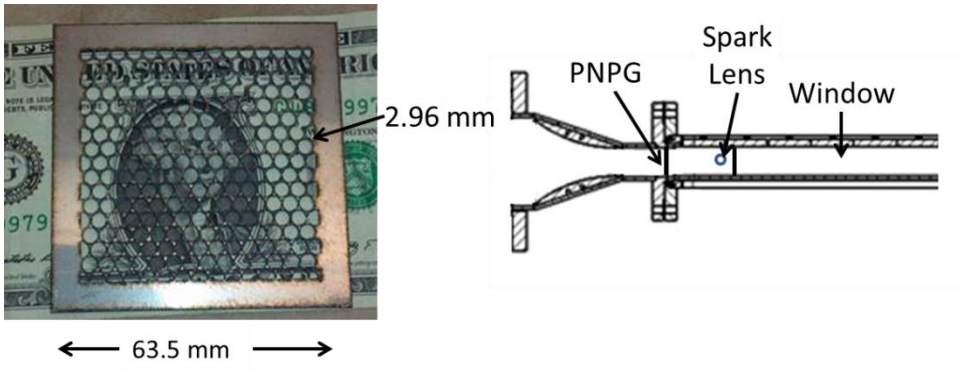


Figure 8 : Picture of post-nozzle passive grid (PNPG, left) and location in tunnel (right).

**Comparison of turbulent flow properties**

For easy reference, the turbulent parameters used in this study will be presented below in Table 1 [52] with laminar flame properties provided in Table 2. The data for the pre-nozzle passive grid and blown grid (see Appendix A) are also included in these tables.

Table 1: Comprehensive table of turbulence conditions for different turbulence generators

| | | Pre-Nozzle Passive Grid | | | Blown Grid (Low and High blowing) | | | |
|---|---|---|---|---|---|---|---|---|
| M | | 0.1 | 0.2 | 0.3 | 0.2 L | 0.2 H | 0.3 L | 0.3 H |
| u' (m/s) | | 0.27 | 0.6 | 0.92 | 4.1 | 4.2 | 10.2 | 8.5 |
| $\ell$ (mm) | | N/A | N/A | N/A | 29.4 | 36.4 | 384 | 155 |
| $u'/S_L$ | $\phi = 1.0$ | 0.675 | 1.5 | 2.3 | 10.2 | 10.5 | 25.5 | 21.2 |
| $\ell/\delta_L$ | $\phi = 1.0$ | N/A | N/A | N/A | 49 | 60.7 | 640 | 258 |

Table 1 continued

| | | Vane Grid | | | Post-Nozzle Passive Grid | | |
|---|---|---|---|---|---|---|---|
| M | | 0.1 | 0.2 | 0.3 | 0.1 | 0.2 | 0.3 |
| u' (m/s) | | 0.4 | 0.9 | 2.0 | 0.6 | 1.0 | 1.8 |
| ℓ (mm) | | 3.5 | 10.2 | 80.9 | 3 | 3 | 3 |
| $u'/S_L$ | $\phi = 1.0$ | 1 | 2.25 | 5 | 1.5 | 2.5 | 4.5 |
| | $\phi = 0.7$ | N/A | N/A | N/A | N/A | 5 | 9 |
| $\ell/\delta_L$ | $\phi = 1.0$ | 5.83 | 17.0 | 135 | 5 | 5 | 5 |
| | $\phi = 0.7$ | N/A | N/A | N/A | N/A | 3 | 3 |

Table 2: Laminar flame properties

| | $\phi$ | |
|---|---|---|
| | 0.7 | 1 |
| $S_L$ (cm/s) | 20 | 40 |
| $\alpha_{c=0.5}$ ($cm^2/s$) | 1.98 | 2.38 |
| $\delta_L$ (mm) | 0.99 | 0.6 |
| $\delta_M$ (mm) [17, 41] | 0.355 | 0.64 |
| Ma = $\delta_M/\delta_L$ [41] | 0.36 | 1.09 |
| Ma [42] | 0.01 | 1.3 |

The laminar flame thicknesses are determined using the thermal diffusivity of the mixture at $T_{c=0.5}$, $\alpha_{c=0.5}$, as shown in Equation 14:

$$\delta_L = \frac{\alpha_{c=0.5}}{S_L} \qquad 14$$

The Markstein numbers for are calculated using the $\delta_L$ values described in Equation 14, and the Markstein lengths determined experimentally by Halter et al. [41].

A comprehensive regime diagram plot is also provided in Figure 9. The extra data point labeled "Large Duct" will be discussed after the PNPG data.

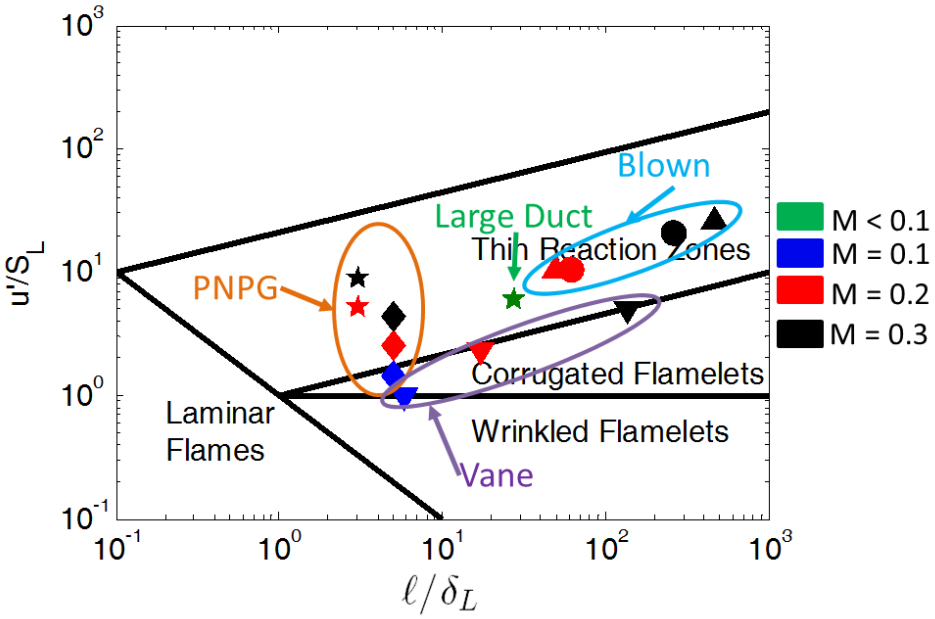


Figure 9: Comprehensive reigme diagram plot of all cases studied.

**Analysis of PLIF data**

Some marker of the flame zone/edge needs to be acquired in order to determine accurate measurements of flame speed, surface density, and thickness. To measure the flame edge, various laser diagnostics have been used to accomplish this using Rayleigh scattering for temperature profiles [53-55] and Mie scattering using oil droplets [9, 56]. Other experiments determined the flame edge with fluorescence imaging of a radical such as CH [57], $CH_2O$ [53], and OH [56, 58-60]. For the current experiment, OH PLIF was chosen to study the effects of turbulence and a schematic of experimental configuration is shown in Figure 10. For the high turbulence intensity cases, the OH PLIF measurements are combined with $CH_2O$ PLIF as described by [53] to ensure there was no local flame extinction.

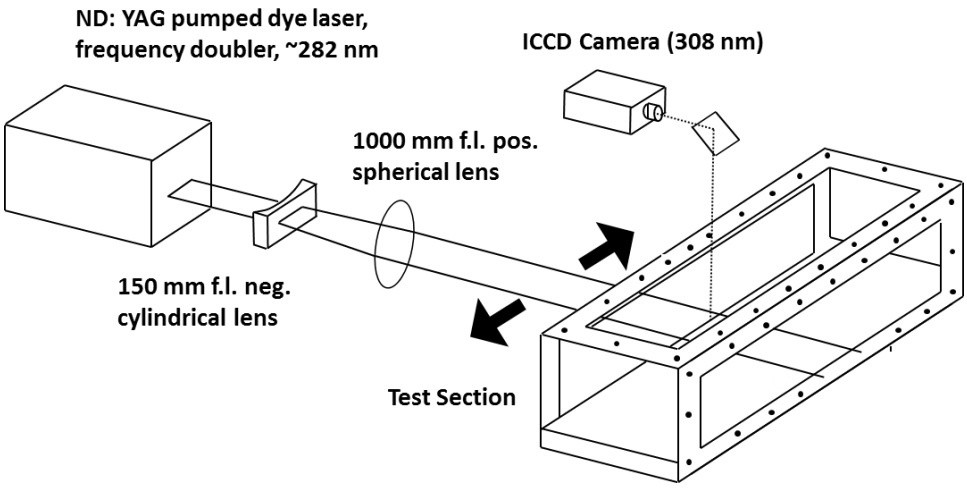


Figure 10: Schematic of OH PLIF diagnostic system where the bold double arrows indicate that the OH PLIF system can be moved in the streamwise direction of the wind tunnel.

The process of determining flame edge from OH images is described in numerous sources [56, 58-61]. Once this flame edge has been found, each image is "binarized" with the value of either 0 or 1 being given to the unburned or burned side respectively. Then each of these binarized images are averaged together thus producing a "c-map" with equidistant bins. From this c-map both flame surface density and turbulent flame speed can be derived. Since the kernels are convected by scales larger than their diameter at early times, the binarized images are centered on each frame to isolate convection from turbulence-flame interaction. With the exception of the blown grid studies, the transverse length scales were small so movement out of the PLIF sheets was negligible. For the blown grid PLIF measurements, a second orthogonal camera had to be used to determine out-of-plane motions to condition the data.

The radius for each c-map is determined by :

$$R = \sqrt{A/\pi} \qquad 15$$

The flame surface density (FSD) was approximated with a 2D dimensional representation, labeled FSD, using the c-map as mentioned in Shepherd and Cheng [56] :

$$FSD(\bar{c}) = \frac{1}{n_f}\frac{L(\bar{c})}{A(\bar{c})} \qquad 16$$

where L(c̄) and A(c̄) are functions of the flame length and area as a function of c̄ respectively, and $n_f$ is the number of images used. A(c̄) is determined directly from the number of pixels for each bin and the area of each pixel. L(c̄) is determined by the length of flame edge in each c-map bin added across all the images (i.e. $n_f$). A schematic of this process is provided in Figure 11. Finally, the flame zone thickness can be defined by:

$$\delta_T = \frac{1}{(dc/dn)_{max}} \qquad 17$$

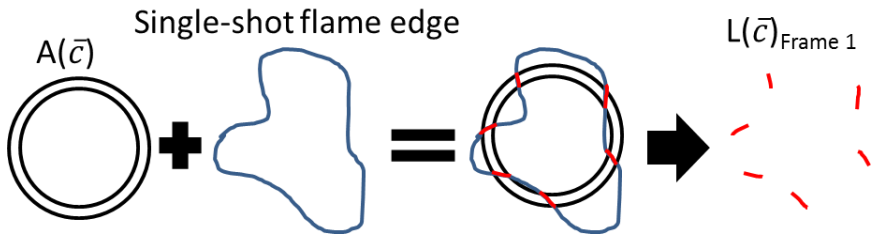


Figure 11: Schematic of FSD determination from c̄-maps for a given progress variable bin.

$S_{T,D}$ is determined from dR/dt where R(t) is the flame position. Knowing dR/dt, $S_{T,D}$ can be calculated using the velocity induced by thermal expansion ($u_{TE}$). By continuity, thermal expansion can be calculated from the wave frame with the following equation:

$$\rho_P \frac{dR}{dt} = \rho_R(S_{T,D}) = \rho_R\left(\frac{dR}{dt} - u_{TE}\right) \qquad 18$$

where the subscripts P and R represent the values of the products and reactants respectively. Solving for $u_{TE}$ yields the following equation:

$$u_{TE} = \frac{dR}{dt}\left(1 - \frac{\rho_P}{\rho_R}\right) \quad (19)$$

Finally, $S_{T,D}$ in the lab frame can be calculated:

$$S_{T,D} = \frac{dR}{dt} - u_{TE} = \frac{dR}{dt}\frac{\rho_P}{\rho_R} \quad (20)$$

The flame edge curvature statistics are also shown. Unlike the derived measurements described previously, curvature measurements can be made from single-shot images. These measurements have been made using OH PLIF by others [58, 59]. Curvature is defined by:

$$h_{xy} = \frac{(\dot{x}\ddot{y} - \dot{y}\ddot{x})}{(\dot{x}^2 + \dot{y}^2)^{3/2}} \quad (21)$$

To find the curvature, the flame edge was smoothed to remove the effects of pixelization, and divided into small segments to determine local curvature. Polynomial fits for both the x and y image coordinates were made for each of the flame edge segments. Previous authors recommend the use of 13 points along the flame edge [59] to obtain consistent results across various turbulence intensities.

**Effects of mean flow velocity and flow choking due to heat addition**

If the range of kernel propagation time is limited to only those kernels small enough to have negligible flame-tunnel effects, then the kernels should propagate in an isobaric flow field.

However, initial kernel spark testing in the tunnel demonstrated potential mean flow effects on flame kernel development as shown in Figure 12. This series of images was taken for a test case of M = 0.2 and $\phi$ = 1, which resulted in sufficient turbulence/heat release to cause

the flow to choke and the resultant pressure spike caused the windows to blow out. Prior to this test, cases with less turbulence and heat release (M = 0.1/$\phi$ = 1 and M = 0.2/$\phi$ = 0.7) did not result in such a blowout. Therefore, it is suggested that 1D flow with heat addition caused a rise in pressure and the flow to choke clearly demonstrating that some effects of mean flow velocity can exist. However, this result was primarily caused by the overall length of the tunnel test section (76.2 cm) which allowed sufficient residence time for the kernel to occupy a large portion of the wind tunnel and created a significant heat addition to the flow. Therefore, the overall length of the tunnel was reduced to 30 cm to prevent window damage.

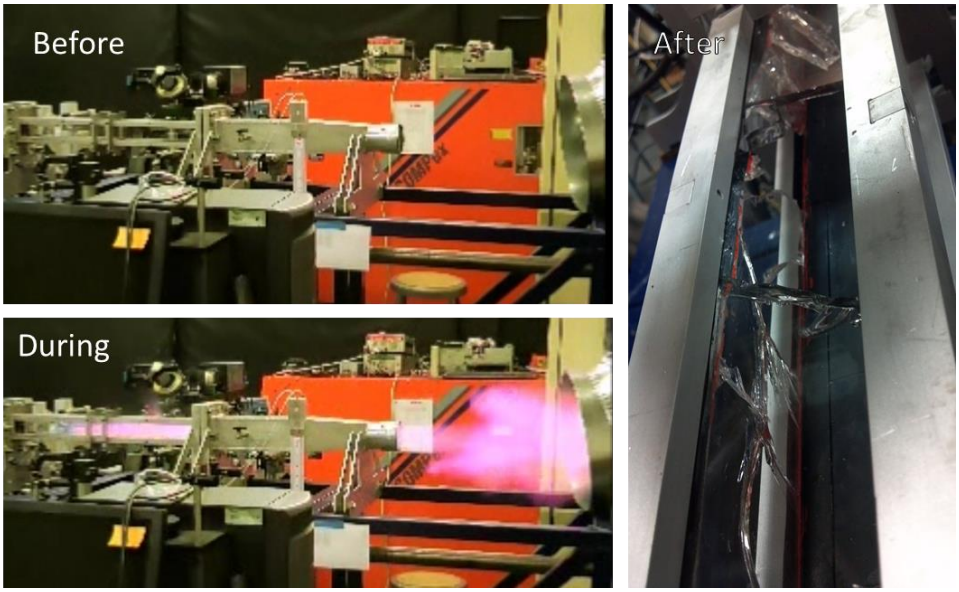


Figure 12: Time series of tunnel blowout due to resultant pressure rise from 1D flow with heat addition.

**Anisotropic, large-scale turbulence: Vane grid**

While the results of the pre-nozzle passive grid and blown grid systems are described in Appendix A, the following is a brief summary to provide perspective and motivation for the vane grid experiment. Repeatable ignition of spherically propagating flame kernels was achieved, and active turbulence generation was achieved. However, it was found that the blown grid

produced scales much larger than tunnel width and most of the turbulent energy was unable to wrinkle the flame front. Therefore, a new turbulence generation scheme was needed which produced smaller scales.

Further research was done using the vane grid turbulence generator and combined $CH_2O$/OH PLIF. In order to obtain the requisite 355 nm light for $CH_2O$ PLIF, the Continuum Surelite previously used to make the spark was repurposed by adding a third harmonic crystal. A Spectra Physics Nd:YAG laser (~10-12 mJ/pulse at 532 nm after focusing lens) was used to ignite the flame kernels. It should be noted that the laser energy is ~30% greater than the laser energy used in the blown grid studies (see Appendix A) due to differences in laser beam quality. The $CH_2O$ fluorescence was imaged on a PI-MAX 2 ICCD camera with a delay of ~100 ns relative to the OH PLIF camera. To ensure consistent triggering between the two cameras, the output of the OH PLIF camera was used to trigger the $CH_2O$ camera. This triggering scheme resulted in a ~100 ns delay between the two cameras. The raw OH/$CH_2O$ images are then dewarped to account for any perspective distortion and translated to ensure that each pixel has the same physical size (~72.5 µm x 72.5 µm square) and location. A schematic of the revised experimental configuration is shown in Figure 13.

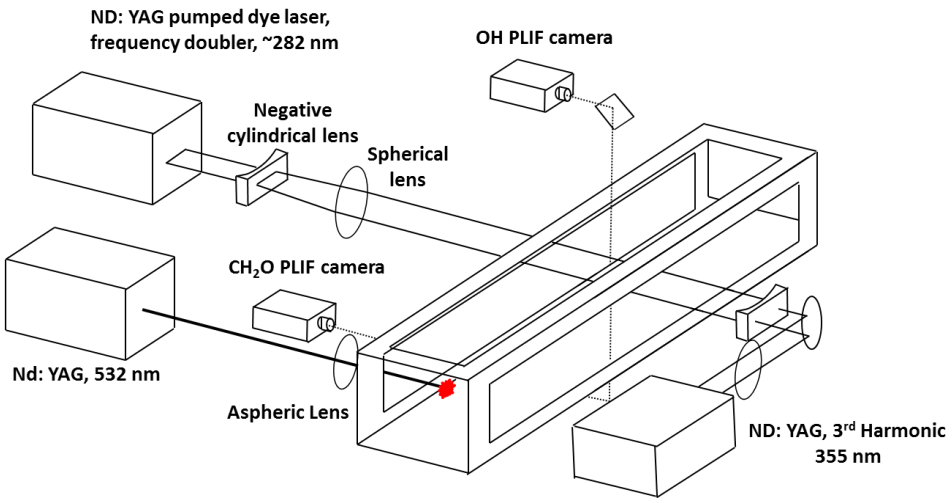


Figure 13: Schematic of $CH_2O$/OH PLIF and laser ignition system

Turbulence data was taken using hot wire anemometry (CTA), and the results for the three Mach numbers used are shown in Figure 14:. Due to vortex stretching in the nozzle [50], the turbulence is highly anisotropic in the test section with the streamwise component, $u_{RMS}$, being ~25% of the other components in the M = 0.3 case and ~40% at M = 0.1. The streamwise component increases slowly in the streamwise direction due to the tendency of the turbulence to return to isotropy. The square root of the turbulent kinetic energy, k, is also shown in Figure 14: and shows a slow decay of the overall turbulence. The values for $k^{1/2}$ were 0.67, 1.5, and 3.8 m/s ($u'/S_L$ = 1.68, 3.75, and 9.5 respectively for $S_L$ = 40 cm/s) for the M = 0.1, 0.2 and 0.3 cases respectively. While the turbulence intensities are lower than the blown grid, the length scales for the vane grid are much smaller for all Mach numbers allowing for more of the turbulent scales to wrinkle the flame front.

Stoichiometric kernels were observed at three different M = 0.2 and 0.3 at 5 streamwise locations and M = 0.1 at two different locations to achieve similar kernel propagation times for the three different mean flows. Only two locations are shown at M = 0.1 since the kernel takes

~3.5 ms to enter the camera's field of view at upstream location and begins to have significant wall interactions after ~4.5 ms. Raw images for the two PLIF systems are shown in Figure 15. In general there was a continuous $CH_2O$ layer around the OH indicating that local extinctions were rare events. Broadened regions of $CH_2O$ were generally between folds in the kernel although there were regions where preheat zone broadening was apparent such as the rightmost $CH_2O$ image in Figure 15. Given the measured turbulence levels and since there is little evidence of local extinction, local extinction was assumed negligible. Therefore, the results presented here focus on data from the OH PLIF images only.

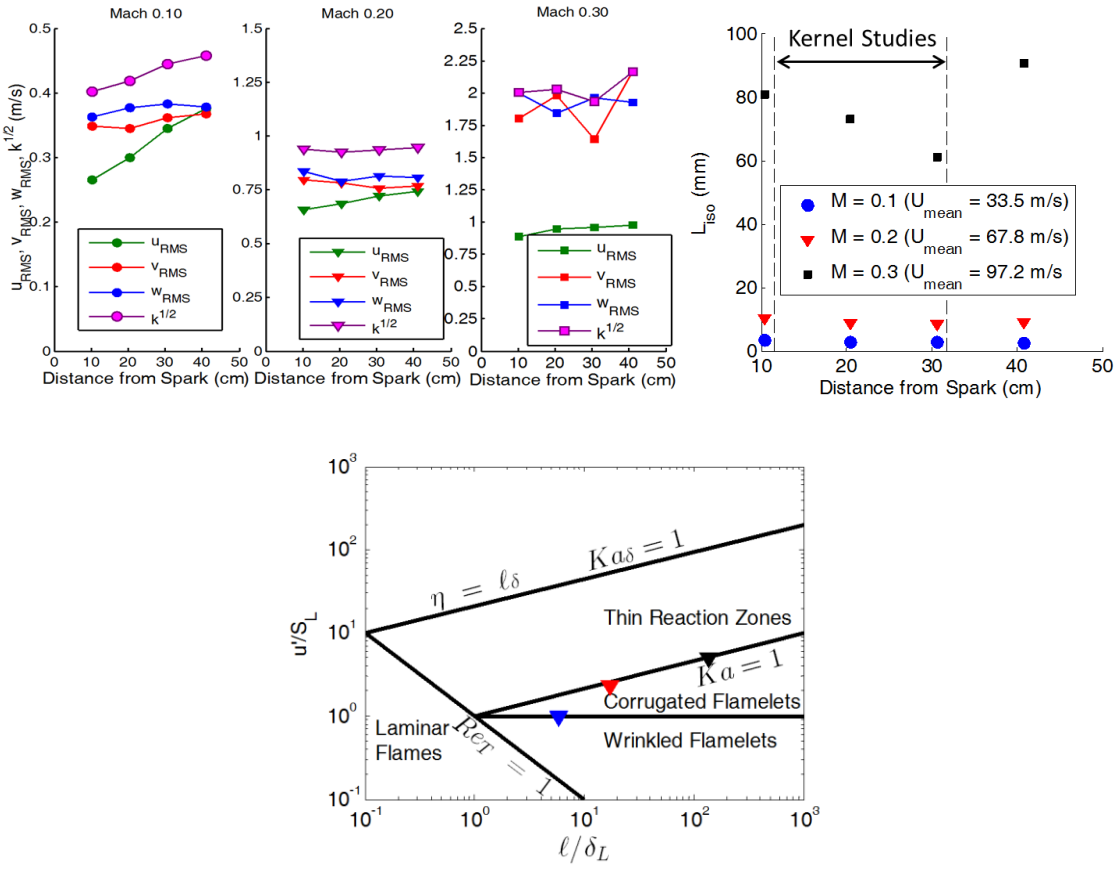


Figure 14: Turbulence levels for M = 0.1 (left), 0.2 (center left), 0.3 (center right), length scales (right) [52], and regime diagram locations (bottom) as determined via hot wire anemometry for the vane turbulence generator.

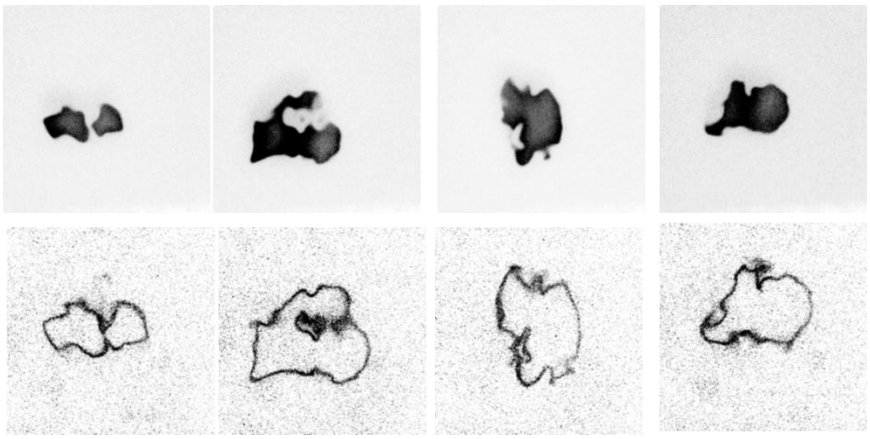

Figure 15: Raw images of OH PLIF (top) and $CH_2O$ PLIF (bottom) taken at M = 0.3 and t = 2.892 ms for the vane grid turbulence generator.

Example c-maps for M = 0.2 and 0.3 are shown in Figure 16 as determined from the OH images. The peanut like structure in the earlier stages of kernel growth is an artifact from beam quality produced by the new spark laser (this will be discussed further in the next section). From these images, kernel growth was inferred as shown in Figure 17. As shown, the growth rates are higher for both M = 0.2 and 0.3 than for M = 0.1 due to the higher levels of turbulence produced with the M = 0.3 profiles growing slightly faster than M = 0.2.

To further examine the changes in burning rates due to increased turbulence achieved at higher Mach numbers, FSD was calculated as can be seen in Figure 18 showing the FSD as a function of time for both M = 0.2 and 0.3. In both Mach numbers, the FSD decreases with time due to the decaying turbulence in the tunnel as shown in Figure 18. Comparing the maximum FSD values at t = 1.842 ms between the two Mach numbers shows a slightly higher value for M = 0.2 than for 0.3.

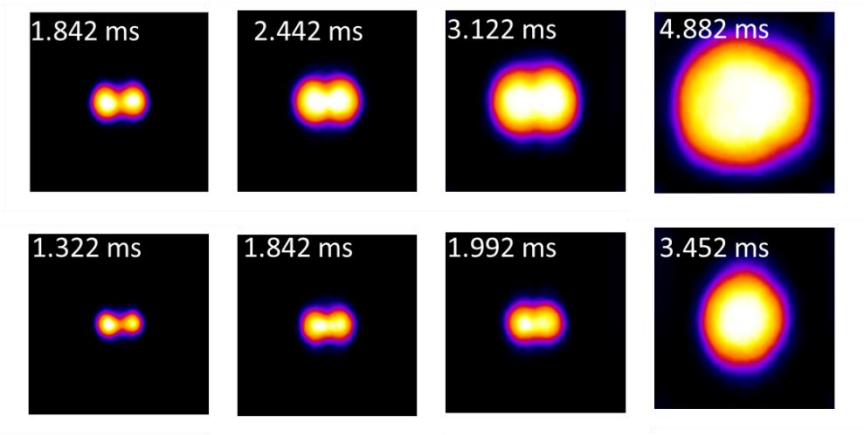


Figure 16 : C-maps for M = 0.2 (top) and M = 0.3 (bottom) at 11.5 cm (left), 15.2 cm, 19.0 cm, and 31.8 cm(right) with 10-12 mJ/ ignition for the vane grid.

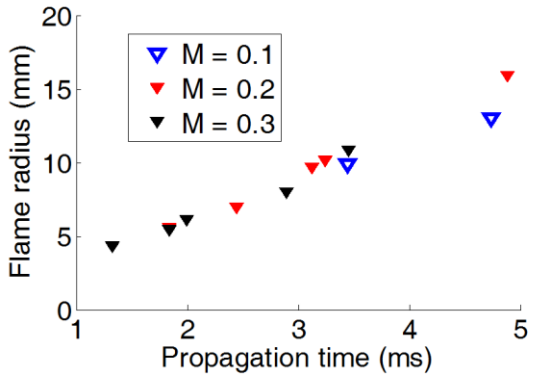


Figure 17: Radius verse time for the vane grid

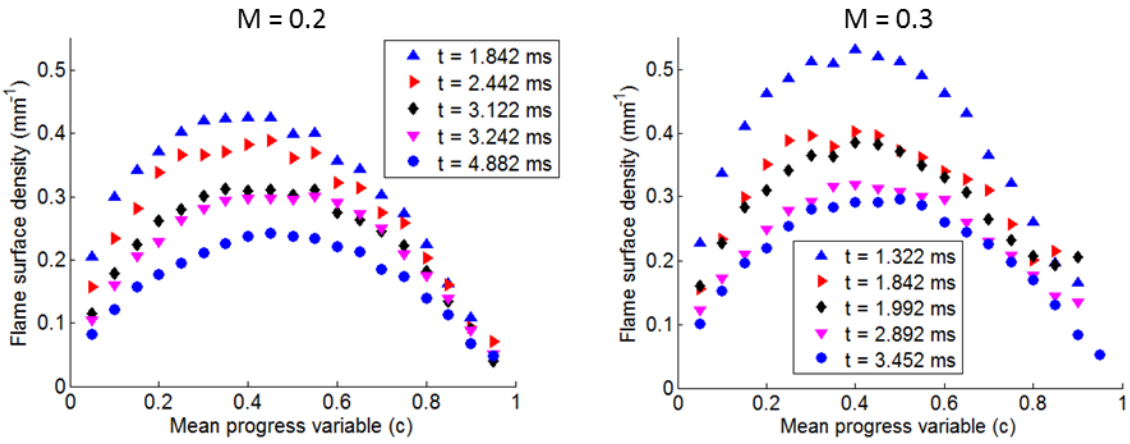


Figure 18: Flame surface density (FSD) vs time for M = 0.2 (left) and M = 0.3 (right) for the vane grid

Additionally, the measured values of FSD and $\delta_T$ show the same trends observed by Renou et al. [23] where FSD values decrease and $\delta_T$ increases w.r.t. time, although the values for both of these are higher in the current experiment as expected from the higher turbulence levels. $FSD_{max}$ and $\delta_T$ are shown Figure 19 along with their product which according to Equation 11 is proportional to $S_{T,C}$. Since the kernels are initially smaller than integral length scale of the turbulence, the local flame fronts are not affected by the full spectrum of turbulence. This results in the observed increase in $FSD_{max}*\delta_T$ (r.h.s. of Figure 19). However once the kernels are larger than the integral scale, the local consumption rates level off as seen in the M = 0.1 data and the last point in the M = 0.2 data. While the FSD and $\delta_T$ values are similar for the high turbulence cases (i.e. M = 0.2 and 0.3), they are both much higher than the low turbulence case (i.e. M = 0.1), demonstrating that even in this highly anisotropic flow field some effects of increased turbulence are still evident.

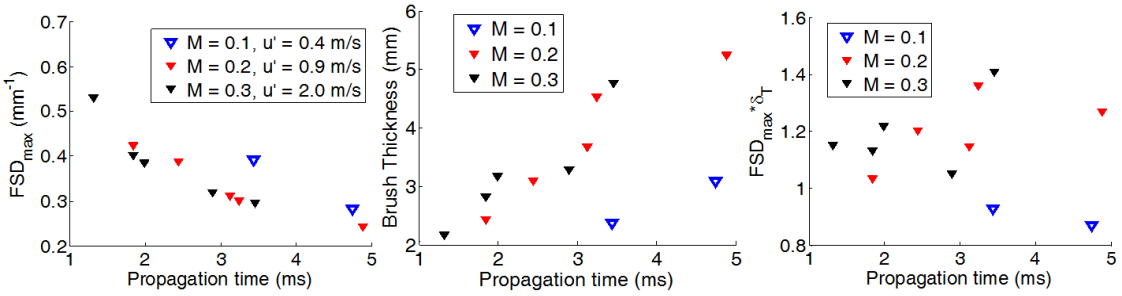


Figure 19: Maximum FSD (left), flame brush thickness (center), and the product the maximum FSD and brush thickness that is $\alpha$ $S_{T,C}$(right) for the vane grid.

Curvature statistics for the vane grid kernels are shown in Figure 20. For latter propagation times, mean curvature values are around zero similar to the lower turbulence intensity cases of the blown grid (see Appendix A). However at earlier times, there is a strong negative curvature which is unexpected for the mixture Markstein number and the small radii of

the kernels. These negative correlations are a result of the peanut shape induced from laser ignition (see Figure 16) which results in mean concave curvature at the necking region of the peanut; however, once the peanut shape goes away so do the negative curvature values.

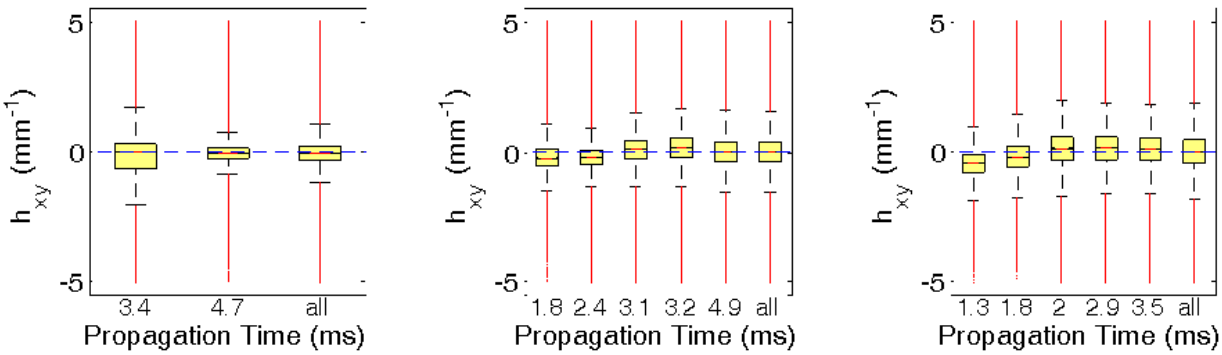


Figure 20: Standard box plot representation for instantaneous curvature statistics for vane grid kernels for M = 0.1 (left), M = 0.2 (center), and M = 0.3 (right) for the vane grid.

Finally, the flame speed data was compared with flame bomb correlations (see Figure 21) done by Chaudhuri et al. [5] who found that spherical flame growth can be correlated using a turbulent Reynolds number based off of the flame radius via $Re_{T,R} = (u'*R)/(S_L*\delta_L)$. While the flame speeds for the M = 0.1 case are close to the flame bomb correlation, the flame speeds measured for both M = 0.2 and 0.3 fall below the flame bomb correlation. This discrepancy is most likely due to the large-scale anisotropic turbulence at the high Mach number cases ($\ell$ = 10.2 mm and 80,9 mm for M = 0.2 and 0.3 respectively) where $u_{eff} << u'$, whereas for the M = 0.1 data the flow is less anisotropic with $\ell$ = 3.5 mm and $u_{eff} \approx u'$. Due to the limitations of the current hot wire system, the turbulence spectra can only be measured in the longitudinal direction and not the transverse directions. Since the flow is so highly anisotropic, the spectra in

all principal directions would be required to calculate an effective turbulence velocity to properly normalize the correlation.

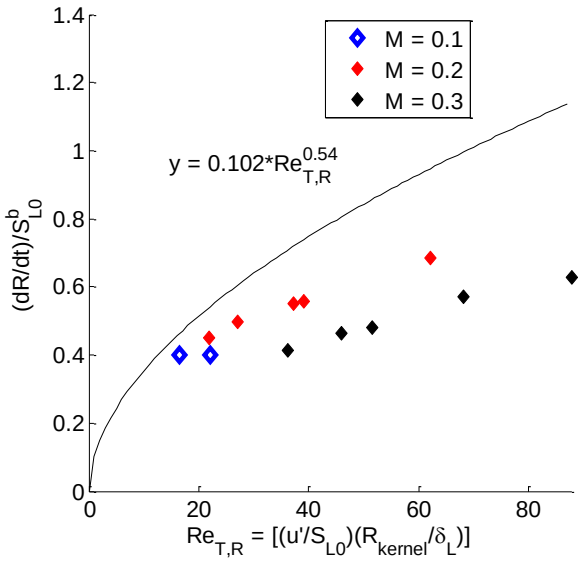


Figure 21: Flame speed correlations for the vane grid. The solid line is from Chaudhuri et al. [5] for $CH_4$-air mixture at $\phi = 0.9$.

Although the vane grid produced much smaller scales than the blown grid (see Appendix A) and resulted in an observable difference in flame properties as a function of u', the scales were still too large to wrinkle the flame front to achieve a constant local consumption rate, $S_{T,C}$, for the M = 0.3 case. In addition, since the $u'_{eff}$ values (the portion of the turbulence energy which can effectively wrinkle a kernel as shown in Figure 5) cannot be calculated with the current system. It is unknown if the discrepancy between the vane grid data and flame bomb data is caused by the large scale anisotropic flow field. Additionally, since vortex stretching in the nozzle and the resultant turbulent length scales are proportional to mean flow velocity, u' and ℓ could not be independently varied thereby preventing a systematic study of turbulent

premixed flame interaction which would have been otherwise possible in a traditional flame bomb.

Therefore, in order to conduct a proper comparison with flame bomb measurements and to demonstrate the utility of the current system in determining the fundamental turbulence-flame interaction, small-scale isotropic turbulence studies were conducted.

**Isotropic, small-scale turbulence**

To eliminate the large scale anisotropic turbulence caused by vortex stretching through the nozzle, a new post-nozzle passive grid (PNPG) system was implemented. The turbulence intensity, length scales, and regime diagram locations for PNPG kernel tests are shown in Figure 22. The turbulence produced by the passive grid is isotropic, thereby enabling a proper comparison with classical flame bomb correlations. Furthermore, the integral length scale is appreciably smaller (ℓ~3 mm) than the anisotropic turbulence (see Table 1) and constant across all Mach numbers.

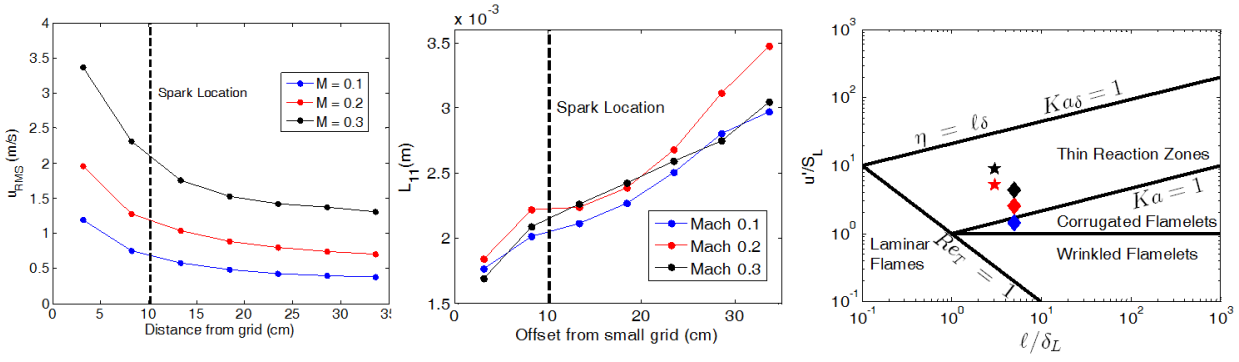


Figure 22: Turbulence values for PNPG kernel experiments (left) [62] with regime diagram (right) with ℓ = 3 mm (i.e. the mesh size of the PNPG). The spark location is indicated by the dash line.

The same lasers and cameras used in the vane grid experiments were used in the PNPG experiments with the following changes: 1) the binning of the cameras was reduced by a factor of 2 (2x2 binning for the $CH_2O$ camera and full frame for the OH camera), and 2) to achieve better beam quality the SpectraPhysics spark laser was operated at full power with only a small portion of the beam being sent to the test section as shown in Figure 23. The reduced binning provided for increased spatial resolution at the cost of repetition rate now being 5 Hz resulting in every other kernel going unrecorded by the cameras. The latter change was to improve laser beam quality and reduce the required energy for successful kernel ignition. It was found that at low power the beam quality was significantly reduced which resulted in the need for higher spark power in the vane grid experiments. By running the laser at full power, kernels could be sparked at ~4.5 mJ/pulse for low turbulence cases, but at higher turbulence this was insufficient to initiate a chemical reaction due to heat convection as described by previous authors [21], but still resulted in hot gases as indicated by the $CH_2O$ signal shown in Figure 24 (n.b. there was no OH signal for any of these kernels indicating that the reaction never initiated). Further testing demonstrated that ~7 mJ/pulse was required for reliable kernel ignition for the high turbulence cases. To reduce systemic variations between experiments, 7 mJ/pulse was used for all cases. The OH/$CH_2O$ images shown in Figure 25 demonstrate that even for the highest turbulence case ($M = 0.3$, $\phi = 0.7$), local extinction is a rare event.

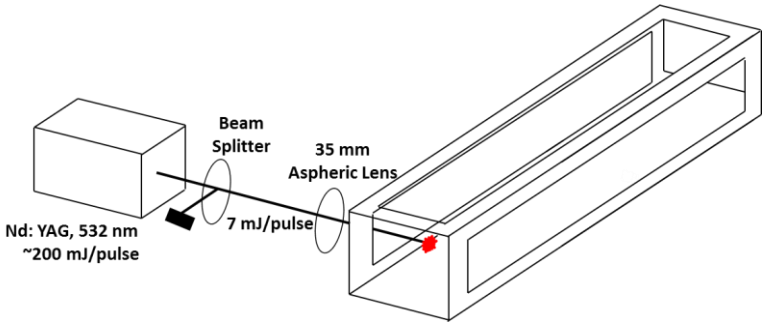


Figure 23: Schematic of revised spark laser system for PNPG experiments.

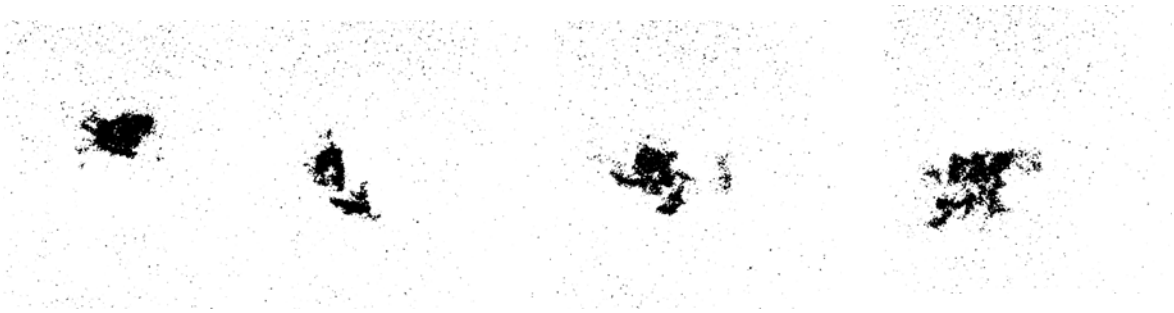

Figure 24: Sample raw $CH_2O$ created by plasma kernels which failed to initiate a flame kernel at M = 0.3/$\phi$ = 1 for the PNPG turbulence.

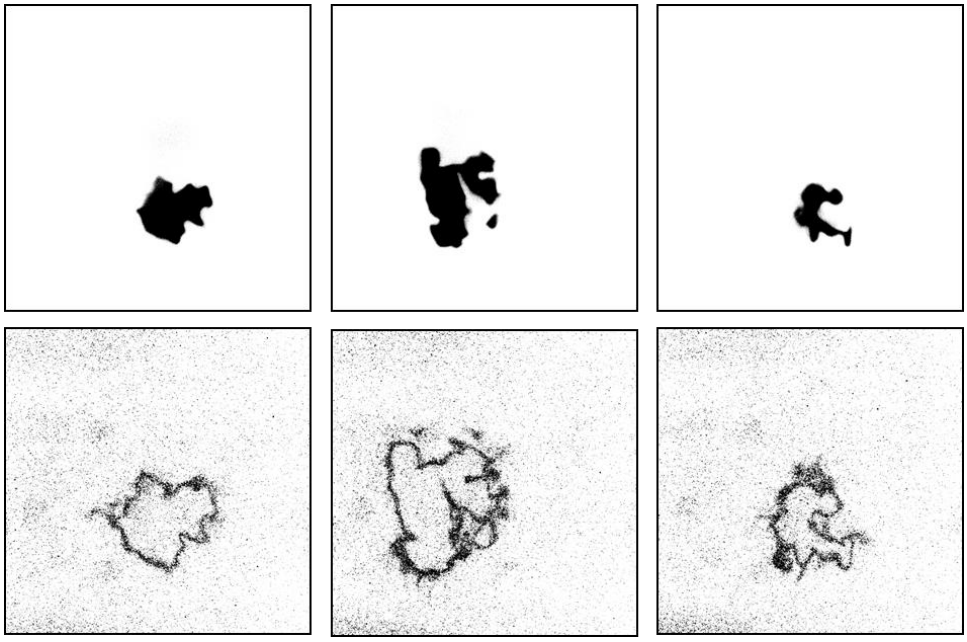

Figure 25: Sample raw OH (top) and $CH_2O$ PLIF (bottom) images before corrections or dewarping for M = 0.3/ $\phi$ = 0.7 for the PNPG turbulence generator.

As noted in Figure 22, the spark location is ~10 cm downstream of the grid which resulted in optical access at time delays closer to ignition. Furthermore to increase temporal resolution and range of kernel propagation, the probe locations were spaced 2.54 cm apart over a total range of ~30.5 cm (~1 ms to ~4.5 ms propagation time). The c-maps for all conditions are shown in Figures 26 and 27 with respect to both space and time both measured relative to the spark ignition point.

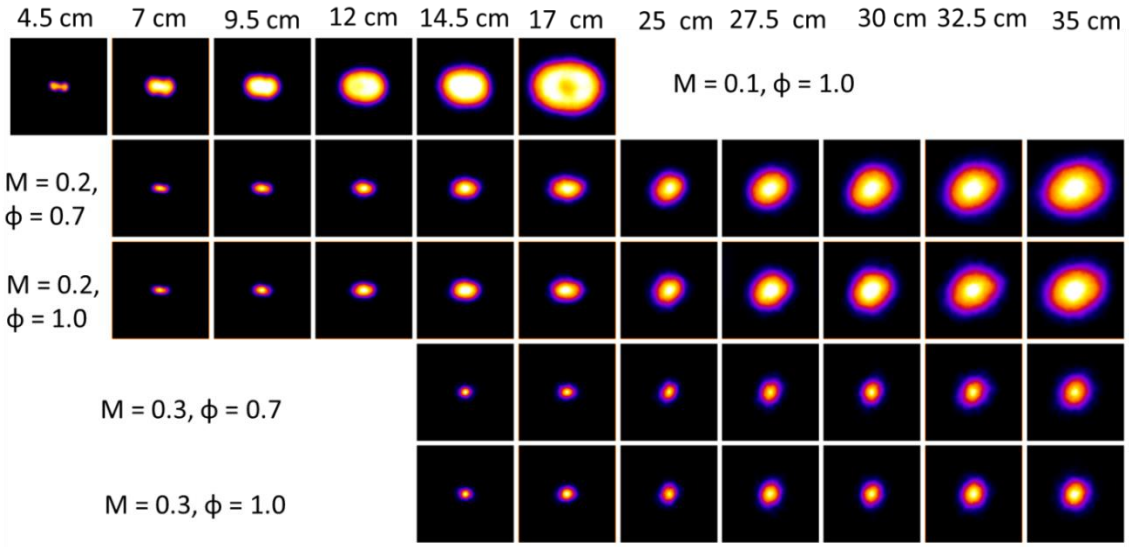


Figure 26: Evolution of centered kernel c-maps for the PNPG. The columns are the nominal positions of the kernels (i.e. position of the camera) with distances given relative to spark location.

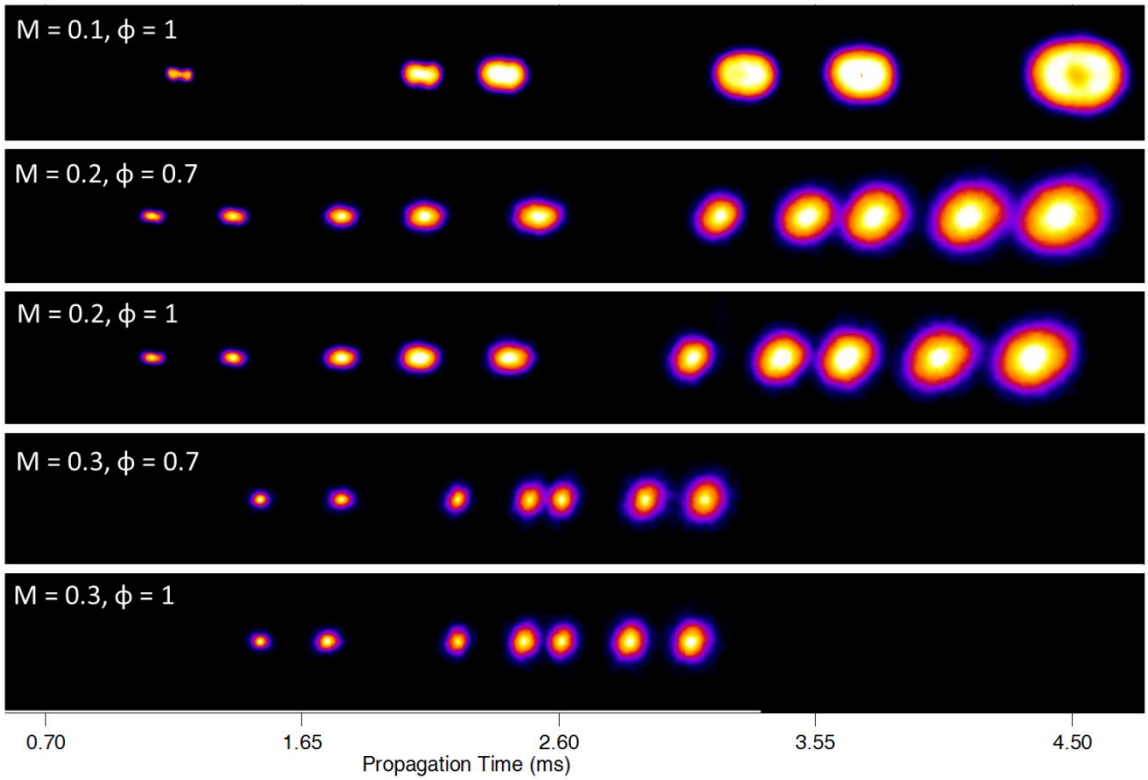


Figure 27: Temporal evolutions of kernel c-maps for the PNPG studies. Times are relative to the spark.

Flame brush and $FSD_{max}$ determined from these c-maps are shown in Figure 28. Unlike the large-scale anisotropic turbulence, there is a clear increase with $S_{T,C}$ as a function of u' as expected from classical correlations shown in Figure 4. Additionally, $S_{T,C}$ is roughly constant for the small-scale turbulence since the initial radii of the kernels is comparable to ℓ, and thus all of the turbulence scales are able to perturb the local flame front and consumption rates. This result would suggest that $R_{kernel} > \ell$ is a sufficient condition for all of the turbulence energy to affect local flame kernel propagation. It should be noted that $S_{T,C}$ being shown in Figure 28 is a local consumption rate, and the global consumption rate would scale with $R^2$.

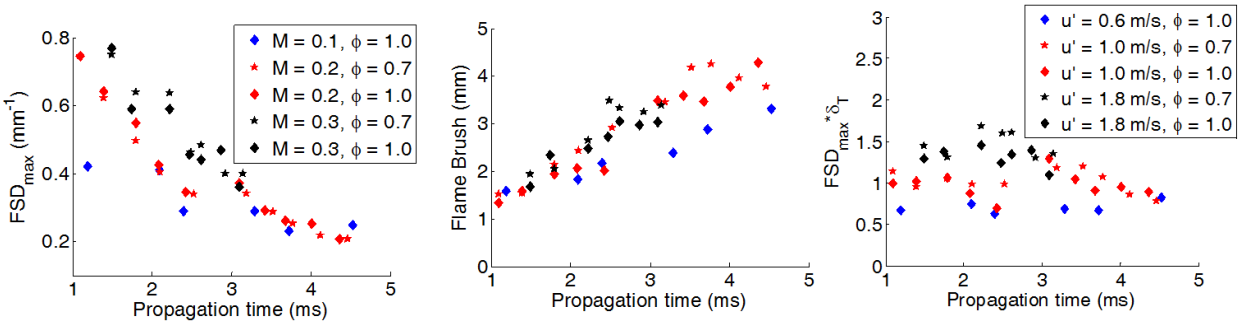


Figure 28: Maximum FSD (left), flame brush thickness (center), and the product the maximum FSD and brush thickness that is $\alpha S_{T,C}$ (right) for the PNPG. The Mach number for each case is given in the left legend and the u' values are given in the right legend.

Curvature statistics for the PNPG kernels are provided in Figure 29. Similar to the vane grid data, the M= 0.1 curvature data has a slightly negative curvature preference due to the peanut structure, while most other data sets have a positive mean curvature due to the small kernel size. The stoichiometric kernels (Ma > 1) are more likely to be positively curved than negative, and the lean cases show no overall curvature preference even at high turbulence levels since for this mixture Ma = 0.36 and would be less sensitive to curvature and stretch.

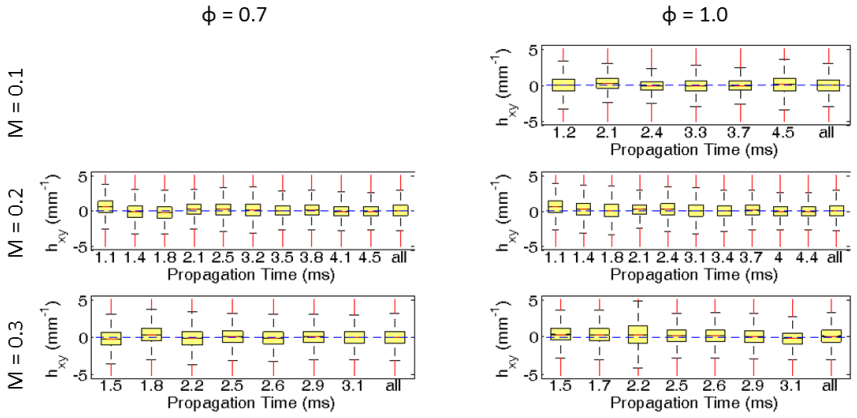


Figure 29: Standard box plot representation for instantaneous curvature statistics for the PNPG kernels.

The radius and growth rates of the kernels are shown in Figure 30. As can be seen in the Figure 30, dR/dt is a function of both R and t. Therefore, an appropriate flame kernel correlation should incorporate both u' and R (i.e. Figure 4 right).

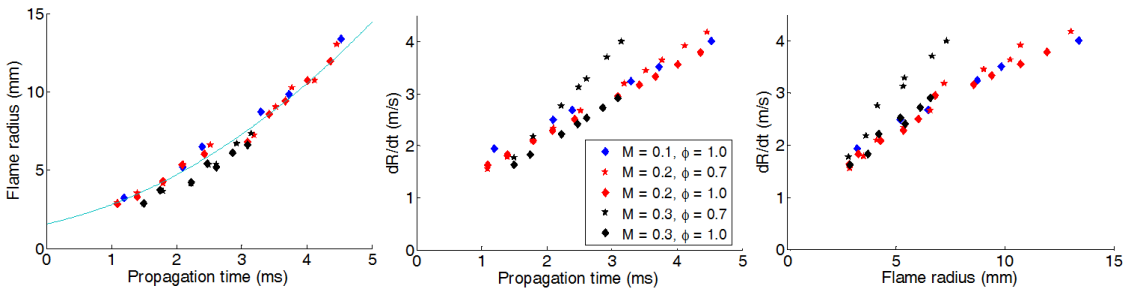


Figure 30: Flame radius (left, with trend line through M = 0.2, $\phi$ = 1 data) and growth rates for the PNPG kernels.

Finally, the measured flame speeds are compared to flame bomb correlations to determine if there are any effects of compressibility on flame kernel propagation. The correlations, shown in Figure 31 are compared to flame bomb correlations done by Chaudhuri et al. [5-7, 63]. In addition to the dependence on $Re_{T,R}$, they found that propagation speeds are inversely proportional with Markstein number (i.e. the $\phi$ = 0.7 kernels should propagate faster than the $\phi$ = 1 kernels). In general, the current data have the same Ma dependence with faster propagation rates observed for the $\phi$ = 0.7 data than the stoichiometric data. Additionally, both data sets have the same $(Re_{T,R})^{0.5}$ dependence as found in the flame bomb data demonstrating the same underlying physics in high speed turbulent flows and turbulent flows with no mean velocity.

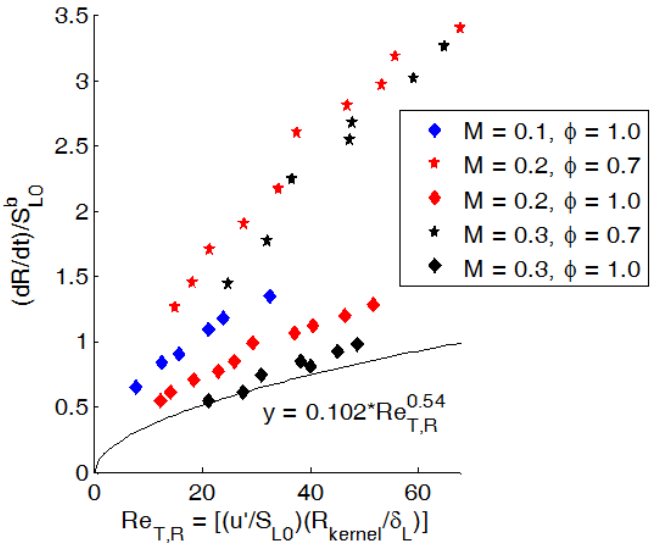


Figure 31: Flame speed correlations for the PNPG data for $CH_4$-air mixtures. The solid line is from Chaudhuri et al. [5] for $CH_4$-air mixture at $\phi = 0.9$.

However, the current flame speeds exceed their correlated values at similar Ma (i.e. comparing the current $\phi = 1$ data to Chaudhuri et al.'s [5] $\phi = 0.9$ data), which is unexpected since $\phi = 0.9$ has a lower Ma and should have higher propagation rates. One possible reason for this discrepancy could be due to differences in the flow field. The flame bomb experiments have a mean radial inflow (which would impede flame propagation) that becomes more significant at larger radii and turbulence levels as shown in their error bars (c.f. Figure 2 [5]), whereas the current configuration has no such radial component (the uncertainty in the current measurements, if available, would be w.r.t. u' and thus result in horizontal error bars). However, this doesn't explain the why there are significant differences for the stoichiometric data as a function of M while the lean $\phi = 0.7$ data collapses.

Alternatively, $Re_{T,R}$ can be normalized using the Markstein length, $\delta_M$, instead of the laminar flame thickness, $\delta_L$, as can be seen in Figure 32 or plotted against $(Re_{T,R})^{0.5}$ as shown in Figure 33. Once again, the lean data show a reasonable correlation across the two mean flows

tested. However, the stoichiometric data now correlate with the lean data for a given M. Therefore, it's possible that the stoichiometric kernels would collapse similar to the lean kernels at larger $Re_{T,R}$ values (i.e. at larger radii or $Re_{T,R}$ than is possible with the current wind tunnel configuration). Additionally, the offsets at small radii (i.e. low values of $Re_{T,R}$) could be due to laser ignition artifacts. As can be seen in Figures 26 and 27, due to increased convection of the laser-induced plasma, the shape of the early kernels changes as the Mach number (and therefore turbulence intensity) increases. Namely, the shape of the original kernel changes from a peanut at M = 0.1, to an ellipse at M = 0.2, and finally to a sphere at M = 0.3. It was further shown via the curvature data in Figure 29 (and Figure 20 for the vane grid data) that the peanut shape present for the M = 0.1 case resulted in a negative mean curvature. Since for high Ma numbers (like the stoichiometric case), this would increase the average flame speed until the peanut shape closed, while the M = 0.2 and M = 0.3 cases would have no such enhancement.

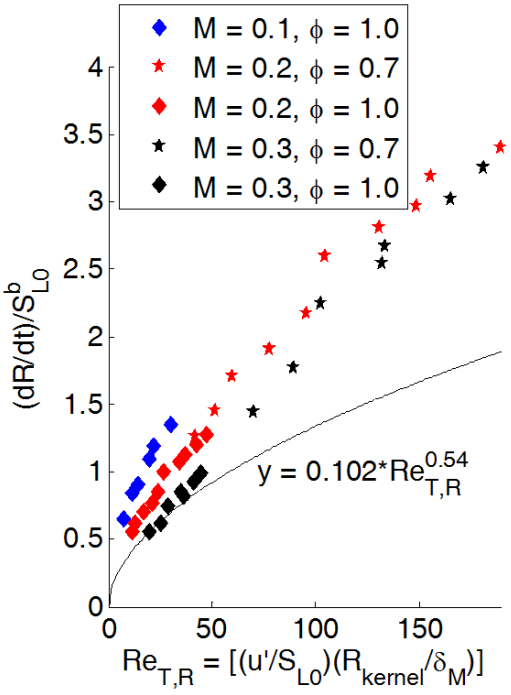


Figure32: Flame speed correlations for the PNPG data using Halter et al.'s [41] data for $\delta_M$. The solid line is from Chaudhuri et al. [5] for $CH_4$ -air mixture at $\phi$ = 0.9.

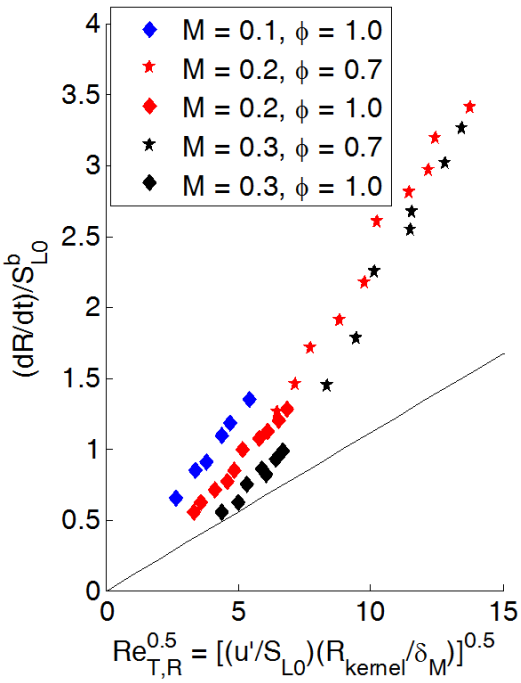


Figure 33: Flame speed correlations vs $(Re_{T,R})^{0.5}$ for the PNPG using Halter et al.'s [41] data for $\delta_M$. The solid line is from Chaudhuri et al. [5] for $CH_4$ -air mixture at $\phi$ = 0.9.

Comparison with the flame bomb data of Chaudhuri et al. [5] (i.e. the black lines in Figures 32 and 33 scaled to account for differences between $\delta_M$ and $\delta_L$) indicate that the turbulent flame speeds measured in the current experiment are higher than the flame bomb data at similar values of $Re_{T,R}$. However, turbulent flame speeds measured over a wide range of mixtures and turbulence intensities had reasonable correlation for flame bomb data if $\delta_M$ was used to calculate $Re_{T,R}$ (c.f. Figure 10 Chaudhuri et al. [6]). Therefore, the faster propagation rates observed in the current experiment are most likely due to inherent differences in the mean flow field (i.e. plug flow versus mean radial inflow).

It can be seen in Figures 31 - 33 that the choice laminar length scale in $Re_{T,R}$ (i.e. $\delta_L$ or $\delta_M$) can affect the correlation especially with respect to equivalence ratio. Therefore, different values of extrapolating measured flame speeds (i.e. linear or nonlinear) to calculate $\delta_M$ will affect the correlation shown in Figures 32 and 33. For comparison, values for $\delta_M$ calculated using a linear extrapolation are shown in Figure 34 using the values of Aung et al. [42].

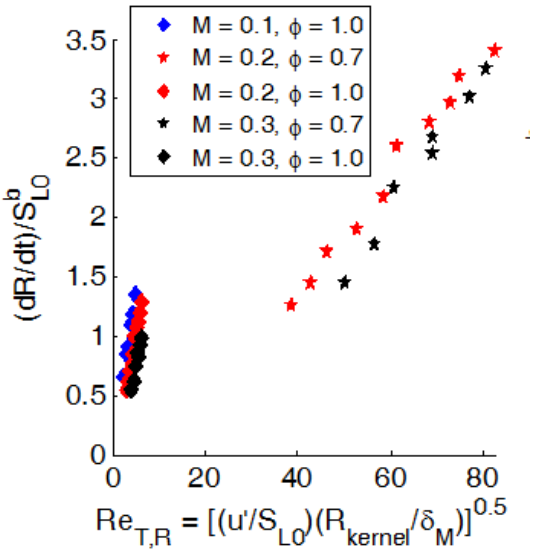


Figure 34: Flame speed correlations vs $(Re_{T,R})^{0.5}$ for the PNPG using Aung et al.'s [42] data $\delta_M$.

As evident in Figure 34, normalizing $Re_{T,R}$ by Aung et al's [42] linearly extrapolated values for $\delta_M$ (0.0099 mm and 0.78 mm for φ = 0.7 and 1 respectively) caused the flame speeds between the two equivalence ratios decorrelate. This observation further corroborates the measurements of Halter et al. [41] and the extensive comparisons conducted by Kelley [17].

**Comparison with slow speed, large duct kernel data and $u'_{eff}$ considerations**

After the previous experiments were conducted, follow-up work by Georgia Tech was conducted using the vane grid turbulence generator but with a modified tunnel configuration where the nozzle was removed altogether resulting in a 152 mm x 152 mm test section. The kernel radius taken from these experiments [62] are shown in Figure 35 taken at a similar turbulence intensity equivalence ratio to the lean cases shown before (and hence a similar but slightly greater Markstein number), but used a 15 mJ/pulse spark instead of a 7 mJ/pulse spark. Shown in the figure is a polynomial fit similar to the one used in the PNPG data, but due to the sparsity of data the fit shows an unphysical rise at t < 2 ms which results in an artificially high flame speed. To remove this artifact, an estimate of the t = 0 ms radius for the large duct data by extrapolating the PNPG data to t = 0 ms (i.e. ~1.5 mm, see Figure 30 left) and scaling by different spark energies used (i.e. $R_{0,big\ duct}$ = 1.5 mm*(15 mJ/7 mJ)$^{1/3}$ = 1.9 mm). For comparison, the calculated $S_{T,D}$ values from both of these fits will be shown.

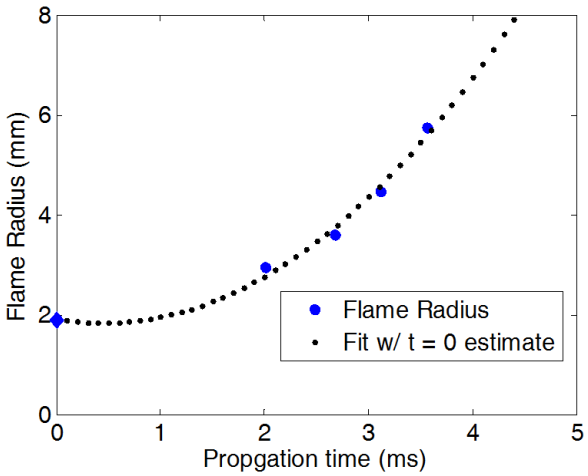


Figure 35: Flame radius data from slow-speed large duct tunnel at $\phi$ = 0.71 and u'=2.8 m/s [62]. The blue diamond at t = 0 ms is estimated from the PNPG data.

Since the large duct turbulence ℓ = 27 mm which is appreciably larger than the kernels especially at earlier times, an effective u' must be used to properly correlate the data. Since the turbulent flow field inside the large duct is isotropic, the effective u', $u_{eff}$, value can be calculated using 1D spectra. Currently, the scaling proposed by Bradley et al. [10] is used:

$$\frac{u'_{eff}}{u'} = \left[\frac{15^{0.5}}{Re_\lambda}\int_{k_G}^{k_R}\bar{S}(\bar{k}_\eta)d\bar{k}_\eta\right]^{1/2} \qquad 22$$

The data from the large duct is plotted against the PNPG data using the $u'_{eff}$ shown in Figure 36, and there is excellent agreement between the PNPG data and the large duct tunnel.

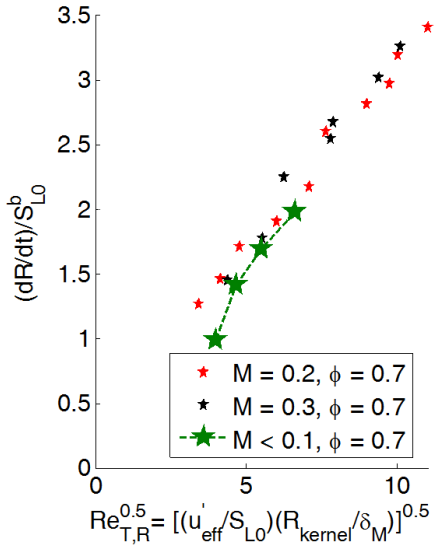


Figure 36: Comparison of flame speed correlation for the high speed PNPG data (M = 0.2 and 0.3, ϕ = 0.7) and low speed vane grid data (M < 0.1, ϕ = 0.71).

The correlation seen in Figure 36 helps to access the following two effects on kernel propagation: 1) confinement and/or flame-wall interactions which would be more significant in the smaller duct, and 2) the effects of mean velocity. While confinement effects were not

accounted for in either experiment, these effects are only significant if $R_{kernel}/R_{vessel} > 0.4$ [3] or $R_{kernel} > 10$ mm for the PNPG data. Since most of the kernels were smaller than this threshold, confinement effects should not have a significant effect on the observed correlation. As for mean flow effects, the PNPG data for M = 0.2 and 0.3 for $\phi = 0.7$ correlated well with the M < 0.1 data found in the big duct at similar equivalence ratios. Therefore the data shown in Figure 36 demonstrates that mean flow velocity doesn't affect flame propagation at least in the limit M < 0.3. Therefore, it's suggested that differences between the current $\phi = 1$ data and Chaudhuri et al.'s data at $\phi = 0.9$ [5] is most likely due to differences in radial flow components and laser ignition artifacts.

**Experimental advantages of current system and future work**

Having demonstrated the ability to correlate incompressible flame kernels over a wide range of mean flow speeds, the current wind tunnel configuration can now be used to access flame kernel propagation over a much wider parameter space (e.g., fuel, $\phi$, u', etc.). Unlike the current system which can acquire flame kernel statistics at 10 Hz, the frequency of flame bomb testing can be very low due to the need to fill the bomb with a homogenous combustible mixture (~5 minutes for flame bomb data comparison [17]) and evacuate the post-combustion mixture (pumped down and filled with air twice before mixtures insertion [17]). Therefore, the current system can make ensemble averages much faster than traditional systems.

Additionally, compressible and supersonic flows can also be studied. Supersonic flows permit the study of shock-kernel interactions which have previously only been possible in shock tubes at very low repetition rates [18, 19, 64] and were limited in time duration due to the eventual

interaction of reflected shocks. The current system could study an arbitrary number of normal or oblique shock-kernel interactions with no such restrictions.

## Conclusions

A new means of studying phenomenological premixed flame kernel propagation was studied using freely propagating flame kernels over a range of turbulence levels and conditions and compared to traditional flame bomb measurements. It was found that for large-scale anisotropic turbulence, the flame kernel growth was less than flame bomb correlations even if laser ignition effects were accounted for. This decrease in correlated flame speed is caused by only a fraction of the turbulence energy being able to fit inside the kernels and wrinkle the flame front thus effecting flame speed. It was found that the nozzle used to accelerate the flow to high mean velocities created this undesirable flow field. In addition, since the degree of vortex stretching is proportional the acceleration through the nozzle, the turbulent intensities and length scales could not be independently varied precluding a systemic study of turbulent-flame interactions. Therefore, additional experiments were conducted by either removing the nozzle entirely or by generating turbulence after the contraction thereby removing the Mach number dependent anisotropy and larger scales caused by vortex stretching through the nozzle.

For small-scale isotropic turbulence generated by a post-nozzle passive, the data agreed reasonably well showing the same dependence on $Re_{T,R}$. Additionally, Markstein effects on flame kernel propagation were observed and flame speeds were inversely proportional to Ma as expected, and normalizing the data with the Markstein length collapsed the data for a given Mach number/turbulence intensity. However, the stoichiometric data seemed to have a dependence on mean flow and/or turbulence intensity, and their propagation rates slightly

exceeded the $\phi = 0.9$ flame bomb correlation. The discrepancies between the stoichiometric data were most likely caused by laser ignition artifacts, such as the peanut shape seen in the M = 0.1 data. This peanut shape resulted in a negative mean curvature, and for the high Markstein number of the mixture this would result in an enhanced flame speed relative to the M = 0.2 and 0.3 cases thus causing the apparent Mach number dependence. The differences between the current data and the flame bomb data were likely due to: 1) laser ignition artifacts, and 2) the lack of a radial mean flow that is caused by the fan stirred turbulence used in the flame bomb.

Since the $\phi = 0.7$ data had a low Markstein number, the initial shape of the kernel and the resultant curvature did not affect flame speeds and the data for these cases correlated well across all mean flow speeds tested. Therefore, an additional comparison with low speed ($M < 0.1$, $\phi = 0.71$) kernel propagation data was also conducted. When an effective turbulence was used (i.e. the turbulence at scales which can effectively wrinkle the kernel) to account for the larger integral length scales of the low speed experiment, the data between the high and low speed data correlated well with each other indicating that the discrepancies found for the $\phi = 1$ case were likely due to laser ignition artifacts. Therefore, it has been demonstrated that the current apparatus can be used to study premixed turbulent flame kernels without the radial mean flow or low repetition rates of flame bombs.

The primary findings of this study are: 1) for incompressible flows the measured flame speeds had similar trends and dependencies to flame bomb data and differences between the two sets are most likely due to the lack of radial inflow in the present experiment and laser ignition artifacts, and 2) when the current high speed ($M > 0.2$) flame kernel propagation data was compared to low speed ($M < 0.1$) data in the same facility the data correlated very well for

lean cases. These two findings indicate that the current device is capable of studying phenomenological premixed turbulent flame interactions as an alternative to flame bomb measurements which might suffer from a radial mean inflow. Additionally, future experiments can be conducted at both higher turbulence levels and supersonic flows which may not have been possible with traditional flame bomb devices.

# CHAPTER 3: UV RAMAN MEASUREMENTS IN A SCRAMJET COMBUSTOR

## Background

As previously mentioned, numerical models are needed to develop scramjet engines. In order to verify the ability of these numerical models to predict turbulence-chemistry interaction, *in situ* and temporally resolved experimental measurements of temperature and species are needed in compressible flows with realistic combustors. O'Byrne et al. [65] have performed extensive coherent anti-Stokes Raman scattering (CARS) measurements in a model scramjet combustor. They recorded temperature and mole fractions of $O_2$, $N_2$, and $H_2$ (employing vibrational CARS for $O_2$ and $N_2$ but rotational CARS for $H_2$) in a hydrogen-fueled scramjet duct; the approach used was a variant of the dual-pump CARS technique [66, 67]. Of course, in a hydrocarbon fueled combustor, measurement of all major species is a challenge for CARS, although new developments have demonstrated improved capabilities of multi-species detection using variants of the dual pump technique [68] or with femtosecond lasers using chirped pulses or beam shaping [69]. Spontaneous Raman scattering can satisfy this requirement (to measure all major species) using only a single laser, a distinct advantage over CARS. A detailed description of Raman scattering is given by Barlow et al. [70], but a brief explanation will be given here.

In both Rayleigh and Raman scattering, incident photons excite a molecule to a virtual state, and then a photon is emitted when the molecule returns to the ground state. In Rayleigh scattering, this is an elastic scattering process where the incident and emitted photon are the same wavelength, $\lambda$. In Raman scattering, the molecule doesn't return to the initial ro-vibrational state and hence the emitted photon has shifted. For vibrational Raman scattering (the method used for the current study), this shift is equal to the vibrational frequency of the

molecule. Therefore, Raman scattered light from one type of molecule will have a different wavelength than light scattered from any other molecule (e.g. $O_2$ and $N_2$ will produce scattered light at different wavelengths). Additionally, the amount of scattered light, $S_i$, from a species is proportional to the number density of that species, $N_i$, a temperature dependent factor, f(T), and its cross section, $\sigma_i$, as shown in Equation 23 where $I_L$ is the laser energy. Since $\sigma_i$ is inversely proportional to the $\lambda_0^4$, the use of a UV laser increases the signal strength and was chosen for this study. The system was calibrated at known temperatures and species concentrations (represented by C (T) in Equation 24 and shown in Figure 43), allowing for quantitative species measurements to be. Furthermore, at known pressures the ideal gas law can be used to determine the temperature using Boltzmann':

$$S_i \propto N_i I_L \sigma_i f(T) \quad (23)$$

$$N_i = \frac{S_i C(T)}{I_L} \quad (24)$$

$$T = \frac{P}{k \sum N_i} \quad (25)$$

Previously, Raman scattering has been used in enclosed subsonic combustors most recently by Meier and colleagues [71-73], open supersonic jets by Cheng et al. [74], and in supersonic combustors without reaction by Carter and colleagues [75, 76]. However, to the authors' knowledge, there has not been Raman scattering measurements inside an enclosed, supersonic, reacting combustor. In this application UV vibrational Raman scattering, based on a KrF excimer laser, with 248-nm excitation is employed instead of visible Raman scattering because: 1) scattering cross sections in the UV are significantly larger than scattering in the

visible, therefore single-shot scattering signals are relatively large (for the same laser pulse energy); 2) due to the ~20 ns KrF laser pulse no pulse stretching is needed to avoid dielectric breakdown. Since the Raman measurements provide all major species and temperature, these scalar values can be plotted against mixture fraction to deduce chemistry-turbulence interaction in the combustion chamber. Mixture fraction is a conserved scalar which is not affected by either the rate of the reaction or its progress and is only indicative of the mixing between the fuel and air streams. The mixture fraction is denoted as 0 in the air stream and 1 in the fuel stream. Mixture fraction, ξ, can be defined as:

$$\xi = \frac{Y_C + \frac{v_H}{v_C} Y_H}{Y_{C,1} + \frac{v_H}{v_C} Y_{H,1}} \qquad 26$$

where $v_j$ are the stoichiometric elemental coefficients (for the fuel the 30% $H_2$/70% $CH_4$ mixture used in this study: $v_C = 7$, $v_H = 34$), $Y_j$ are elemental mass fractions, and the subscript 1 represents the fuel stream. The stoichiometric mixture fraction for this fuel is 0.0525.

In order to assure the relevance of the measurements, UV Raman measurements were taken in a wall cavity flame holder. Wall cavity flame holders are perhaps the simplest means of providing 1) adequate residence time, 2) reliable flame holding across a wide range of flight conditions, and 3) minimal increases in drag [77]. Furthermore, wall cavities can be designed to include unobstructed optical access and offer a canonical flow which can easily be modeled [78]. Since good agreement was obtained between experimental and numerical results in an unreacting flow over a ramp close-out wall cavity before [78], this configuration was used in the current study to help verify numerical predictions of reacting conditions. Previous experiments by Gruber et al. [79] and Rasmussen et al. [80] have shown that direct fueling from the rear of the cavity supports combustion over wider range of conditions and a more uniform fuel-air

mixture with longer residence times than fueling from either passive entrainment or the floor of a cavity, so this fueling strategy was implemented in this study.

**Scramjet test facility and UV Raman system**

The experiments were conducted at the supersonic flow facility in Research Cell 19 at the Aerospace Systems Directorate, Wright-Patterson Air Force Base. The wind-tunnel employed a 2-D Mach-2 nozzle with an air flow rate of 3.1 kg/s. A schematic of the wind-tunnel and test section can be found in Figure 37 and 38. The coordinates given in this paper are in reference to x = 0 being on the step in the axial direction, z = 0 being on the step in the vertical direction, and y = 0 being centered on the spanwise centerline. An isolator of constant cross section (51 mm high by 153 mm wide) was upstream of the test section. There was a 2.5° expansion of the test section floor. Flame holding was provided by a cavity, which was 16.5 mm deep for 46 mm before ascending back to the test section floor at a 22.5° angle. Fused-silica windows (Esco S1-UV) were used to allow optical access to the test section. Windows were located on the sidewalls and the top tunnel surface.

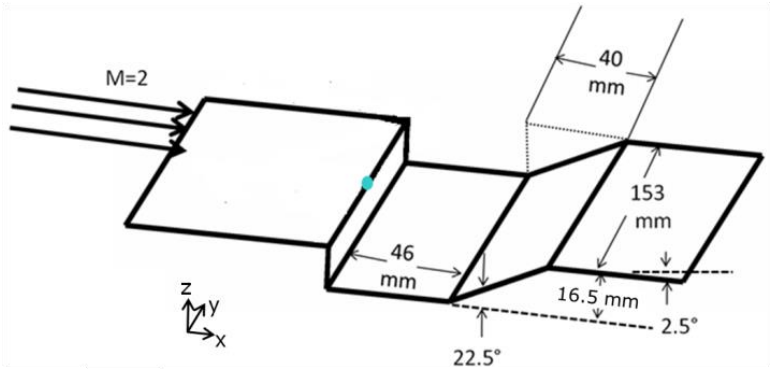


Figure 37: Mach 2 air flow over a ramp-closeout cavity. The blue dot located on the leading edge of the cavity and the centerline of the combustor (x = 0, y = 0, z = 0).

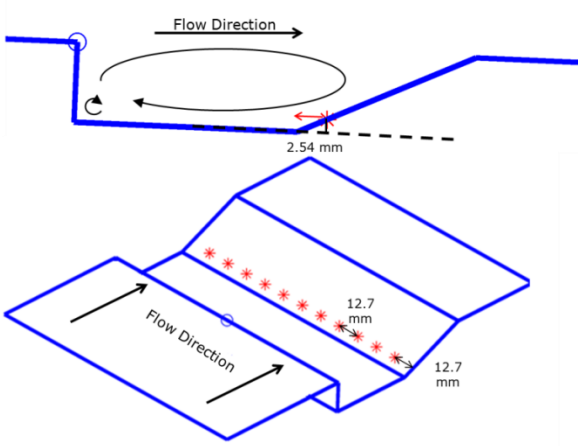


Figure 38: Close up of the fuel (red stars) injectors from the side (top) and from above at an angle (bottom). The 11 fuel injectors are spaced 12.7 mm apart with an exit diameter of 1.98 mm supplying a 70% $CH_4$/30% $H_2$ fuel blend. The recirculation zones and flow patterns are indicated in the top figure.

The tunnel supplied heated (via a natural-gas-fueled heat exchanger), compressed air (T0 = 590 K, P0 = 415 kPa) that was expanded to Mach-2 conditions at the isolator (T = 330 K, P = 53 kPa) and was further expanded due to the 2.5° expansion of the combustor at the test section (T = 300 K, P = 39 kPa). It should be noted that these wind-tunnel conditions relate, roughly, to a Mach-4 scramjet flight condition; however, the resulting static temperature in the cavity region, ~300 K, is much lower than at true flight conditions. Facility limitations (seals, etc.) prevented use of higher, more realistic temperatures. The fuel used for this study was composed of 70% methane ($CH_4$) and 30% hydrogen ($H_2$), by volume, and was premixed by the manufacturer; it was intended to represent the reactivity of a military grade hydrocarbon jet fuel but also to minimize fluorescence interference (a primary concern with the Raman scattering technique). I note too that $CH_4$ and $H_2$ are two components expected in a cracked jet fuel; other expected gaseous components include ethane ($C_2H_6$) and ethylene ($C_2H_4$). The fuel was injected parallel to the cavity floor from the cavity close-out ramp, from the locations shown in Figure 38, at a rate of 102 standard liters per minute (referenced to 273 K and 1

standard atmosphere), which is equivalent to a mass flow rate of 0.90 g/s. The fuel was passed through a manifold and split between the 11 fuel injectors, as shown in Figure 38. The exit velocity of the fuel can be estimated using continuity, and assuming that the density of the fuel at the jet exit can be approximated using the cavity static pressure and the room temperature:

$$V_{exit} = \frac{\dot{m}/11}{\rho_{exit} * A_{exit}} \approx \frac{\dot{m}/11}{\left(\frac{P_{cavity}}{R_{mix} * T_{room}}\right) A_{exit}} \qquad 27$$

Where the room temperature 293 K, injector exit area of 3.08 $mm^2$, $R_{mix}$ is 702.7 J/kg*K, and the cavity static pressure was ~37 kPa resulting in a velocity of ~150 m/s ($M_{fuel} < 0.3$)..

A narrowband Lambda Physik Compex 150 KrF excimer laser (350 mJ/pulse, 20 ns pulse length) produced 248 nm radiation that was used to excite the vibrational Raman transitions. The laser was tuned away from $O_2$ and OH laser-induced fluorescence (LIF) transitions to reduce interference with the Raman lines. To prevent damage to the fused-silica wind-tunnel windows, following the procedure used by Wehr et al. [81], two 200-mm focal length, cylindrical lenses, oriented 90° from each other, were used to focus the 248 nm beam. Additionally, a thin-film polarizer was placed before the lenses to reject any unpolarized laser radiation. The laser-beam energy measured after the lenses was ~200 mJ/pulse. Using burn patterns, the probe size was estimated to be 0.75 mm in the x direction and 1.5 mm in the z direction (see Fig. 1 for the coordinate system). Raman scattering was collected through the top wind-tunnel window, collimated, and then focused onto the entrance slit of a Horiba iHR320 spectrometer using two 5-cm-diameter ƒ/4 UV achromats, as shown in Figure 39. A 6-mm-long region of the beam was imaged, but only a 5.25-mm-long segment was used for data processing. A n-butyl acetate liquid

filter was placed before the entrance slit to block scattering at 248 nm. Raman signals were recorded with a PIMAX Superblue ICCD camera at a 10 Hz frequency, matching the pulse repetition rate of the excimer laser. The photocathode was gated at 200 ns, and to further reduce background noise, multichannel plate gating was also used. The optics directing the 248-nm beam to the test section were arranged such that the probe region could be translated vertically and axially via a remote controlled breadboard translation table.

Bottom-wall pressures along the combustor centerline are shown in Figure 40 the pressures measured upstream of the cavity are near the predicted isentropic value of 39 kPa. The drop in pressure at the fourth data point, x = 120.4 mm, which was observed in all experimental runs, is indicative of flow separation after the ramp (c.f. Figure 5b [20]). Pressure measurements on the cavity floor (x = 0-40 mm) varied <1% during each dataset, so pressure was assumed to be constant during each data set. Therefore, the ideal gas law was invoked to determine the temperature using the calculated number densities of the major species using the pressure at x determined via linear interpolation of the cavity wall pressure measurements (i.e. the second and third probe locations at x = 1.2 cm and 3.8 cm respectively as shown in Figure 4) for each test location. Since the number densities are in turn a function of temperature, the temperature was determined via an iterative scheme until convergence of ±10 K was met. The RMS temperature values were 9 % in the freestream, where the true variation in temperature is expected to be very small, and 32 % in the cavity, where large variations might be expected (though signals are lower, due to the reduction in total number density, and thus instrument precision will be worse too). The Raman system was calibrated using $H_2$-air and 70% $CH_4$/30% $H_2$-air flames stabilized on a 25-mm-square Hencken burner (Technologies for Research Model RT1x1 ) at ambient pressures, and the resulting temperatures and species mole fractions are shown in Figures 41 and 42 . Each calibration point is for 200 laser shots, where the values of

mean and standard deviation are shown. The calibration factors for each species are shown in Figure 43 with the exception of $CH_4$ which had a constant value of $5.28*10^{20}$ #/$m^3$ taken at room temperature. Sample calibration spectra are also shown in Figure 44.

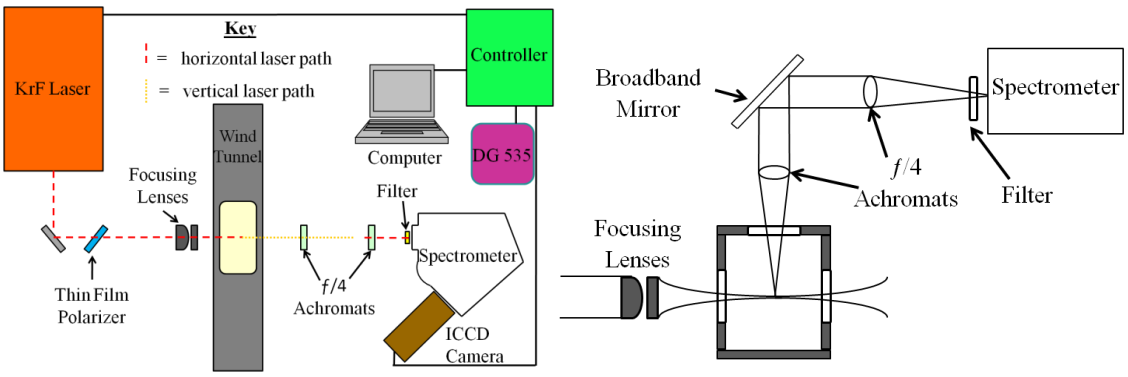


Figure 39: Schematic of the UV Raman experimental system in Research Cell 19 at WPAFB (right) with side view of collection system (left).

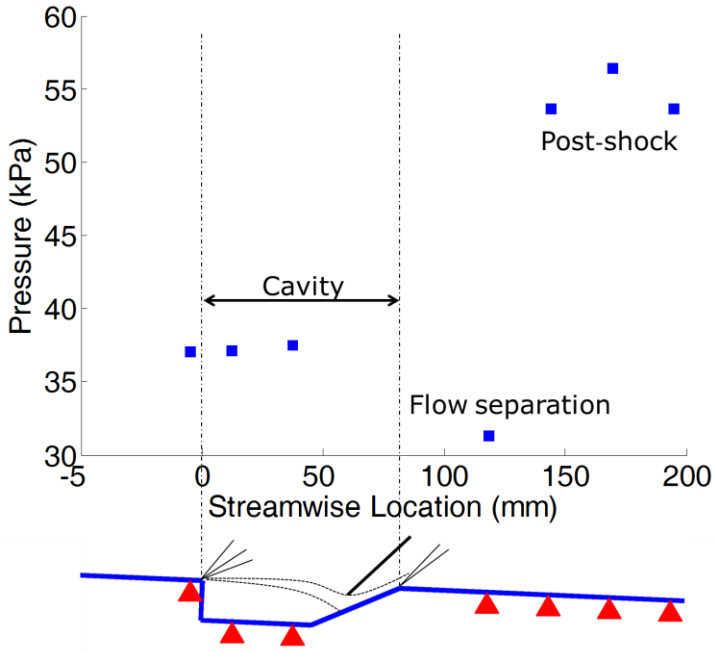


Figure 40: Example mean wall pressure data and the standard deviation of the 1 Hz measurement was generally <1%. Insert shows the pressure port locations (solid triangles) with respect to the cavity. Flow pattern from Figure 5b in [77]

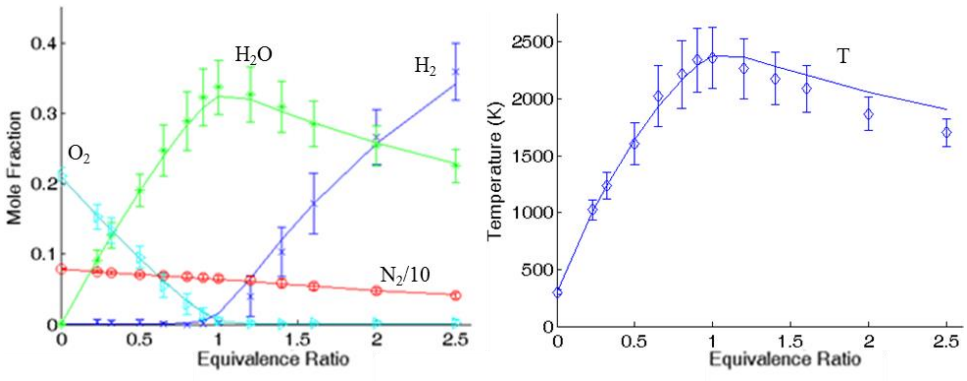


Figure 41: Calibration plots of Raman data over a Hencken burner using a $H_2$-air flame at 1 atmosphere pressure shown with the values at adiabatic equilibrium (lines). The points are the mean values and the bars represent one standard deviation.

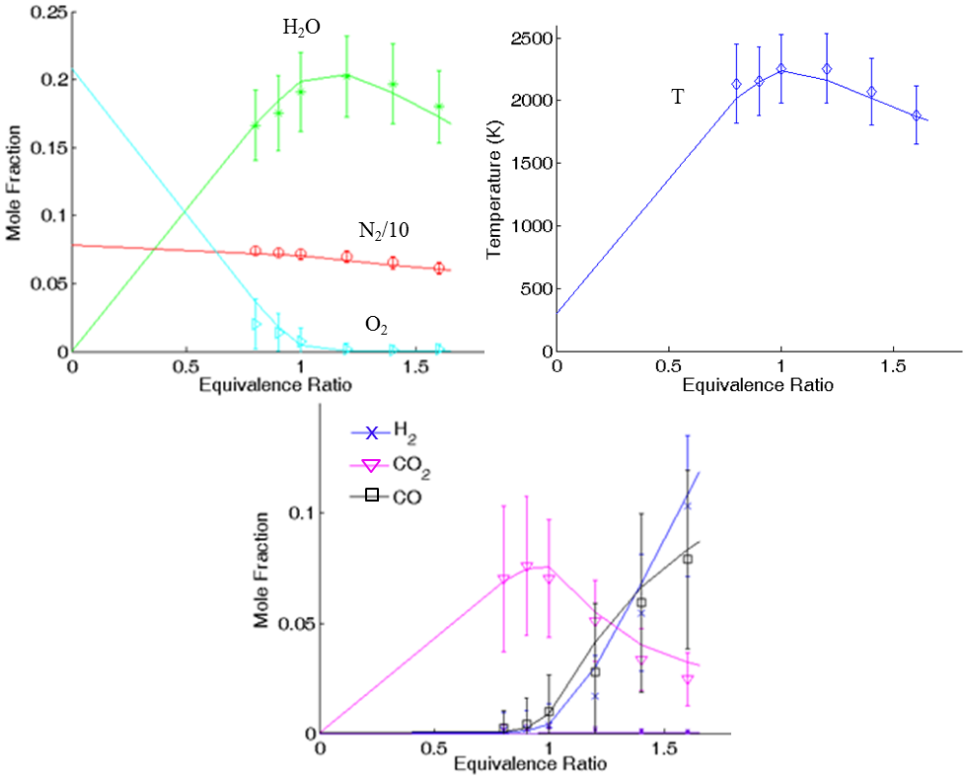


Figure 42: Calibration plots of Raman data over a Hencken burner using a 70% $CH_4$/30% $H_2$-air flame at 1 atmosphere pressure shown with the values at adiabatic equilibrium (lines). The points are the mean values and the bars represent one standard deviation from the mean.

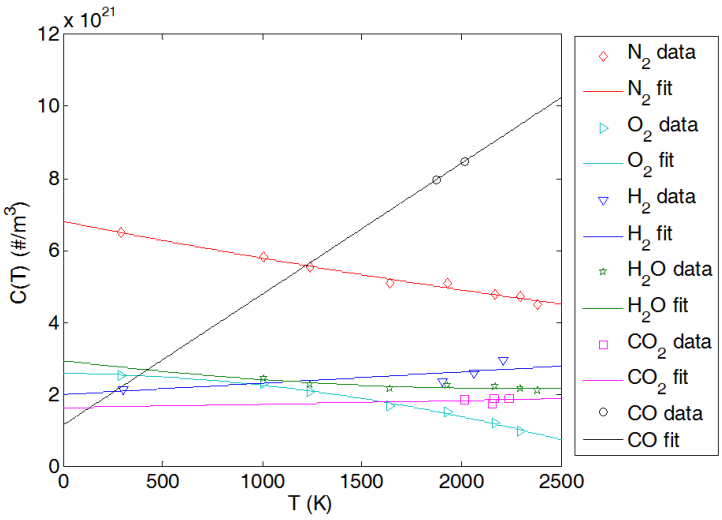


Figure 43: Calibration factors, C(T), vs. temperature obtained from the Hencken burner. The C(T) for $CH_4$ measured at room temperature and assumed to be invariant with temperature.

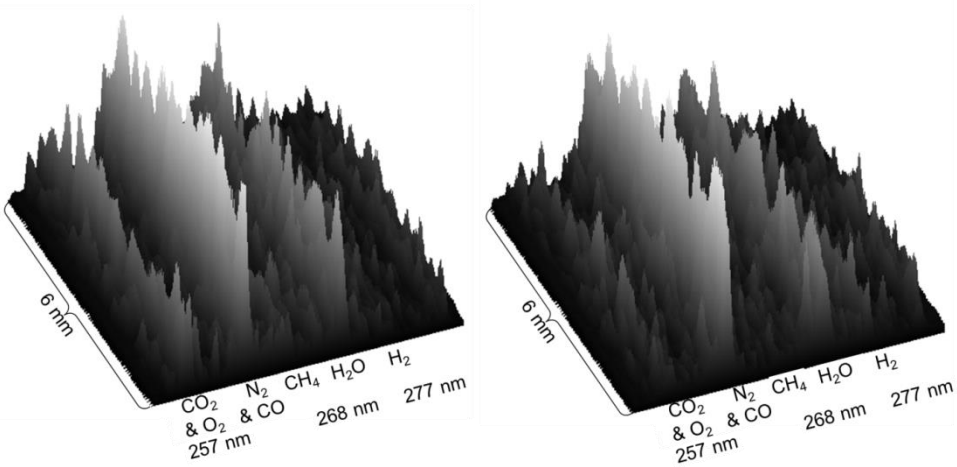


Figure 44: Raw, single-shot line spectral images of calibration data of 70% $CH_4$/30% $H_2$ fuel mixture at ϕ = 1 (left) and ϕ = 1.6 (right).

**UV Raman results**

Typically, the cavity was lit (using two spark igniters located on the cavity floor) with a specific fuel flow rate (for repeatable ignition), the fuel flow rate was then changed to the desired setting, and the Raman images were collected; after the images were collected, the fuel

was shut off, and the cavity was allowed to cool (before making measurements at the next location). At 8 vertical locations (9 locations at x = 3.45 cm), 200 images were collected (from 200 laser shots), starting above the cavity shear layer and ending at the lowest point in the cavity assessable before the beam was clipped by the tunnel side-wall window frame. After a single vertical sweep was completed, the probe region was then moved axially from the upstream to downstream edge of the cavity. The data taken along each Raman line were then divided into 7 line segments, each representing sample volumes of 0.75 x 0.75 x 1.5 $mm^3$. Upstream regions of the cavity suffered from considerable LIF interference shown in Figure 45 alongside an example with minimal interference, and as a result some fraction of the images could not be reliably reduced. Therefore, to increase the available sample size at each probe location, the data from all 7 line segments were individually reduced then bundled together to calculate mean scalar values. The resultant number of reducible images from this bundling is shown in Figure 46. Experimental data of mean and RMS fluctuations are shown in Figures 47-55. As can be seen from the experimental data in Figures 47-49, there is a high concentration of $CH_4$ ($X_{CH4}$) with little $CO_2$ at high temperatures caused by the relatively fast reaction of $H_2$. Furthermore, recirculation near the step in the x-z plane (see counter-rotating vortex shown in Figure 37) can effectively trap unreacted fuel, increasing residence time and creating fuel rich pockets. Therefore, it is suggested that this LIF interference is from soot precursors [e.g., polycyclic aromatic hydrocarbons (PAH)] formed from this rich region, since such a broadband LIF interference has been observed previously from PAH and soot precursors (see Figure 14.6 in [77]); nonetheless, it is noted that no test was performed to confirm PAH fluorescence as being the source of interference and no soot emission is observed in the cavity (even with ethylene fuel, regardless of fuel flow rate). The mixture fraction data in Figure 55 show rich mixtures ($\xi > 0.05$) along the floor and behind the step of the cavity further

corroborating the PAH interference hypothesis. In addition, the mixture fraction steadily decreases along the shear layer, due to turbulent transport of O2 into the cavity, and products out of the cavity. By x = 6 cm, on the ramp, the mixture is lean ($\xi < 0.05$) with little fuel and PAH fluorescence interference, and almost all of the spectra are reducible.

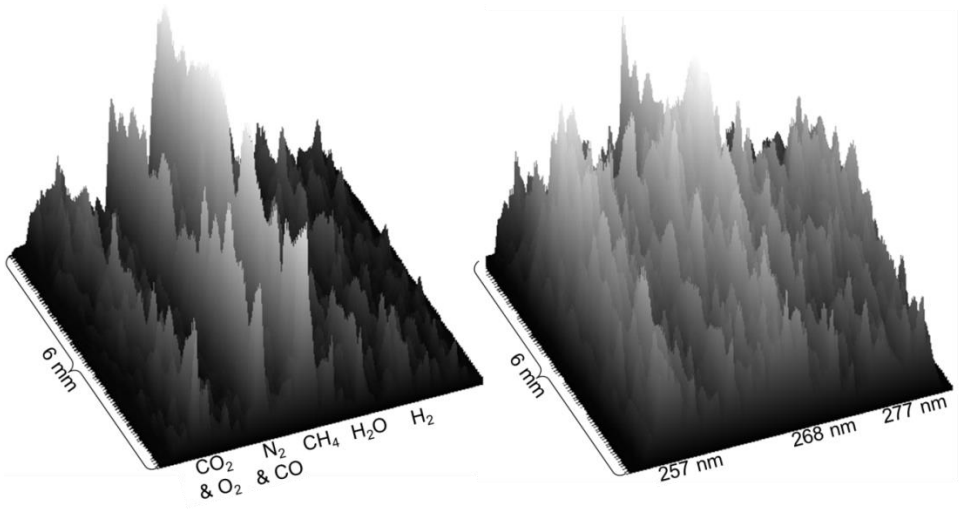


Figure 45: Raman single-shot spectra taken inside the combustor showing a reducible image (left), and an irreducible image (right) due to broadband interference both taken at x = 0.92 cm and y = 0.85 cm. The maximum signal value of the right image is ~20% more than the left.

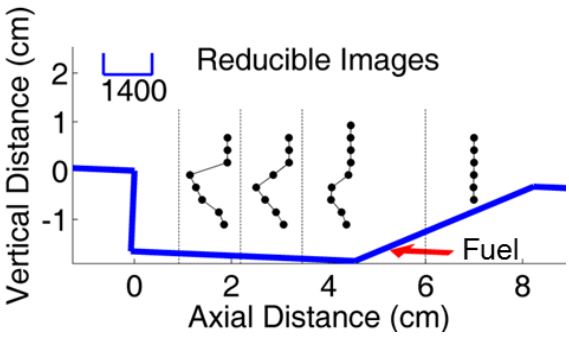


Figure 46: Number of reducible images.

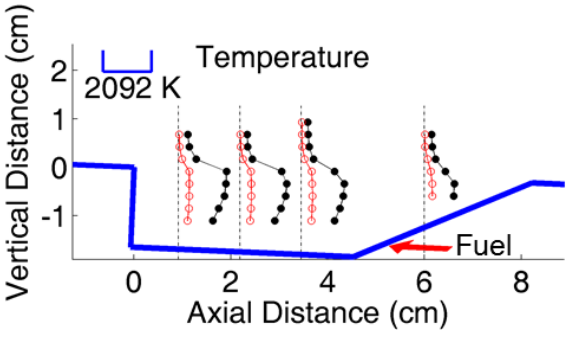


Figure 47: Experimental mean (black) and RMS fluctuation (red) temperature data.

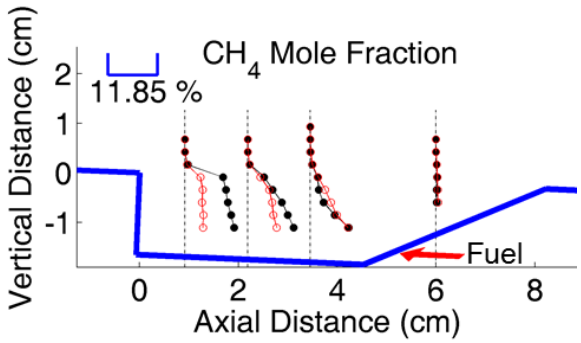


Figure 48: Experimental mean (black) and RMS fluctuation (red) $CH_4$ data.

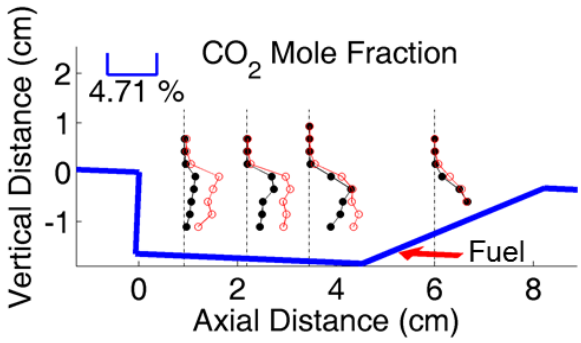


Figure 49: Experimental mean (black) and RMS fluctuation (red) $CO_2$ data.

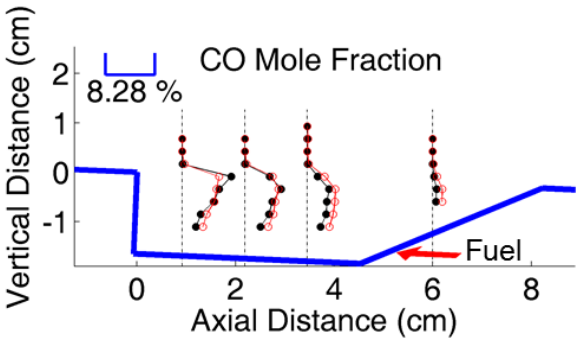


Figure 50: Experimental mean (black) and RMS fluctuation (red) CO data.

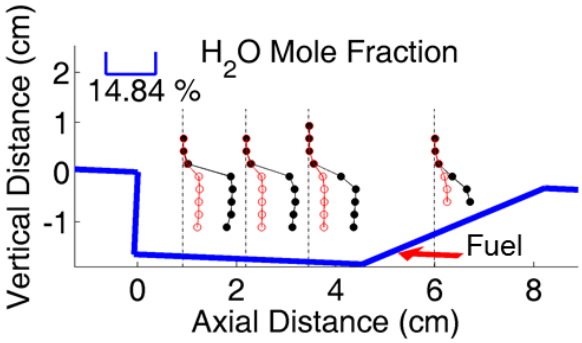


Figure 51: Experimental mean (black) and RMS fluctuation (red) $H_2O$ data.

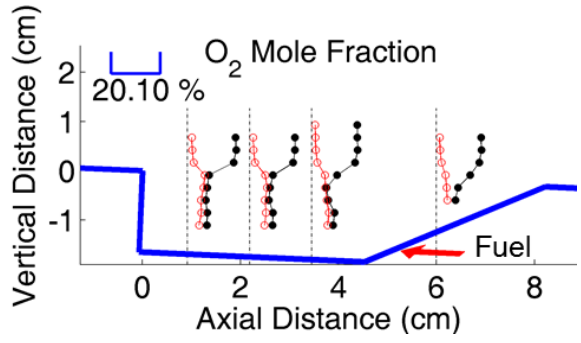


Figure 52: Experimental mean (black) and RMS fluctuation (red) $O_2$ data.

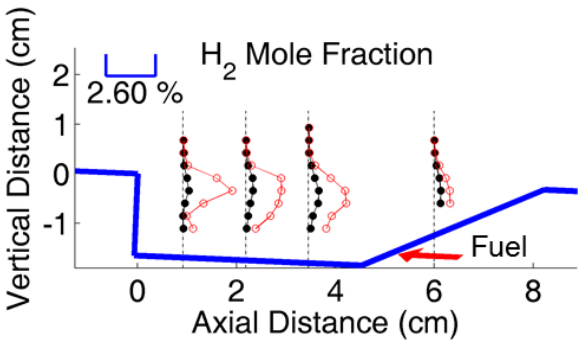


Figure 53: Experimental mean (black) and RMS fluctuation (red) $H_2$ data.

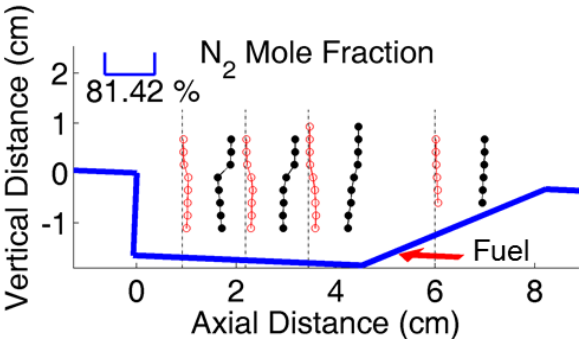


Figure 54: Experimental mean (black) and RMS fluctuation (red) $N_2$ data.

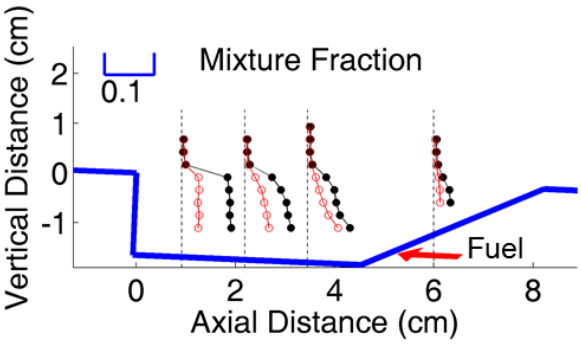


Figure 55: Experimental mean (black) and RMS fluctuation (red) ξ data.

Interpretation of the RMS fluctuation data is complicated by the convolution of chemical reactions and recirculation; therefore, scatter plots will be discussed first. For the sake of analysis, the cavity combustor is divided into four regions to show the extent of mixing/chemistry throughout the combustor with two more locations in the freestream (Point 1) and in the shear layer (Point 2) shown in Figure 56. To reduce data biasing due to the broadband interference, points were chosen such that at least 90% of the images were reducible. The primary recirculation pattern of the cavity is also shown in Figure 56, and illustrates how the fuel jet (shown as the red arrow) would first pass through points A through D in order before either recirculating or exiting through the rear of the ramp. Hot products can also leave the cavity *via* turbulent convection and diffusion through the shear layer (e.g. point 2). Scatter plots for Locations 1, 2, and A through D are shown in Figures 57-62 with lines drawn for the appropriate adiabatic and mixing without reaction scalar values. Values greater than these lines are primarily caused by measurement uncertainty due to low signal levels or to recirculation of hot gases.

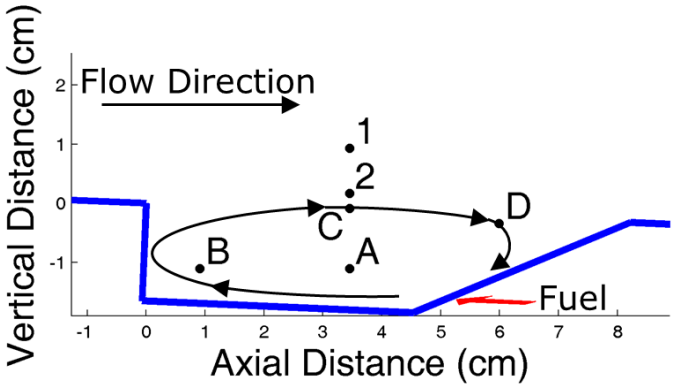


Figure 56: Scatter plot locations with arrows showing fuel injection (red) and the recirculation pattern (black). Point 1 is in the freestream, Point 2 is in the shear layer, and Points A through D are in the cavity.

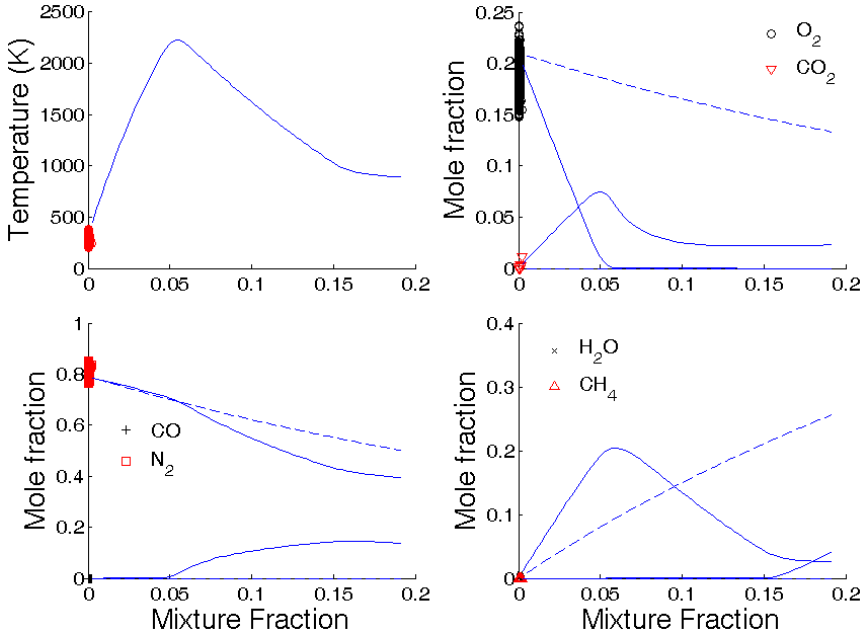


Figure 57: Scatter plots for Location 1 with lines drawn for adiabatic equilibrium (solid) and mixing without reaction (dashed).

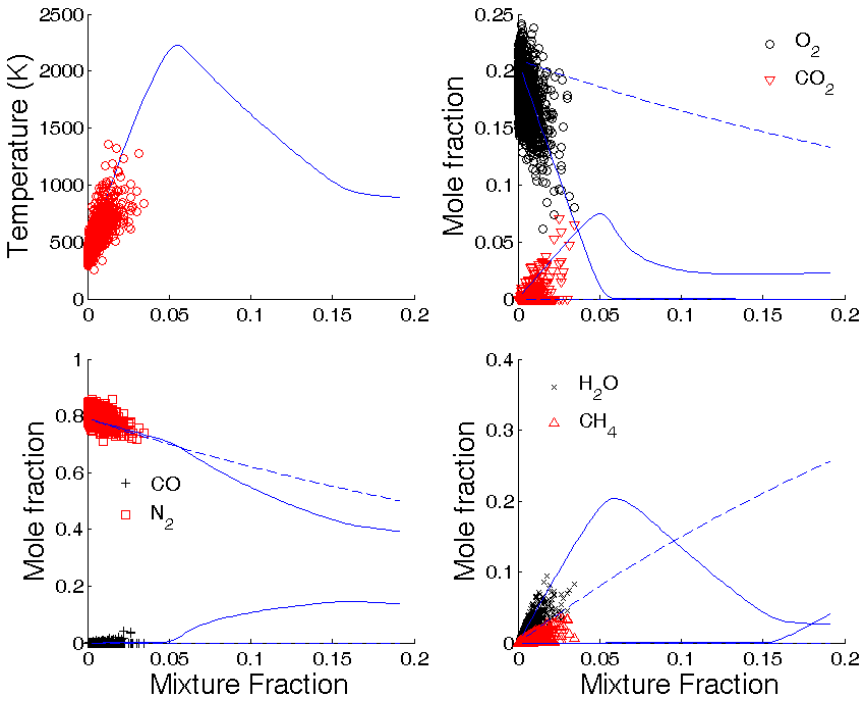


Figure 58: Scatter plots for Location 2 with lines drawn for adiabatic equilibrium (solid) and mixing without reaction (dashed).

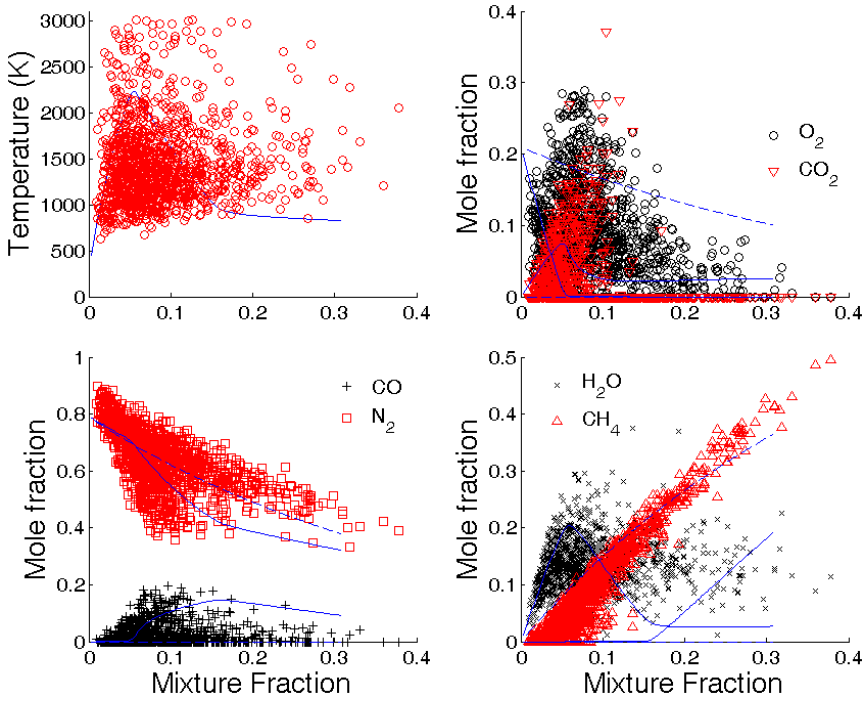


Figure 59: Scatter plots for Location A with lines drawn for adiabatic equilibrium (solid) and mixing without reaction (dashed).

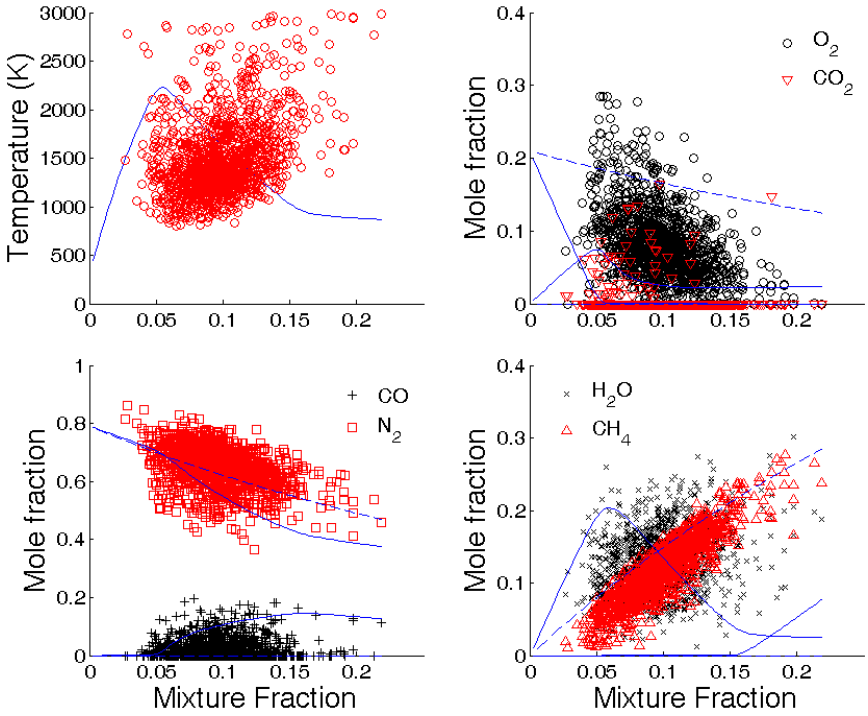


Figure 60: Scatter plots for Location B with lines drawn for adiabatic equilibrium (solid) and mixing without reaction (dashed).

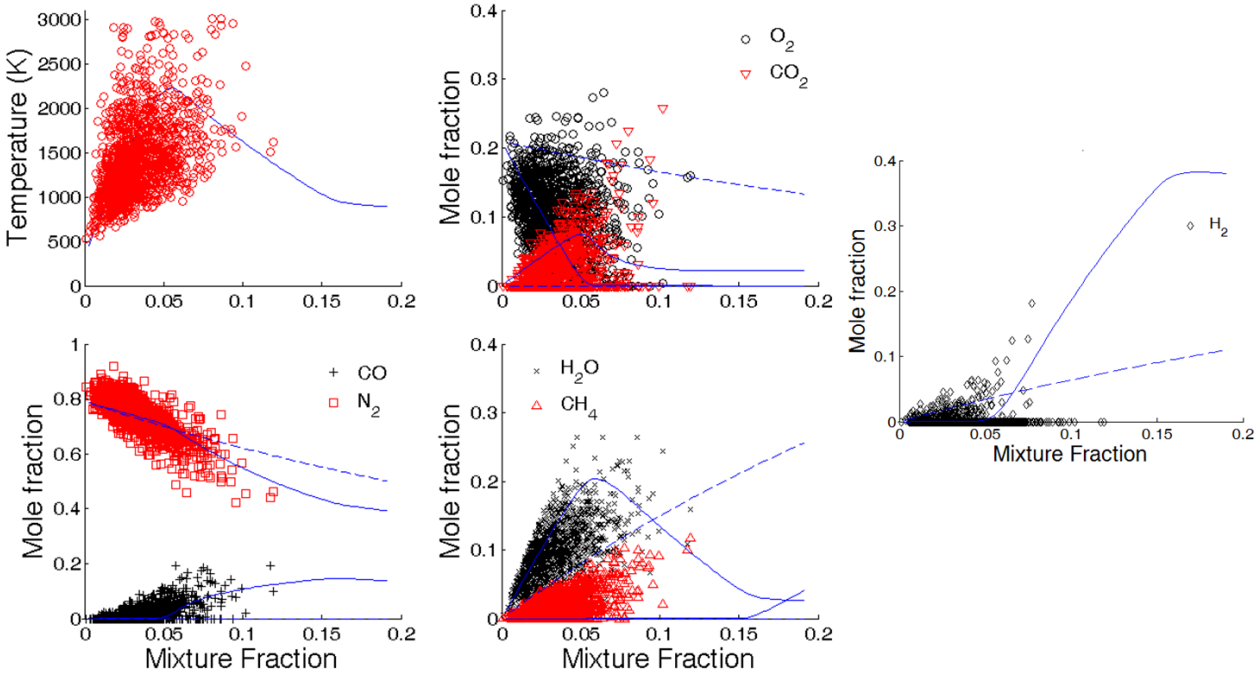


Figure 61: Scatter plots for Location C with lines drawn for adiabatic equilibrium (solid) and mixing without reaction (dashed).

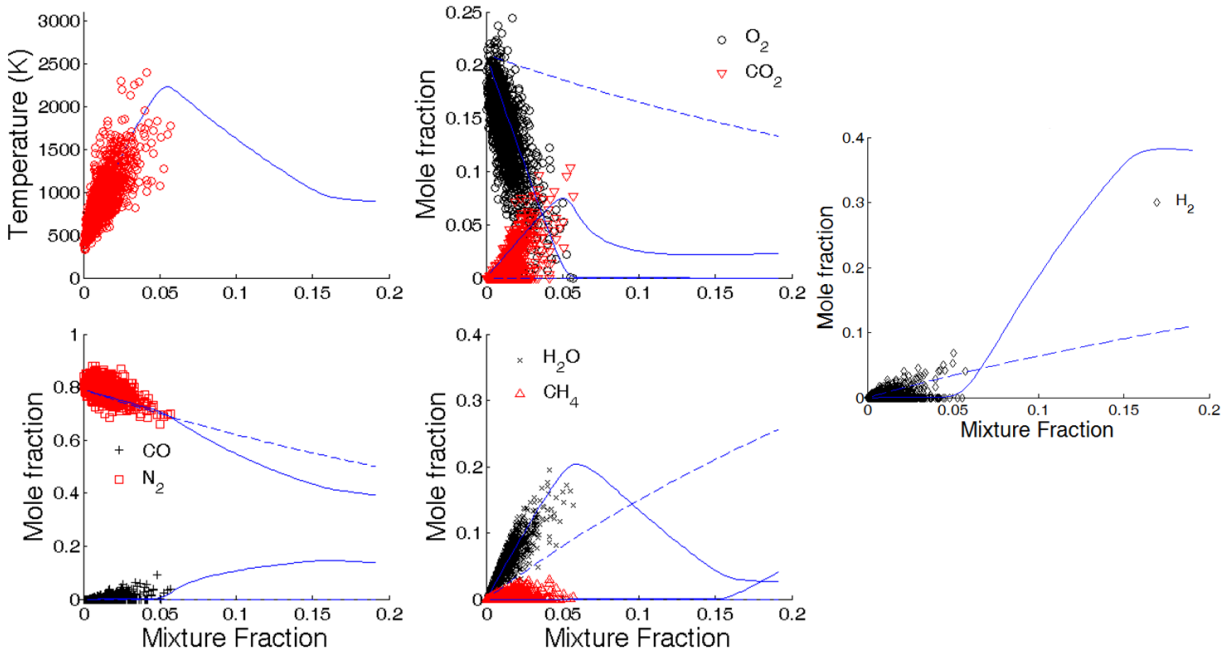


Figure 62: Scatter plots for Location D with lines drawn for adiabatic equilibrium (solid) and mixing without reaction (dashed).

Location 1 shown in Figure 57 , which is located in the freestream where there should be negligible fluctuations, is included to demonstrate the uncertainty of the measurement. Other than a few instances of $CO_2$ due to cross-talk between $O_2$, only $O_2$ and $N_2$ are observed as expected. As a result of the low signal levels, the mean $O_2$ concentration is under-predicated by ~2% and both $N_2$ and $O_2$ RMS fluctuations are ~1.3%. Location 2 shown in Figure 58 is included to demonstrate diffusion across the shear layer. Mean $X_{O2}$ values are roughly half that found in the main air flow over the cavity but are higher than the $X_{O2}$ inside the cavity, while RMS fluctuations are almost twice as large in the shear layer as in the main flow. Temperature mean and RMS values are also elevated relative to the main flow but are lower than in the cavity. Trace amounts of $CH_4$, and products are also seen in the shear layer as opposed to the main flow.

At Location A shown in Figure 59, the scatter plots demonstrate that this region fluctuates between partially reacted and unreacted mixtures. The $CH_4$ data is almost entirely along the *mixing without reaction line*, indicating that most of the $CH_4$ has not reacted at this point in the cavity although it has started to mix with a lot of points below $\xi = 0.5$. Temperatures and $X_{H2O}$ vary from near adiabatic to unreacted for $\xi < 0.15$, whereas for $\xi > 0.15$ there are super-equilibrium temperatures and $X_{H2O}$ values. CO and $CO_2$ values are between the mixing without reaction and equilibrium lines for lean conditions, but with super-equilibrium $CO_2$ values between $0.5 < \xi < 0.1$. Since little $CH_4$ has reacted at this location, the high temperatures and $X_{H2O}$ must be from either $H_2$ combustion or from recirculation, and the CO and $CO_2$ concentrations must primarily be from recirculated products.

At point B shown in Figure 60, the $CH_4$ is still largely unreacted although more air has been entrained into the fuel jet than at point A. $CH_4$ is most likely still present here in spite of the high temperatures and available oxygen due to a ~270 µs residence time (estimated based the ~4 cm distance between point B and the fuel injection and using the jet exit velocity of 150 m/s). Both the $X_{O2}$ and the $X_{CO}$ profiles indicate partially reacted mixtures, while there is little $CO_2$ observed in this region since CO oxidation is significantly slower than the competing $CH_4$ breakup. Super-equilibrium values for temperature are probably due to interference and measurement error. The absence of $CO_2$ is probably caused by the fuel jet sweeping away recirculated products. Since there is a comparable concentration of CO at Points A and B, it's unlikely that the disappearance of $CO_2$ at Point B is caused by dissociation.

At Location C shown in Figure 61, while some of the $CH_4$ has yet to react the mixture is predominantly lean and reacted or at least partially reacted. When the flow moves to Location D shown in Figure 62, the $O_2$ and CO data primarily follow the adiabatic equilibrium

lines while temperature and $CO_2$ still show partial reaction. The scatter in the $CO_2$ data in Figure 62 indicates that CO oxidation occurs between Locations C and D, which is further corroborated by the $CH_4$ data going to adiabatic equilibrium between these points. The $X_{H2}$ scatter plots, included for Locations C and D, indicate significant concentrations of partially reaction of $H_2$ which was not found at the other locations. The presence of $H_2$ near the shear layer at these points can be explained by the water shift reaction shown in Equation 28:

$$CO_2 + H_2 \leftrightarrow H_2O + CO \qquad 28$$

The excess $H_2$ above 30% in the equilibrium curves (see Figures 61 and 62) are also due to this water shift reaction

Returning to the RMS fluctuation plots in Figures 47-55, mixture fraction and $CH_4$ fluctuations peak near the injection location due to intense fuel/air mixing with less intense fluctuations near the step before $CH_4$ starts to react. The profiles for CO fluctuations and concentrations are similar and in general there is less CO when $X_{CH4}$ is high, as expected, due to CO oxidation kinetics. $X_{CO2}$ fluctuations peak in regions of CO oxidation, primarily near the shear layer or in regions of recirculation near the ramp, while fluctuations lower in the cavity are most likely due to recirculation or to displacement caused by the fuel plume.

The temperature, $X_{H2O}$, and $X_{O2}$ RMS profiles are flatter than profiles of other scalars. Inspection of the scatter plots would indicate that the initial $X_{O2}$ fluctuations are due to fuel/air mixing or the consumption of $O_2$ in the chain-branching reaction steps, while the fluctuations further away from the injectors are due to slow reacting $CH_4$ or turbulent transport of $O_2$ across the shear layer. Inspection of Location A demonstrated that fluctuations in both $X_{H2O}$ and temperature were due to either the reaction of injected $H_2$ or to recirculation. Additionally, the

scatter plots showed that $H_2O$ was not fully at equilibrium at Location D over the ramp (although comparisons between Locations C and D indicate that $H_2O$ is approaching full equilibrium) due to continued formation from late burning $CH_4$ and from consumption due to water shift reactions and oxidation of CO. The "flatness" of the $X_{H2O}$ and $X_{O2}$ RMS profiles is probably due to recirculation/turbulent transport and the slow reaction of $CH_4$. The "flatness" of the temperature RMS profile can be explained with similar arguments. Considering that heat release primarily occurs as a result of $H_2O$ and $CO_2$ formation, this flatness of the Xi profiles could be because product formation is spread out across the cavity. This may also be a consequence of the fast reaction of $H_2$ and relatively slow reaction of $CH_4$. While this was an expected result, the use of only temperature and/or PLIF measurements would not be sufficient to prove this behaviour.

## Conclusions

UV spontaneous Raman scattering measurements of temperature and major species concentrations ($H_2$, $CH_4$, $CO_2$, CO, $O_2$, and $N_2$) were recorded over a ramp close-out cavity in the Mach-2 scramjet test section of Research Cell 19 at Wright Patterson Air Force Base. Raman scattering has intrinsically low signal levels especially at the low pressure, ~1/3 atm, of the cavity. While the presence of broadband interference further exacerbated the signal quality and increased measurement uncertainty, some conclusions on the combustion phenomena in the scramjet combustor were determined.

The cavity flow field was directly fueled from the ramp using a fuel composed of 70% $CH_4$ and 30% $H_2$ (by volume). Results showed that $H_2$ fuel quickly reacted while the $CH_4$ fuel reacted slowly. $CH_4$ was largely unreacted by the time it reached the leading edge of the cavity,

forming a fuel-rich region along the floor and behind the step at high temperature due to the fast reaction of $H_2$. This region of hot, unreacted $CH_4$ may have resulted in production of polycyclic aromatic hydrocarbons (PAH), thus creating the broadband interference observed in this region.

Measurements of mixture faction indicated that the cavity was rich overall, however turbulent transport of $O_2$ across the shear layer eventually resulted in lean mixtures over the ramp. The path of the injected fuel was traced out through the cavity using scatter plots, and $CH_4$ was mainly unreacted near the injectors and behind the step, partially reacted by the midpoint of the cavity below the shear layer, and reacted near the ramp where the products will either exit the cavity or recirculate. Due to high concentrations of unreacted $CH_4$, CO concentrations accumulated until the $CH_4$ reacted. Comparisons between CO and $CO_2$ concentration profiles showed that CO began to oxidize after the $CH_4$ concentrations decreased near the midpoint of the cavity below the shear layer and was nearly gone by the ramp, although there was still scatter in the $CO_2$ concentration. While the $H_2$ fuel quickly reacted near the injectors, $H_2$ concentrations were observed where CO began to oxidize, probably due to the water shift reaction. Data taken in the shear layer demonstrated turbulent transport across the shear layer of $O_2$ into the cavity and hot products into the main flow of tunnel. Fluctuations in measured temperature and $O_2$, and $H_2O$ concentration were fairly constant throughout the cavity, primarily due to the slow reaction of $CH_4$ and to a combination of recirculation of hot products and turbulent transport of $O_2$ across the shear layer.

Even though the $H_2$ fuel component quickly reacted providing the high temperature and radicals to sustain the reaction, the slow reaction of CH4 delayed the formation of both CO and $CO_2$. Additionally, these results show the importance of measuring all

major species when multi-component fuels are used in order to properly determine the combustion behaviour and progress even in the relatively simple fuel mixture used in the current experiment.

# CHAPTER 4: VELOCIMETRY DEVELOPMENT

## Molecular tagging techniques

In MTV, a laser excites molecules in the gas to create a tag line or grid. In environments where the tag fluorescence or phosphorescence is rapidly quenched (e.g., oxygen containing gas at atmospheric pressure), MTV methods require a two-step process where one laser "writes" a tag line (usually via dissociation) and a second laser "reads" the displaced tag line (usually a photo-product from the write phase) [82, 83]. For low quenching environments (e.g., low pressure or pure nitrogen at atmospheric pressure), the tag line fluorescence or phosphorescence can persist long enough to record the tag line movement without a second laser [84, 85].

MTV can be accomplished by direct seeding of the gas using biacetyl [84], $N_2O$ [86], $NO_2$ [87], NO [85, 88], tert-butyl nitrate [89] and other molecular seeds [90-92]. However, these seeds can be expensive, toxic, damaging to the experimental apparatus, or not viable in reacting flows. Therefore, unseeded methods have also been developed and implemented using linear processes to create $O_3$ [93], OH (HTV) [78, 93-96] and nonlinear techniques to make, NO (APART) [97, 98], OH [99, 100], vibrationally excited $O_2$ (RELIEF) [101-103], and electronically excited $N_2^+$ using nanosecond [104] and femtosecond (FLEET) [105] lasers.

One issue that has plagued unseeded MTV is obtaining usable signal-to-noise ratios in hot gas or combustion regions where there may be high backgrounds of the chosen tracer, insufficient quantities of the write molecule, or other interferences. For example in conventional HTV, an ArF laser photodissociates $H_2O$ into ground state grid of OH (v=0) that may be obscured in high temperature flames by naturally occurring background OH [33]. In laminar flames or in environments which are highly repeatable, a mean image without the write laser can be

subtracted from a mean image with the write laser to obtain mean velocity data. However, mean data are often insufficient in turbulent flames and single-shot data are required to obtain instantaneous velocities.

One way to acquire single-shot data is to create vibrationally excited molecular tracers that can be differentiated from the background in flames. While MTV methods have been developed to produced vibrationally excited $O_2$ ($\gamma_{vib}$ = 1556 $cm^{-1}$) [102] and NO ($\gamma_{vib}$ = 1877 $cm^{-1}$) [106], their relatively low vibrational frequency ($\gamma_{vib}$) has led to tag line obscuration under high temperature gas conditions. For example, in RELIEF which uses vibrationally excited $O_2$, the practical gas temperature limit is 750 K [102]. The hydroxyl radical, OH, has a high vibrational frequency ($\gamma_{vib}$ = 3700 $cm^{-1}$) and vibrationally excited OH is projected to be detectible against ground state OH at flame conditions. Therefore, in the present experiment, a variant of hydroxyl tagging velocimetry (HTV) is developed where water is dissociated using two photons (248 nm) from a KrF excimer laser creating vibrationally excited OH (v=1) to use as the molecular tag. This new process is called Vibrationally Excited Hydroxyl Tagging Velocimetry (VE-HTV).

**Tag formation system**

Previously, HTV measurements have been made using either 1 x 193 nm or 2 x 248 nm photons [33, 78, 93-96, 99, 100, 107] to dissociate water to form the OH (v = 0) photofragment that is the molecular tracer via either the predissociative Ã state for 1 x 193 nm excitation or the predissociative Č state for 2 x 248 nm excitation. In this work, 2 x 248 nm photons excite water to the electronic Č as shown in Figure 63 state which results in at least 50% vibrationally hot photofragments (v ≥ 1)[108]. The primary difference between the current work and previous efforts using 2 x 248 nm excitation [99, 100] is the use of OH tracers in the first vibrationally

excited state instead of the ground state. The physical process of forming vibrationally hot photofragments via the Č state is described elsewhere [109, 110].

The schematic of the VE-HTV system and a diagram of the write/read processes of HTV are shown in Figure 64. A Coherent COMPex 150T KrF excimer laser is used to produce the write line at 248 nm (~100 mJ/pulse) and focused with a 0.5 m lens. Burn patterns taken at the focal point show a beam spot size of ~400 µm. However, due to the two-photon dependence of the method, the tag line image thickness is closer to ~230 µm. The strong $H_2O$ absorption lines mentioned in [109, 110] are outside the tuning range of the KrF laser. The KrF laser is tuned to a weaker $H_2O$ absorption line in the center of its range to ensure maximum locking and laser performance leading to consistent levels of $H_2O$ absorption and subsequent photodissociation.

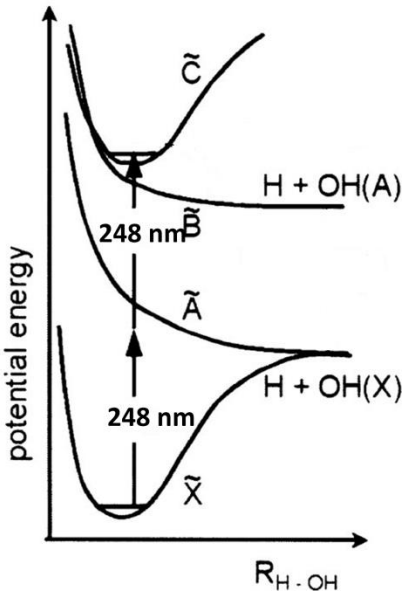


Figure 63: Energy level diagram demonstrating the 2 x 248 nm photon dissociation process of $H_2O$ used in VE-HTV.

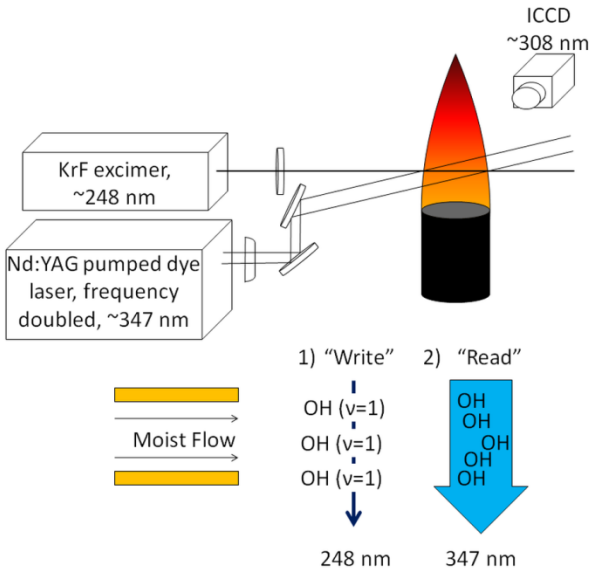


Figure 64: Experimental schematic of the VE-HTV system (top), and a diagram of write/read process (bottom).

A Continuum Powerlite 9010 Nd:YAG with a second harmonic generator is used to pump an ND6000 dye laser with a LDS-698 dye. The dye laser output is frequency doubled to ~347 nm for the read sheet (~4 mJ/pulse, 9 ns). This wavelength is centered in the OH $A^2FSD^+$ (v' = 0) ← $X^2Π$ (v" = 1) ro-vibration band. A 150 mm cylindrical lens and a 1 m spherical lens are used to form a 150 µm thick read sheet at the probe location.

The tag line is imaged by 308 nm fluorescence from the OH $A^2FSD^+$ (v' = 0) → $X^2Π$ (v" = 0) transition induced by the 347 nm read sheet laser. The read image is captured using a Cerco 2.8 ƒ/# (100 mm focal length) in front of a Princeton Instruments PIMAX-4i ICCD camera binned 4x4 so that each effective pixel is 114.6 µm x 114.6 µm square in the read plane. Stray room light and scattered read sheet laser light (347 nm) are blocked by a UG-11 filter and a 325 nm shortpass filter (Asahi Spectra, ZUS0325-shortpass 325nm).

All of the VE-HTV measurements are made in Hencken burners (either 12.5 mm dia. or 25 mm square cores) producing $H_2$/air flames. The Hencken burner has a fuel/air core with separate passages for fuel and air. The $H_2$ fuel flows through an array of micro-tubes contained in an air channel honeycomb. The fuel and air mix and burn at the burner surface with negligible surface heat transfer. Downstream of the flame, an adiabatic equilibrium region of hot gases forms. The fuel/air core is surrounded by a co-flow channel to shield the hot post flame gases in the core. All of the OH (v=1) tag lifetime and spectral identification measurements are made downstream of the burner surface where the flame radicals recombine to produce adiabatic equilibrium gas [111]

**OH (v" = 1) formation, yield, lifetime and tag line width**

Examples of single-shot images of VE-HTV tag formation in the $H_2$/air post flame zone of a 25 mm square core Hencken burner are shown in Figure 65. The VE-HTV method forms long tag lines (2 cm) in the post flame (~ 6 cm downstream of the burner surface). Due to the inverse square dependence of $H_2O$ photodissociation on the write laser diameter, the tag formation concentration is strongest in the center (1 cm) portion of the line. The tag lines are shown for a 10 μs delay typically used in velocity measurement. The tag lines show good Signal-to-Noise Ratio and are clearly seen against the background in flames at lean (φ = 0.75, SNR = 13.5:1), near stoichiometric (φ = 0.95, SNR = 4.3:1) and rich (φ = 01.51, SNR = 3.1:1) conditions. The flame is laminar with Reynolds numbers, Re < 2000 (Re=UD/υ where $U_o$ is the average jet exit velocity, D is the jet diameter and υ is the kinematic viscosity). The near stoichiometric flame condition (φ = 0.95) has a gas temperature of 2334 K and an equilibrium OH concentration of $[OH]_{eq}$ = 2 x $10^{16}$ #/$cm^3$.

Figure 66 shows the observed OH (v=1) tag signal intensity vs. equivalence ratio (φ) at two time delays (50 ns and 1000 ns) in the post flame zone of a Hencken burner (12.5 mm core dia.) burning $H_2$/air. A 1.5 mm length of line is measured in the burner centerline, 45 mm downstream of the burner surface where the post flame conditions are at adiabatic equilibrium. For lean flames, the OH (v=1) tag signal intensities generally follow the temperature curve rather than the $H_2O$ number density curve, $[H_2O]$. For rich flames, the signal decreases with increased φ faster than the corresponding decrease in either temperature or $[H_2O]$. Furthermore, the OH tag intensity decreases more rapidly with delay time under rich conditions than lean conditions. Under rich conditions, the OH tag will react with $H_2$, decreasing the signal strength of the tracer as discussed in previous HTV papers [33, 93].

In Figure 66, the equilibrium concentrations of OH (v=1) and total OH are also shown. At stoichiometric conditions, the vibrationally excited equilibrium OH is about 10% of the total OH concentration. Thus the tag lines in Figure65 can be imaged over a small concentration of equilibrium excited state OH (v=1) rather than the much higher total concentration of equilibrium OH. The read sheet background seen in Figure 65 follows the trends for OH (v=1) in Figure 66 for lean and stoichiometric conditions. However for rich conditions, the OH tag line reacts with $H_2$ and the tag disappears more rapidly [33]. This may explain the apparent high read sheet background seen for rich conditions in Figure 65.

To compare the experimental results with theory, two-photon cross-sections (δ) for each of the low lying vibrational modes of water would be required. To the authors' knowledge, no such cross sections have been measured for 248 nm laser light. While cross-sections at higher wavelengths are available [112, 113] which can be scaled to approximate the cross-section at 248 nm, the values are for liquid $H_2O$ with no dependence given for the vibrational excitation expected at flame temperatures. Additionally, these estimates would need to be further modified for rich conditions to account for the signal decay observed from chemical reactions.

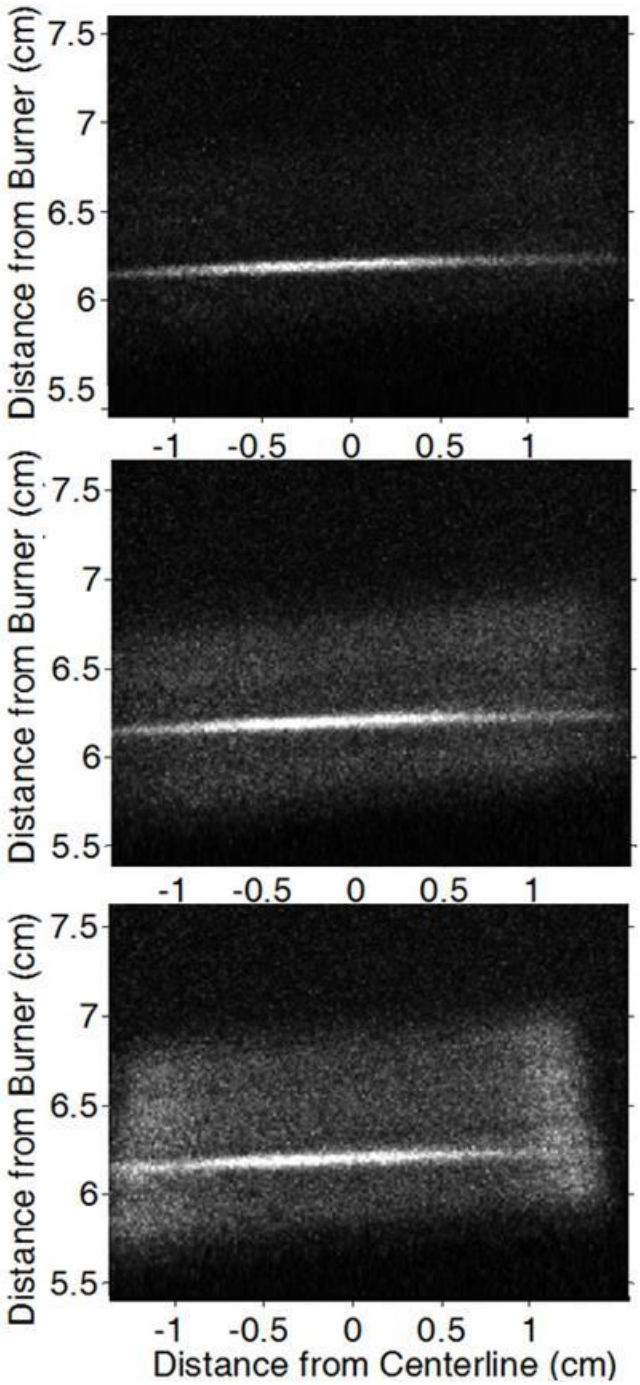


Figure 65: Single-shot VE-HTV images at φ = 0.75, 0.95, and 1.51 (top, middle, and bottom respectively) in a $H_2$/air laminar post flame zone formed in a 25 mm square Hencken burner. The time delay is 10 μs and the Reynolds numbers are Re = 1,900, 1550, and 1050 respectively.

The lifetime of the OH (v = 1) photofragment at lean and rich post-flame zone conditions (φ = 0.69, 1.23, and 2.34) can be found in Figure 67 taken at the same flame location as Figure 66. The half-life of the tag decreases from ~8 µs at φ = 0.69 to ~6 µs at φ = 1.23, whereas at φ = 2.36 the half-life of the tag is only ~2 µs. This reduction in tag lifetime in richer flames further supports the notion that chemical reactions, especially with $H_2$, are affecting the OH photofragment. Lifetimes of the OH (v = 1) tracer in lean flames are significantly shorter than have been reported previously using the ground state OH (v = 0) tag [33]. However at rich conditions, both OH (v=1) and OH (v=0) tags are depleted more rapidly due to chemical reaction with $H_2$. Note that even at a time delay of 10 µs, single-shot tag lines are clearly seen in Figure 65.

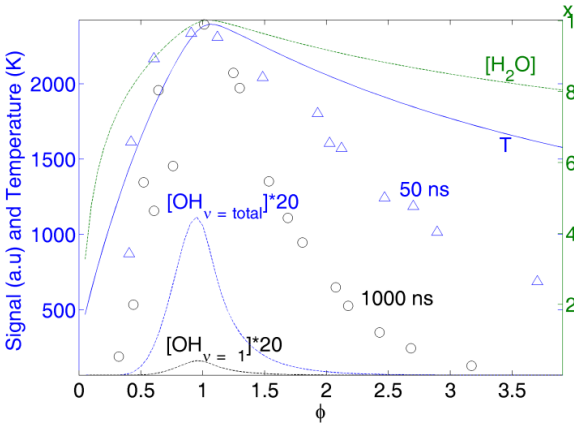


Figure 66: Plot of OH (v = 1) signal intensity vs. equivalence ratio at 1000 ns and 50 ns time delays with adiabatic values for temperature and species data. Measurements are in the post flame zone of a laminar $H_2$/air flame formed by a Hencken burner (12.5 mm dia.)

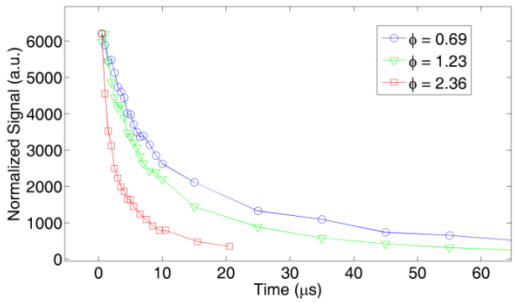


Figure67: Lifetime of the OH (v = 1) tracer at different equivalence ratios in the post flame zone of a laminar $H_2$/air flame formed by a Hencken burner (12.5 mm dia.).

To spectrally identify the OH (v = 1) tag, an OH $A^2FSD^+$ (v' = 0) ← $X^2\Pi$ (v" = 1) a laser-induced fluorescence (LIF) scan of the photofragments is shown in Figure 68 alongside a LIFBASE

simulation (2331 K) [114]. These measurements are made 20 mm downstream in a larger Hencken burner with a 25.4 x 25.4 mm core using a 2 μs delay. The simulated and measured spectra have good correspondence confirming the formation of the OH (v=1) tag. The strongest fluorescence signal is obtained when exciting the combined $Q_1(7)$ and $P_1(2)$ line at 346.81 nm (denoted by the horizontal arrow in Figure 68) and this line is used for the remainder of the experiments.

In Figure 69, the tag line width vs. time is plotted in a lean φ = 0.69 $H_2$/air flame (T = 1997 K, $H_2$ = 5.2 LPM, Air = 17.8 LPM, Re = 2,170) with lines for binary diffusion of both the OH and H photofragments into either $N_2$ or $H_2O$ (the two major species comprising 93.9% of the mixture). The binary diffusion is approximated using the coefficients from Cantera [115] and the following equation for Gaussian beam diffusion of molecular tag lines from [102]:

$$\omega^2 = 8\tau D \ln(2) + \omega_0^2 \qquad 29$$

Here ω is the tag line width, τ is the time delay, and D is the diffusion coefficient ($D_{OH, N2, 1997K}$ = 7.7 $cm^2/s$, $D_{H, N2, 1997K}$ = 30.7 $cm^2/s$, $D_{OH, H2O, 1997K}$ = 10.4 $cm^2/s$, $D_{H, H2O, 1997K}$ = 39.7$cm^2/s$). The value of $\omega_0$ is determined from the measured line width at 50 ns (230 μm). The actual line width is larger than those predicted from diffusion for both OH and H photofragments. However, at long delays, the theoretical width approaches the experimental width. Differences between the experimental and theoretical results are most likely due to initially faster diffusion from steeper concentration gradients arising from the non-Gaussian KrF laser profile.

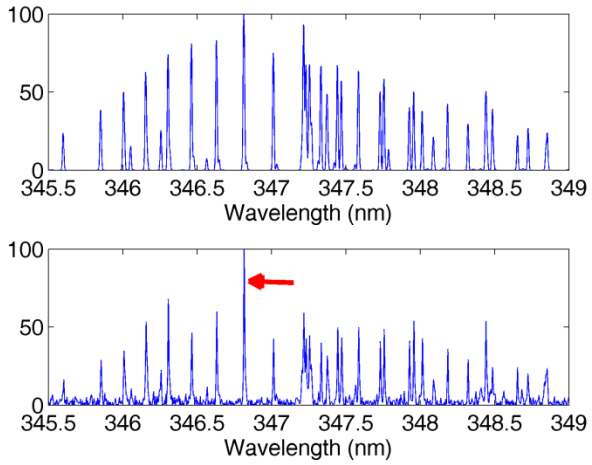


Figure 68: Comparison of simulated (top) and experimental (bottom) LIF scans of OH (v = 1) in the post flame zone of a laminar $H_2$/air (φ = 0.933, T = 2331 K) flame at atmospheric pressure. Measurements made 20 mm downstream in a 25 mm square Hencken burner. The combined $Q_1(7)$ and $P_1(2)$ line (346.8 nm), indicated by the red horizontal arrow, was used for the experiments.

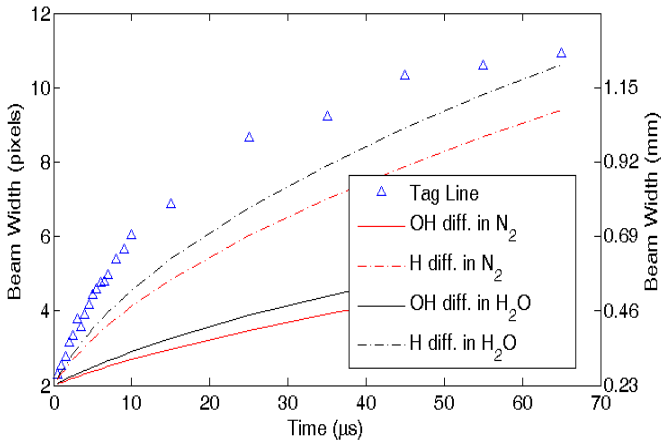


Figure 69: Line width of the OH (v = 1) tracer vs. time in the post flame zone of a lean (φ = 0.69) $H_2$-air laminar flame (12.5 mm burner) with corresponding lines for binary diffusion of the OH photo-fragments into both $N_2$ and $H_2O$.

**Application over a turbulent jet**

A preliminary demonstration of the VE-HTV method is made in a lean (φ = 0.78) premixed $H_2$/air turbulent jet flame formed in the Hencken burner (Re = 26,550, D=12.5 mm

dia., $U_o$ = 38.7 m/s, $H_2$ = 70 LPM, Air = 215 LPM). To stabilize the flame, a rich methane-air pilot ($\varphi$ = 1.2, $CH_4$ = 1.3 LPM, Air = 8.9 LPM) is supplied to the 6.2 mm wide annular coflow surrounding the 12.5 mm dia. core Hencken burner. At this high Reynolds number (Re = 26,550), the flame is turbulent and unsteady.

In Figures 70 and 71, single-shot measurements of the VE-HTV tag line are made in the turbulent premixed flame at x= 10.5 cm downstream (x/D = 8.4) for two different delay times (2 μs and 10 μs). For the 2 μs time delay, (Figure 70) the tag line is clearly seen with few breaks in the line. There are no clean breaks in the central portion (1 cm) of the line where the written tag line intensity is the highest. Even when there are apparent breaks, one can see the tag line at a diminished intensity. In the center of the line, a SNR of 4 or higher is achieved that is sufficient for accurate velocity measurement [116] when the line is displaced about 10 pixels. For the 10 μs time delay (Figure 71), the tag line is more frequently broken. Some line breaks seem to be absent of the OH tag. These line breaks are probably due to out-of-plane motion displacing the line outside of the read sheet. Line breaks due to out of plane motion can be avoided by thickening the read sheet (or retro-reflecting the read sheet) to increase the read volume thereby obtaining single-shot contiguous lines and instantaneous velocity [78]. This modification was not done in this preliminary work.

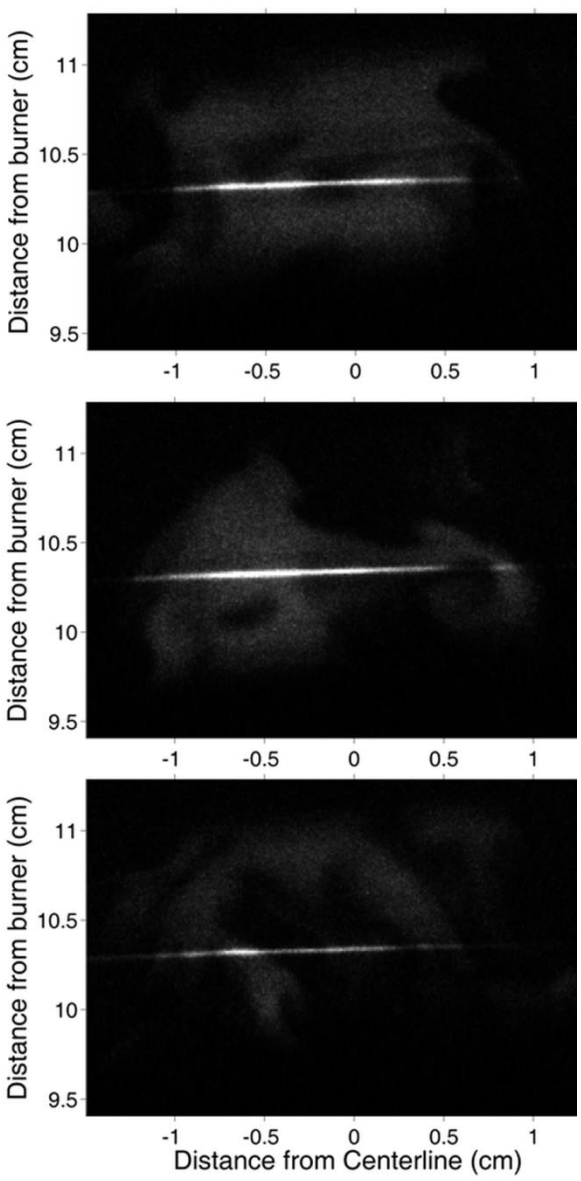


Figure 70: Single-shot VE-HTV images (2 µs delay) in a lean (φ = 0.78) $H_2$/air turbulent premixed flame (Re = 26,550, Air = 215 LPM, $H_2$ = 70 LPM) formed by a Hencken burner (12.5 mm dia.) with a low-flow methane-air pilot.

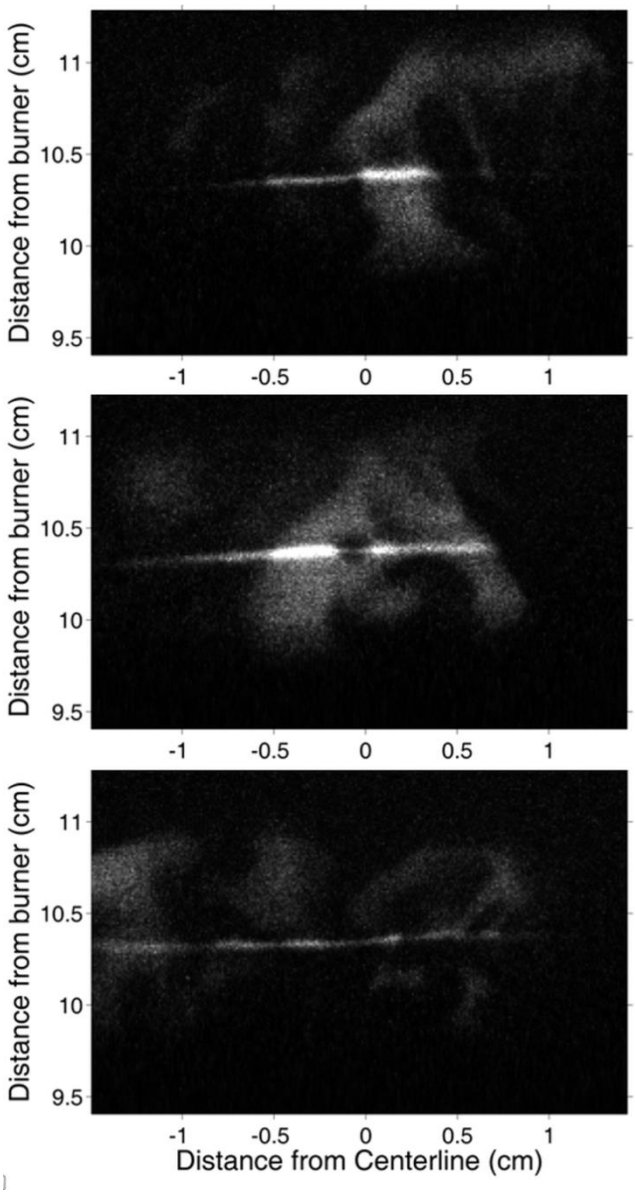


Figure 71: Single-shot VE-HTV images (10 µs delay) in a lean (φ = 0.78) $H_2$/air turbulent premixed flame (Re = 26,550, Air = 215 LPM, $H_2$ = 70 LPM) formed by a Hencken burner (12.5 mm dia.) with a low-flow methane-air pilot.

Since a 10 μs delay is needed to obtain sufficient tag displacement for a velocity measurement, the 500 single-shot tag lines are averaged for the 10 μs delay to achieve unbroken displacement lines with and without background subtraction as shown Figure 72. With averaging, the displaced lines are unbroken across the 2 cm length of the tag line. The mean displaced line and the original tag line are used to calculate the mean velocity profiles shown in Figure 73. Mean velocity profiles determined from tag images with and without background subtraction show similar values and have a peak velocity of ~39 m/s (~3.5 pixel displacement) at the center of the jet. The increased jaggedness of the profiles away from x = 0 is a result of the write laser beam expansion which creates a reduced OH (v" = 1) photofragment concentration due to the intensity squared dependence of the two-photon dissociation processes. The SNR of the mean raw image ranges from 4:1 to 7:1 in the region where velocity profiles are provided.

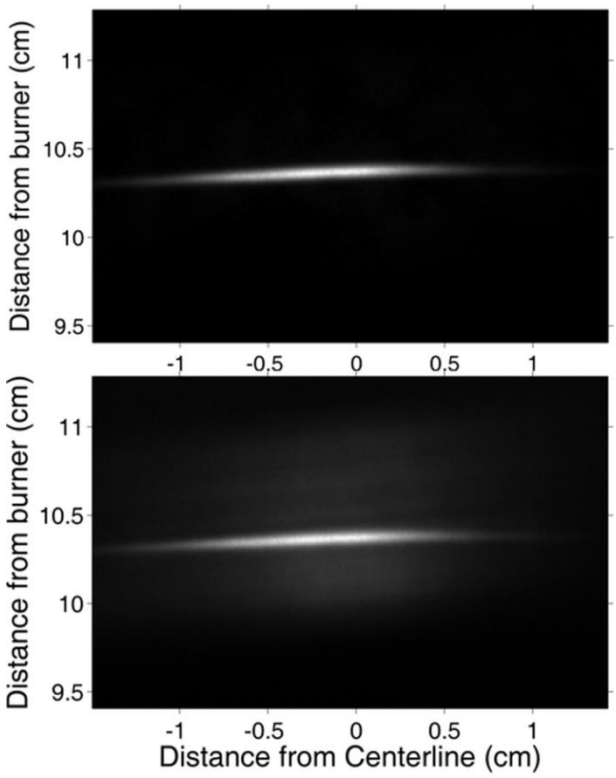


Figure 72: Comparison of mean VE-HTV images (500 single-shots, 10 µs delay) both without (top) and with (bottom) background subtraction with in a lean (φ = 0.78) $H_2$/air turbulent premixed flame (Re = 26,550, Air = 215 LPM, $H_2$ = 70 LPM) formed by a Hencken burner (12.5 mm dia.) with a low-flow methane-air pilot.

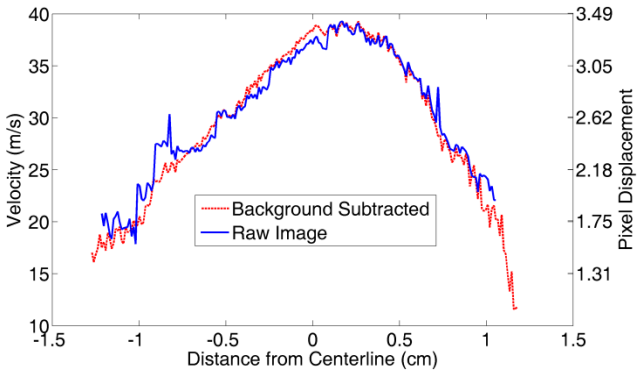


Figure 73: Comparison of VE-HTV velocity measurements at x/D = 10.4 in a lean (φ = 0.78) $H_2$/air turbulent premixed flame (Re = 26,550, Air = 215 LPM, $H_2$ = 70 LPM,) formed by a Hencken burner (12.5 mm dia.) with a low-flow methane-air pilot. Mean velocity (500 single-shots, 10 µs delay) is calculated from the Figure 72 images that are with and without background subtraction.

These results in the turbulent premixed jet flame and the single-shot tag images in laminar flames (Figure 65) show that the VE-HTV has potential for single-shot measurements of velocity in turbulent high temperature flames. VE-HTV is advantageous over conventional HTV in reducing the background OH level in the MTV measurements at high temperature flame conditions. Since is VE-HTV is non-linear, it has the potential to write very small diameter tag lines as has been done with other non-linear methods [103]. The main disadvantage of a non-linear technique is that it is more difficult to write multi-line MTV grids to obtain two components of velocity in the imaging plane [78, 107].

**Conclusions and potential improvements**

A new molecular tagging velocimetry technique called Vibrationally Excited Hydroxyl Tagging Velocimetry (VE-HTV) is demonstrated in an $H_2$-air flame at lean, stoichiometric and rich laminar flames. A KrF excimer laser is used to photo-dissociate water via a two-photon process to create vibrationally excited OH (v=1); the vibrationally excited molecular tracer can be distinguished from background OH concentrations in high temperature combustion gases. The high vibrational frequency of OH ($\gamma_{vib}$ = 3700 $cm^{-1}$) allows the OH (v=1) tag to be seen in high temperature flames at 2300 K. Due to chemical reactions of OH with $H_2$, the tag half-life was shorter for rich flames (~2 μs half-life at $\phi$ = 2.36). Still, the tag half-life exceeds 6 μs for $\phi \leq 1.23$. While the lifetime of the vibrationally excited OH (v=1) tag is shorter than the ground state OH (v=0) tag, it still has sufficient lifetime for fast flows. In laminar $H_2$/air flames, single-shot line OH (v=1) tag images could be clearly seen for time delays up to 10 μs sufficient for single-shot measurement of high-speed combustion flows [78, 107].

In a lean $H_2$/air ($\phi$ = 0.78, Re = 26,500) turbulent premixed flame with an annular co-flow pilot, mean velocity measurements are obtained at a time delay of 10 µs. A mean peak velocity of 39 m/s is obtained from an average of 500 single-shot images both with and without background subtraction. The good agreement between the two mean velocity profiles demonstrates the technique's ability to successfully write tags in regions of high backgrounds.

The results of the laminar and turbulent flame studies show that single-shot velocity VE-HTV measurements are possible in turbulent flames. The VE-HTV method is best suited for high-speed flames with a high background of OH that requires the use of a vibrationally excited OH tag.

As seen in the bottom image of Figure 65, no vibrationally excited tags were seen outside of the flame zone (i.e., near room air conditions) in part due to higher levels of vibrational relaxation thus preventing the use of this technique in room air. However, while the OH (v = 1) concentration is insufficient, the OH (v = 0) created by the relaxation are still present and can be used for tagging. Therefore, by adding a second read laser/camera system to fluoresce the ground state OH in addition to the vibrationally excited tracers, the method could be enhanced to work in all conditions.

# CHAPTER 5: SUMMARY

The study of turbulent flames is of immediate interest to propulsion devices due to their faster burning rates and naturally high Reynold's numbers at flight conditions. The proposed work will explore: 1) a phenomenological study of premixed, freely propagating flame kernels , 2) diffusion flames in a model scramjet combustor using UV Raman scattering, and 3) the development of a new molecular tagging velocimetry technique

1. A novel wind tunnel facility has been made to study premixed $CH_4$-air flames, turbulent flame kernel propagation in high speed mean flows up to the incompressible limit ($M \leq 0.3$). In this tunnel, a flame kernel is laser ignited and allowed to freely convect downstream free of any wakes or shear layers. Since there are no geometric dependencies of this flame (due to burner, stabilization device, or spark plugs), the kernel has no artificial "memory" effects allowing for a pure, phenomenological study of premixed flame propagation. Using this tunnel, PLIF measurements were used to acquire images of the kernels at various times (and/or distances from the igniters) to determine a statistical representation of flame speed. The measured flame speeds were compared with classical flame bomb correlations to determine if there was any effect of mean flow velocity for nominally incompressible flows. In general, the freely propagating flame kernels followed similar trends found in flame bomb data, and discrepancies between the data were most likely due to a lack of radial mean flow in the present experiment, and laser ignition artifacts. The current lean ($\phi = 0.7$, $M = 0.2$ and 0.3) data taken in a small duct (50 x 50 $mm^2$) correlated well with low speed data ($\phi = 0.71$, $M < 0.2$) taken in a modified version of the tunnel with the nozzle removed (150 x 150 $mm^2$) demonstrating that current apparatus can be used to study premixed turbulent flame kernels without the radial mean flow or low repetition rates of flame bombs

2. UV Raman scattering measurements of temperature and major species were taken over a ramp close-out cavity in the Mach 2 scramjet test section of Research Cell 19 at Wright Patterson Air Force Base. The cavity was directly fueled from the ramp using 70% $CH_4$ 30% $H_2$ fuel. Experimental results showed that $CH_4$ was largely unreacted by the time it reached the leading edge of the cavity forming a fuel rich region along the floor and behind the step. This region of unreacting $CH_4$ may have resulted in production of polycyclic aromatic hydrocarbons (PAH), thus creating the laser induced broadband interference observed in this region. The path of the injected fuel was traced out through the cavity using scatter plots, and $CH_4$ was mainly unreacted at near the injectors and behind the step, partially reacted by the midpoint of the cavity below the shear layer, and reacted near the ramp where the products will either exit the cavity or recirculate. Comparisons between CO and $CO_2$ profiles showed that CO began to oxidize by the midpoint of the cavity below the shear layer and was nearly gone by the ramp although there was still scatter in the $CO_2$ data. Injected $H_2$ quickly burned off near the injectors; however, $H_2$ concentrations were observed where CO began to oxidize probably from water shift reactions. Data taken in the shear layer demonstrated diffusion across the shear layer of $O_2$ into the cavity, and hot products into the main flow of tunnel. Temperature, $O_2$, and $H_2O$ RMS fluctuations were fairly constant throughout the cavity primarily due to the slow reaction of $CH_4$ and to a combination of recirculation of hot products and diffusion of $O_2$ across the shear layer.
3. A new molecular tagging velocimetry technique called Vibrationally Excited Hydroxyl Tagging Velocimetry (VE-HTV) is demonstrated in an $H_2$-air flame at lean, stoichiometric and rich laminar flames. A KrF excimer laser is used to photo-dissociate water via a two-photon process to create vibrationally excited OH (v=1); the vibrationally excited molecular tracer can be distinguished from background OH concentrations in high temperature

combustion gases. The high vibrational frequency of OH ($\gamma_{vib}$ = 3700 $cm^{-1}$) allows the OH (v=1) tag to be seen in high temperature flames at 2300 K. Due to chemical reactions of OH with $H_2$, the tag half-life was shorter for rich flames (~2 μs half-life at φ = 2.36). Still, the tag half-life exceeds 6 μs for φ ≤ 1.23. While the lifetime of the vibrationally excited OH (v=1) tag is shorter than the ground state OH (v=0) tag, it still has sufficient lifetime for fast flows. In laminar $H_2$/air flames, single-shot line OH (v=1) tag images could be clearly seen for time delays up to 10 μs sufficient for single-shot measurement of high-speed combustion flows [78, 107]. In a lean $H_2$/air (φ = 0.78, Re = 26,500) turbulent premixed flame with an annular co-flow pilot, mean velocity measurements are obtained at a time delay of 10 μs. A mean peak velocity of 39 m/s is obtained from an average of 500 single-shot images both with and without background subtraction. The good agreement between the two mean velocity profiles demonstrates the technique's ability to successfully write tags in regions of high backgrounds. The results of the laminar and turbulent flame studies show that single-shot velocity VE-HTV measurements are possible in turbulent flames. The VE-HTV method is best suited for high-speed flames with a high background of OH that requires the use of a vibrationally excited OH tag.

# Appendix A

## PRELIMINARY PREMIXED FLAME KERNEL MEASUREMENTS AND SYSTEMS

**Introduction**

Preliminary premixed kernel measurements were conducted to access two issues: 1) the ability to repeatably ignite kernels in high speed turbulent flows, and 2) actively generate turbulence. This appendix will detail two experiments conducted with pre-nozzle passive grid generated turbulence, and active blown grid generated turbulence.

While these experiments demonstrated the ability to ignite flame kernels over a wide range of turbulence intensities and actively generate turbulence, the turbulent lengths scales created by the blown grid were much larger than the kernels and rapidly increased as a function of mean flow velocity.

**Turbulence generation**

This section will detail two different methods of generating turbulence. The first method used passive grids as described by previous authors [117-120]. Schematic of the grid-generation scheme is shown in Figure A1 (left) with an example grid. The second generation of turbulence was from a "uniform jet grid" [121, 122] (see Figure A1 right). In this method, a grid of pressurized, perforated tubes is placed in the same location as the passive grid mentioned previously. Turbulent jets are formed at each perforation thus increasing the turbulence level, and any inhomogeneities can be corrected by varying the relative flow rates between the respective tubes. This method provided an increase in turbulence intensities which can be varied for a given Mach number. However, this technique requires that the equivalence ratios be matched between the blown grid and the main stream. Additionally, due to the wide of range of flow rates and blowing ratios of interest, having uniform jets is impossible with a single orifice size requiring multiple different jet arrays for consistency. Both of these generators had the same location as the vane grid (see Figure 6).

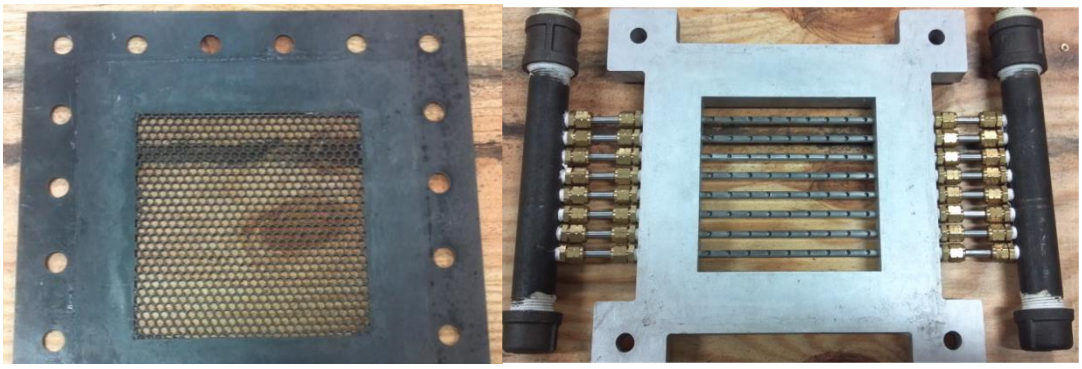

Figure A1: Pictures of passive grid turbulence generator (left) and blown grid (right)

**Pre-nozzle passive grid turbulence**

The first round of tests generated turbulence with a passive grid consisting of a 2.29 mm thick perforated plate with 12.7 mm holes place upstream of the nozzle. The grid featured a plate solidity of 33% (percentage of blocked area) with holes arranged in a hexagonal pattern generating a u'/U of ~1% as shown in Figure A2. A Continuum Surelite Nd:YAG laser (195 mJ/pulse at 1064 nm after focusing lens) was used to ignite the flame kernels. The spark laser was focused into the tunnel using a -250 mm lens to expand the original 6 mm beam to ~25.4 mm before being focused by a 60 mm lens through a window 50 mm upstream of the test section. These lenses were chosen to prevent damage to the window which was 2.5 cm from the focal point and limit the effect of back reflections on the 60 mm lens, and provided a spot size of ~800 µm for the 195 mJ pulse.

Data was taken at 3 streamwise locations (12.7 cm, 16.5 cm, and 20 cm) from the spark laser. Example raw single-shot images for $\phi = 1$ are shown in Figure A3 with the corresponding c-maps shown in Figure A4. The binarized images were corrected for the unevenness of the laser sheet. The flow direction is from left-to-right, and the top of the images is towards the

spark laser. The third lobe found in the images is an artifact of the laser ignition similar to the results of Mansour et al. [20].

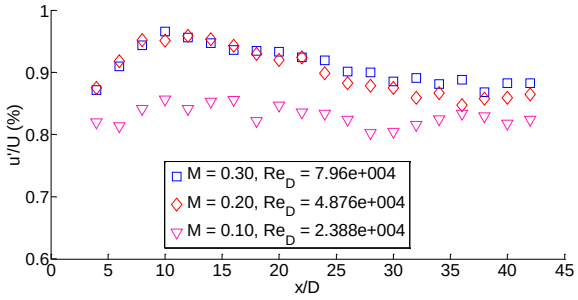


Figure A2: Turbulence intensities as function of mean velocity for pre-nozzle passive grid generation.

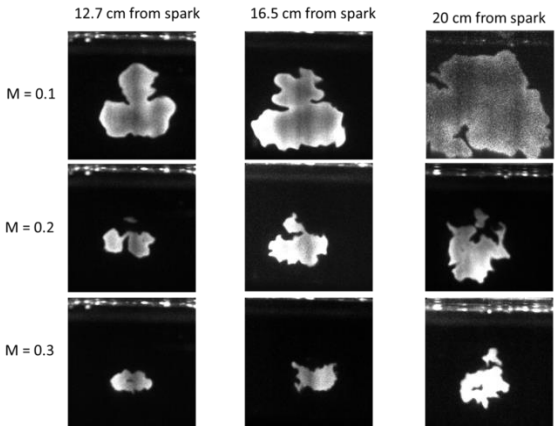


Figure A3: Raw single-shot OH PLIF images from pre-nozzle passive grid studies.

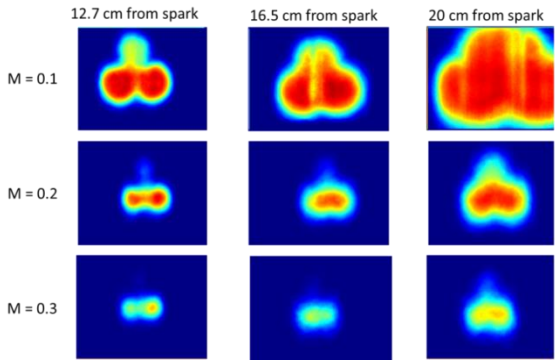


Figure A4: C-maps of flame kernels form pre-nozzle passive grid studies.

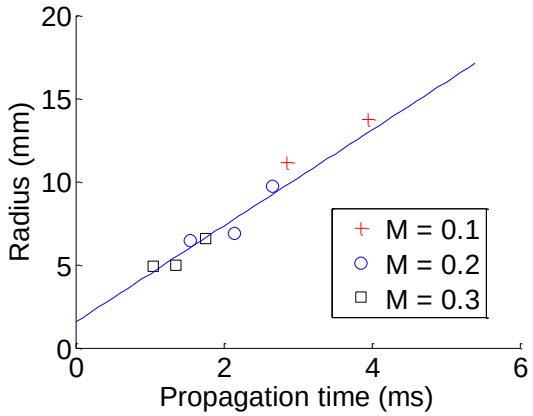


Figure A5: Characteristic radius verse time for $\phi = 1$ for the passive grid.

The mean images are used to calculate an equivalent radius for the kernels, and are plotted versus propagation time in Figure A5. Both the M = 0.2 and M = 0.3 curves are nearly collinear and the two upstream M = 0.1 data points also lie on these lines (the third has made contact with the wall and was excluded).

Flame thickness is determined from Equation 17 using the inverse gradients from the c-maps along the $\bar{c} = 0.5$ contour. Flame thickness is plotted vs time for all Mach numbers shown in Figure A6. Normalized flame thicknesses are also shown in the figure using a laminar flame thickness of 0.6 mm approximated using $S_L = 40$ cm/s and $\alpha_{mix,\ 1200K} = 2.38\ cm^2/s$. The flame brush thicknesses for the higher turbulence case (i.e. M = 0.3 since u' $\alpha$ $U_{mean}$) appears to be growing faster than at lower turbulence.

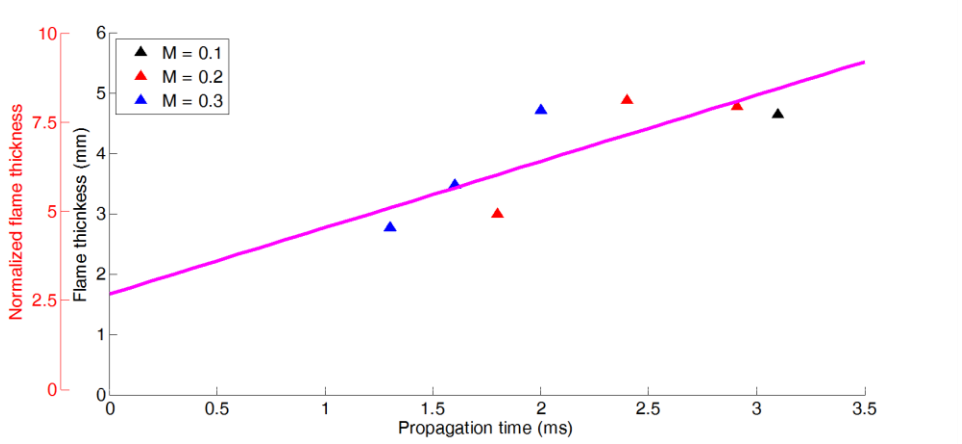


Figure A6: Flame brush thickness and normalized flame thickness for $\phi = 1$ verse time with trend lines for the passive grid.

While the pre-nozzle passive grid studies demonstrated the ability to ignite mixtures under low turbulence for a variety of mean flow rates and an increase in flame brush thickness as a function of turbulence, the laser ignition artifacts limited the interpretation of the results. The three lobe structure reduced the effective propagation time before the kernels interacted with the walls. Additionally, it is unknown if this lobed structure had any effect on flame propagation.

**Blown grid turbulence**

To increase the turbulence intensity and remove laser ignition artifacts found in the pre-nozzle passive grid studies, a second round of experiments was conducted with the following improvements: 1) new spark system, and 2) new turbulence generator. To eliminate the previous lobed kernel structure, a 35 mm aspheric lens replace the previous optics and a second harmonic crystal was added to existing spark laser to double the 1064 nm laser to 532 nm laser. These two changes allowed for 7.5 mJ/pulse spark energy used across all of the cases studied. The new turbulence generator was the blown grid system (Figure A1 right).

The u' values stated in the second set of tests are given for the fluctuations in the streamwise direction. Due to vortex stretching the nozzle, the turbulence is highly anisotropic with the fluctuations in the streamwise direction being suppressed while the other two components are significantly higher. Additionally, the degree of anisotropy is a strong function of the Mach number with higher mean flow rates creating more anisotropy as shown in Figure A7. Due to these large scales, there was significant out-of-plane motion of the kernels. Therefore, an orthogonal camera was used to monitor both the OH* chemiluminescence of the kernels relative to the OH PLIF sheet as shown in Figure A8. The revised data processing using this new camera is shown schematically in Figure A9. Using this additional camera, only flame kernels which are centered on the PLIF sheet were used in the statistics of flame growth/speed.

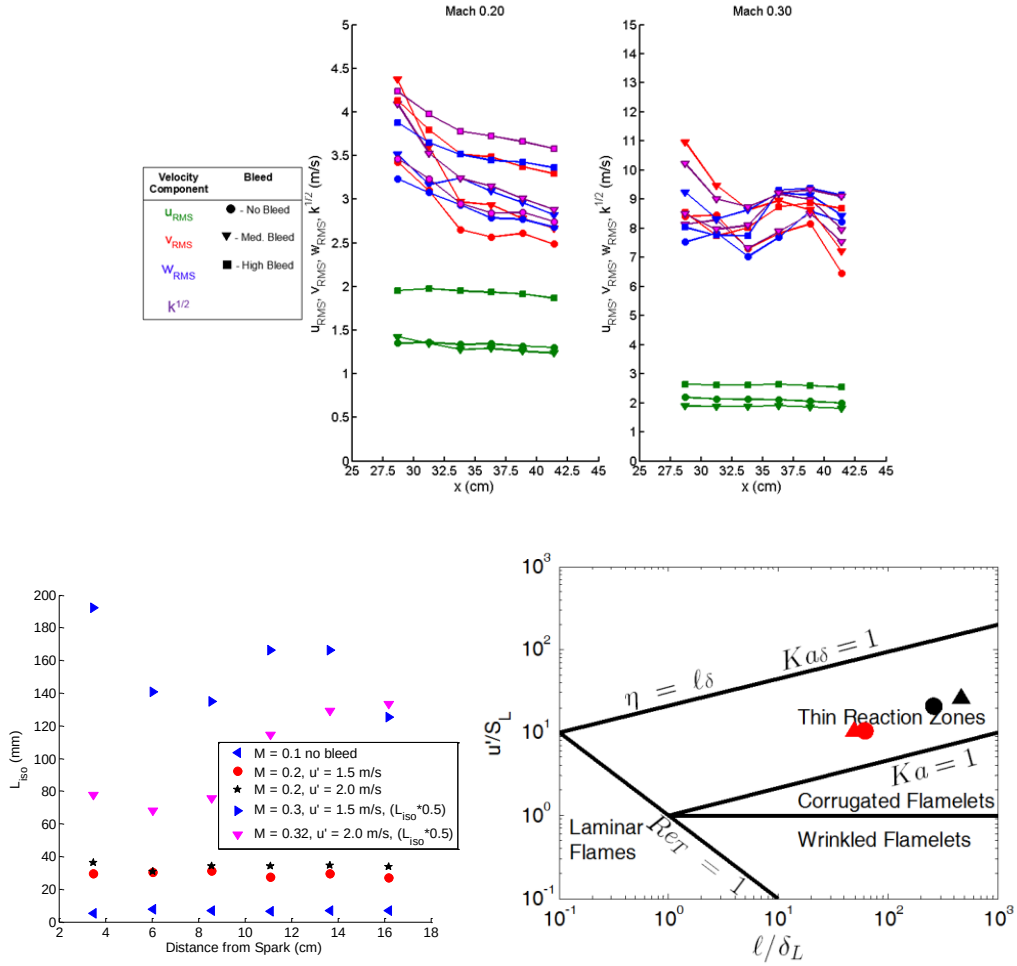


FigureA7: Hot wire anemometry data showing the correlation between Mach number and anisotropy for the blown grid turbulence generator on both intensity (top), length scale (bottom left), and regime diagram locations (bottom right).

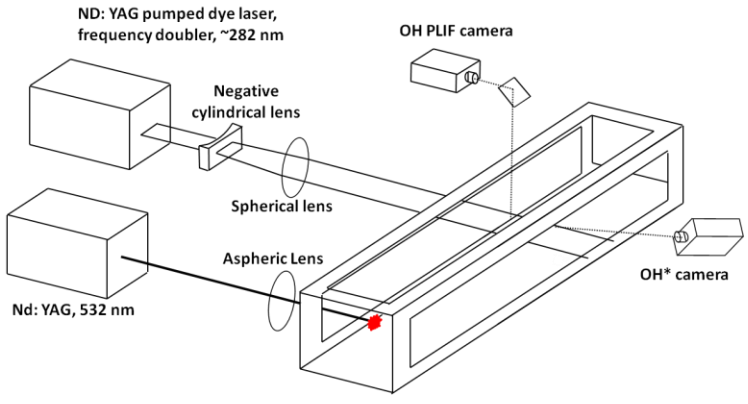


Figure A8: Experimental configuration with OH* included

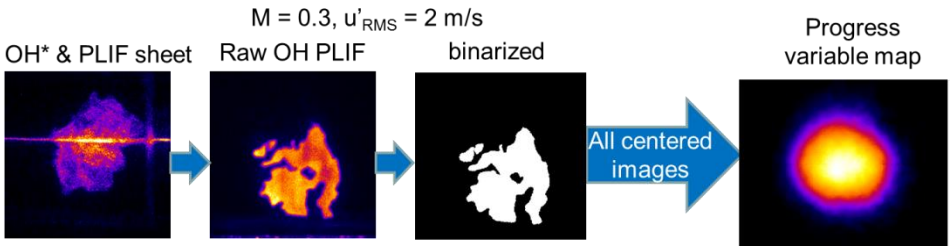


Figure A9: Data processing including the PLIF sheet/OH* conditioning

Since there is higher turbulence in the transverse directions at higher M, then there should be changes in R(t) as a function of M. The effects of this anisotropy can be seen in Figure A10 where c-map of the kernels starts in ellipse with the major axis in the streamwise direction and with time becomes an ellipse in the transverse direction. The original ellipse shape is most likely an artifact of the laser ignition as explained previously which overtime becomes spherical then an ellipse in the transverse direction due to the higher turbulence fluctuations in that direction. Eventually, the expansion wave reaches the wall and flame propagation is inhibited in the transverse directions.

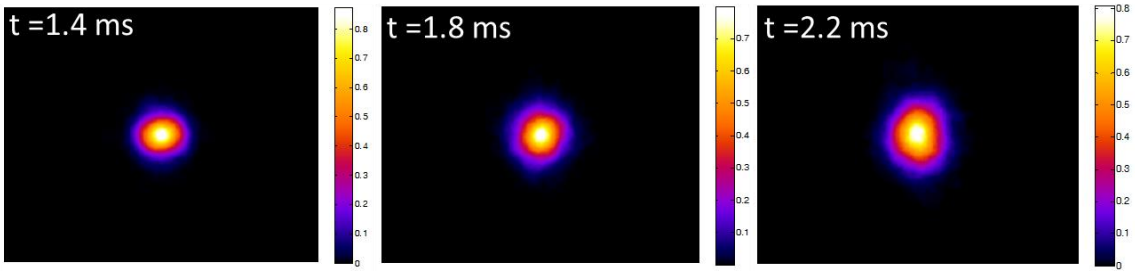


Figure A10: C-maps for M = 0.5 and u' = 2 m/s for the blown grid generator with 7.5 mJ/pulse ignition.

For the second series of tests mean Mach number range was increased up to M = 0.6. While the overall turbulence intensity increases as a function of mean flow velocity, the length

scales also increase. Due to limitations of the current hot wire system, turbulence could not be measured above M = 0.3. However, it can be seen that ℓ becomes very large and therefore $u'_{eff}$ becomes very small for the size of kernels studied (see Table 1). Therefore, there are no significant changes with respect to Mach number/u' observed as shown in Figure A11.

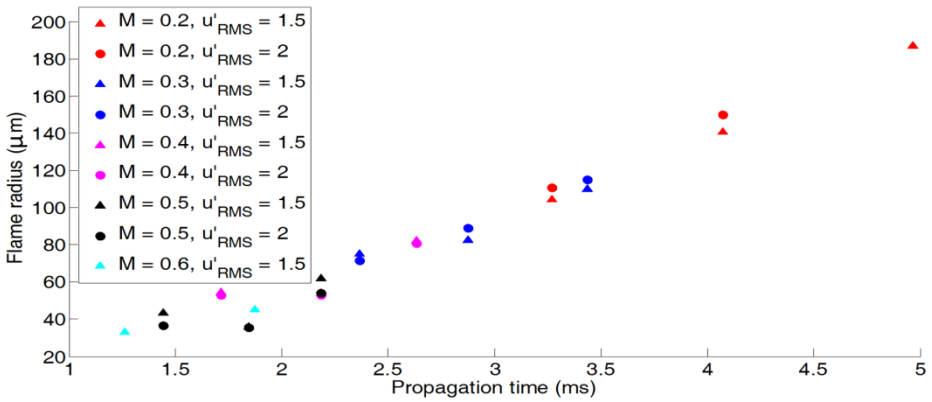


Figure A11: Flame radius verse time for blown grid studies.

Analysis of flame surface density was conducted and peak values were observed to decrease with time as shown in Figure A12. Finally, instantaneous curvature statistics are shown in Figure A13. For the low turbulence intensities, there is no overall curvature preference, but for higher turbulence intensities positive curvature values are more likely to occur since the mixture Ma = 1.3 for $\phi = 1$ [42]. However, mean curvature decreases downstream as the kernel radii become larger and turbulence intensities decrease.

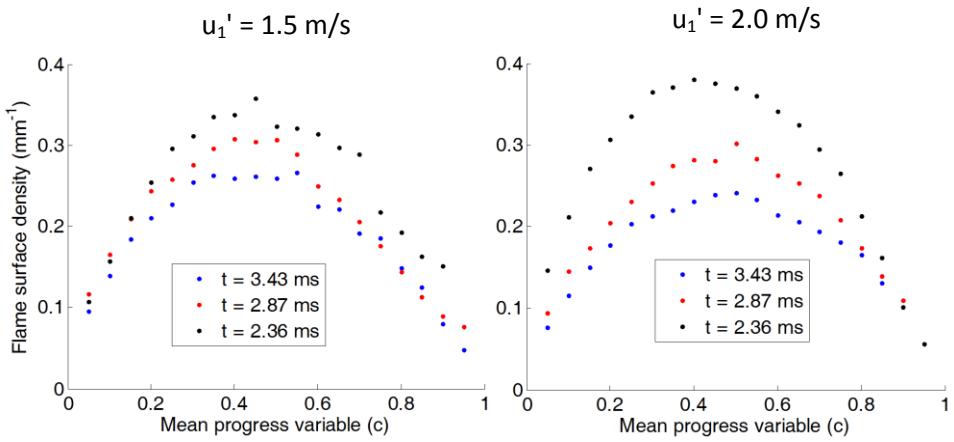


Figure A12: Flame surface density for M = 0.3 at $u_1'$ = 1.5 m/s (left) and 2 m/s (right) for the blown grid

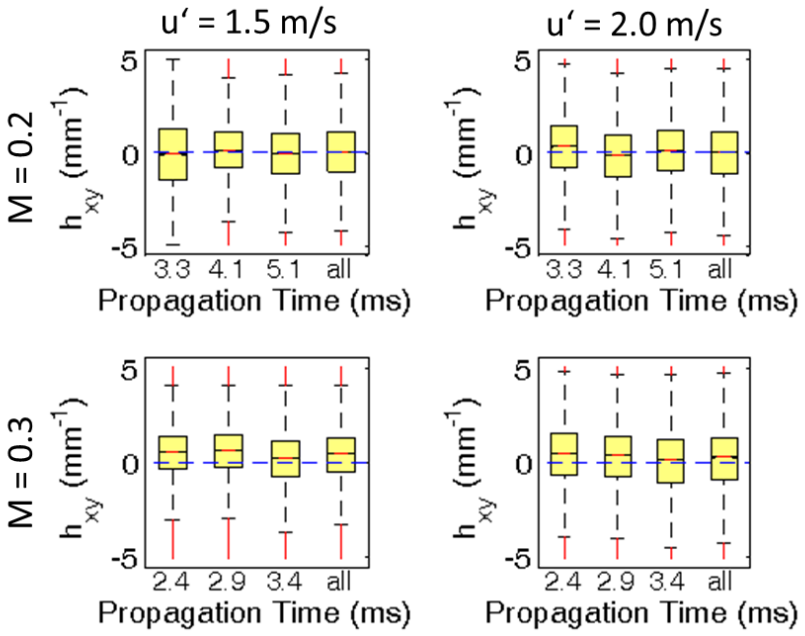


Figure A13: Standard box plot representation of instantaneous curvature values for the blown grid kernels.

## REFERENCES


[1] Driscoll, J. F., 2008, "Turbulent premixed combustion: Flamelet structure and its effect on turbulent burning velocities," Progress in Energy and Combustion Science, 34(1), pp. 91-134.
[2] Bonhomme, A., Selle, L., and Poinsot, T., 2013, "Curvature and confinement effects for flame speed measurements in laminar spherical and cylindrical flames," Combustion and Flame, 160(7), pp. 1208-1214.
[3] Burke, M. P., Chen, Z., Ju, Y., and Dryer, F. L., 2009, "Effect of cylindrical confinement on the determination of laminar flame speeds using outwardly propagating flames," Combustion and Flame, 156(4), pp. 771-779.
[4] Abdel-Gayed, R. G., Bradley, D., and Lawes, M., 1987, "Turbulent burning velocities - a general correlation in terms of straining rates," Proceedings of the Royal Society of London Series A-Mathematical Physical and Engineering Sciences, 414(1847), pp. 389-413.
[5] Chaudhuri, S., Wu, F., Zhu, D., and Law, C. K., 2012, "Flame Speed and Self-Similar Propagation of Expanding Turbulent Premixed Flames," Physical Review Letters, 108(4).
[6] Chaudhuri, S., Wu, F. J., and Law, C. K., 2013, "Scaling of turbulent flame speed for expanding flames with Markstein diffusion considerations," Physical Review E, 88(3).
[7] Chaudhuri, S., Saha, A., and Law, C. K., 2015, "On flame-turbulence interaction in constant-pressure expanding flames," Proceedings of the Combustion Institute, 35, pp. 1331-1339.
[8] Bradley, D., Haq, M. Z., Hicks, R. A., Kitagawa, T., Lawes, M., Sheppard, C. G. W., and Woolley, R., 2003, "Turbulent burning velocity, burned gas distribution, and associated flame surface definition," Combustion and Flame, 133(4), pp. 415-430.
[9] Bradley, D., Lawes, M., and Mansour, M. S., 2009, "Flame surface densities during spherical turbulent flame explosions," Proceedings of the Combustion Institute, 32, pp. 1587-1593.
[10] Bradley, D., Lawes, M., and Mansour, M. S., 2011, "Correlation of turbulent burning velocities of ethanol-air, measured in a fan-stirred bomb up to 1.2 MPa," Combustion and Flame, 158(1), pp. 123-138.
[11] Bradley, D., Lawes, M., and Mansour, M. S., 2011, "Measurement of turbulent burning velocities in implosions at high pressures," Proceedings of the Combustion Institute, 33, pp. 1269-1275.
[12] Fairweather, M., Ormsby, M. P., Sheppard, C. G. W., and Woolley, R., 2009, "Turbulent burning rates of methane and methane-hydrogen mixtures," Combustion and Flame, 156(4), pp. 780-790.
[13] Kelley, A. P., and Law, C. K., 2009, "Nonlinear effects in the extraction of laminar flame speeds from expanding spherical flames," Combustion and Flame, 156(9), pp. 1844-1851.
[14] Kelley, A. P., Jomaas, G., and Law, C. K., 2009, "Critical radius for sustained propagation of spark-ignited spherical flames," Combustion and Flame, 156(5), pp. 1006-1013.
[15] Shy, S. S., Shih, W. T., and Liu, C. C., 2008, "More on minimum ignition energy transition for lean premixed turbulent methane combustion in flamelet and distributed regimes," Combustion Science and Technology, 180(10-11), pp. 1735-1747.
[16] Shy, S. S., Liu, C. C., and Shih, W. T., 2010, "Ignition transition in turbulent premixed combustion," Combustion and Flame, 157(2), pp. 341-350.
[17] Kelley, A. P., 2011, "Dynamics of expanding flames," Ph.D. dissertation, Princeton University.
[18] Khokhlov, A. M., Oran, E. S., and Thomas, G. O., 1999, "Numerical simulation of deflagration-to-detonation transition: The role of shock-flame interactions in turbulent flames," Combustion and Flame, 117(1-2), pp. 323-339.

[19] Thomas, G., Bambrey, R., and Brown, C., 2001, "Experimental observations of flame acceleration and transition to detonation following shock-flame interaction," Combustion Theory and Modelling, 5(4), pp. 573-594.
[20] Mansour, M., Peters, N., and Schrader, L.-U., 2008, "Experimental study of turbulent flame kernel propagation," Experimental Thermal and Fluid Science, 32(7), pp. 1396-1404.
[21] Cardin, C., Renou, B., Cabot, G., and Boukhalfa, A. M., 2013, "Experimental analysis of laser-induced spark ignition of lean turbulent premixed flames: New insight into ignition transition," Combustion and Flame, 160(8), pp. 1414-1427.
[22] Trunk, P. J., Boxx, I., Heeger, C., Meier, W., Boehm, B., and Dreizler, A., 2013, "Premixed flame propagation in turbulent flow by means of stereoscopic PIV and dual-plane OH-PLIF at sustained kHz repetition rates," Proceedings of the Combustion Institute, 34, pp. 3565-3572.
[23] Renou, B., Mura, A., Samson, E., and Boukhalfa, A., 2002, "Characterization of the local flame structure and the flame surface density for freely propagating premixed flames at various Lewis numbers," Combustion Science and Technology, 174(4), pp. 143-179.
[24] Renou, B., and Boukhalfa, A., 2001, "An experimental study of freely propagating premixed flames at various Lewis numbers," Combustion Science and Technology, 162, pp. 347-370.
[25] Pitsch, H., Desjardins, O., Balarac, G., and Ihme, M., 2008, "Large-eddy simulation of turbulent reacting flows," Progress in Aerospace Sciences, 44(6), pp. 466-478.
[26] Sheikhi, M. R. H., Drozda, T. G., Givi, P., Jaberi, F. A., and Pope, S. B., 2005, "Large eddy simulation of a turbulent nonpremixed piloted methane jet flame (Sandia Flame D)," Proceedings of the Combustion Institute, 30, pp. 549-556.
[27] Genin, F., and Menon, S., 2010, "Simulation of turbulent mixing behind a strut injector in supersonic flow," AIAA Journal, 48(3), pp. 526-539.
[28] Sung, C. J., Kistler, J. S., Nishioka, M., and Law, C. K., 1996, "Further studies on effects of thermophoresis on seeding particles in LDV measurements of strained flames," Combustion and Flame, 105(1-2), pp. 189-201.
[29] Koike, S., Takahashi, H., Tanaka, K., Hirota, M., Takita, K., and Masuya, G., 2007, "Correction method for particle velocimetry data based on the Stokes drag law," AIAA Journal, 45(11), pp. 2770-2777.
[30] Reeder, M. F., Crafton, J. W., Estevadeordal, J., DeLapp, J., McNiel, C., Peltier, D., and Reynolds, T., 2010, "Clean seeding for flow visualization and velocimetry measurements," Experiments in Fluids, 48(5), pp. 889-900.
[31] Santoro, R. J., Pal, S., Woodward, R. D., and Schaaf, L., "Rocket testing at university facilities," 39th AIAA Aerospace Sciences Meeting,Reno, Nevada, January 8-11, 2001AIAA Paper 2001-0748.
[32] Vedula, R., Mittal, M., and Schock, H. J., 2013, "Molecular tagging velocimetry and its application to in-cylinder flow measurements," Journal of Fluids Engineering-Transactions of the ASME, 135(12), pp. 1-17.
[33] Wehrmeyer, J. A., Ribarov, L. A., Oguss, D. A., and Pitz, R. W., 1999, "Flame flow tagging velocimetry with 193-nm $H_2O$ photodissociation," Applied Optics, 38(33), pp. 6912-6917.
[34] Borghi, R., 1985, On the structure and morphology of turbulent premixed flames, Springer US, Plenum, N.Y.
[35] Peters, N., 1999, "The turbulent burning velocity for large-scale and small-scale turbulence," Journal of Fluid Mechanics, 384, pp. 107-132.
[36] Lipatnikov, A. N., and Chomiak, J., 2002, "Turbulent flame speed and thickness: phenomenology, evaluation, and application in multi-dimensional simulations," Progress in Energy and Combustion Science, 28(1), pp. 1-74.

[37] Hamlington, P. E., Poludnenko, A. Y., and Oran, E. S., 2011, "Interactions between turbulence and flames in premixed reacting flows," Physics of Fluids, 23(12).
[38] Poludnenko, A. Y., and Oran, E. S., 2011, "The interaction of high-speed turbulence with flames: Turbulent flame speed," Combustion and Flame, 158(2), pp. 301-326.
[39] Savre, J., Carlsson, H., and Bai, X. S., 2013, "Turbulent methane/air premixed flame structure at high Karlovitz numbers," Flow Turbulence and Combustion, 90(2), pp. 325-341.
[40] Markstein, G. H., 1951, "Experimental and theoretical studies of flame-front stability," Journal of the Aeronautical Sciences, 18(3), pp. 199-209.
[41] Halter, F., Tahtouh, T., and Mounaim-Rousselle, C., 2010, "Nonlinear effects of stretch on the flame front propagation," Combustion and Flame, 157(10), pp. 1825-1832.
[42] Aung, K. T., Tseng, L. K., Ismail, M. A., and Faeth, G. M., 1995, "Laminar burning velocities and Markstein numbers of hydrocarbon and air flames - response," Combustion and Flame, 102(4), pp. 526-530.
[43] Bradley, D., 1992, "How fast can we burn?," Proceedings of the Combustion Institute, 24, pp. 247-253.
[44] Liberman, M. A., Ivanov, M. F., Peil, O. E., Valiev, D. M., and Eriksson, L. E., 2004, "Self-acceleration and fractal structure of outward freely propagating flames," Physics of Fluids, 16(7), pp. 2476-2482.
[45] Kang, H. S., Chester, S., and Meneveau, C., 2003, "Decaying turbulence in an active-grid-generated flow and comparisons with large-eddy simulation," Journal of Fluid Mechanics, 480, pp. 129-160.
[46] Larssen, J. V., and Devenport, W. J., 2011, "On the generation of large-scale homogeneous turbulence," Experiments in Fluids, 50(5), pp. 1207-1223.
[47] Makita, H., 1991, "Realization of large-scale turbulence field in a small wind-tunnel," Fluid Dynamics Research, 8(1-4), pp. 53-64.
[48] Mydlarski, L., and Warhaft, Z., 1996, "On the onset of high-Reynolds-number grid-generated wind tunnel turbulence," Journal of Fluid Mechanics, 320, pp. 331-368.
[49] Mydlarski, L., and Warhaft, Z., 1998, "Passive scalar statistics in high-Peclet-number grid turbulence," Journal of Fluid Mechanics, 358, pp. 135-175.
[50] Han, Y., George, W., and Hjarne, J., 2005, "Effect of a contraction on turbulence. Part 1: Experiment," 43rd Aerospace Sciences Meeting,Reno, Nevada, January 10-14, 2005, AIAA-2005-119.
[51] Liu, R., Ting, D. S. K., and Checkel, M. D., 2007, "Constant Reynolds number turbulence downstream of an orificed perforated plate," Experimental Thermal and Fluid Science, 31(8), pp. 897-908.
[52] Slais, T. A., 15 November 2014, "*Personal communication*."
[53] Dunn, M. J., Masri, A. R., Bilger, R. W., and Barlow, R. S., 2010, "Finite rate chemistry effects in highly sheared turbulent premixed flames," Flow Turbulence and Combustion, 85(3-4), pp. 621-648.
[54] Mansour, M. S., Chen, Y. C., and Peters, N., 1999, "Highly strained turbulent rich methane flames stabilized by hot combustion products," Combustion and Flame, 116(1-2), pp. 136-153.
[55] Yuen, F. T. C., and Guelder, O. L., 2009, "Premixed turbulent flame front structure investigation by Rayleigh scattering in the thin reaction zone regime," Proceedings of the Combustion Institute, 32, pp. 1747-1754.
[56] Shepherd, I. G., and Cheng, R. K., 2001, "The burning rate of premixed flames in moderate and intense turbulence," Combustion and Flame, 127(3), pp. 2066-2075.

[57] Filatyev, S. A., Driscoll, J. F., Carter, C. D., and Donbar, J. M., 2005, "Measured properties of turbulent premixed flames for model assessment, including burning velocities, stretch rates, and surface densities," Combustion and Flame, 141(1-2), pp. 1-21.
[58] Sweeney, M. S., Hochgreb, S., and Barlow, R. S., 2011, "The structure of premixed and stratified low turbulence flames," Combustion and Flame, 158(5), pp. 935-948.
[59] Cheng, R. K., Shepherd, I. G., Bedat, B., and Talbot, L., 2002, "Premixed turbulent flame structures in moderate and intense isotropic turbulence," Combustion Science and Technology, 174(1), pp. 29-59.
[60] Lawn, C. J., and Schefer, R. W., 2006, "Scaling of premixed turbulent flames in the corrugated regime," Combustion and Flame, 146(1-2), pp. 180-199.
[61] Sweeney, M., and Hochgreb, S., 2009, "Autonomous extraction of optimal flame fronts in OH planar laser-induced fluorescence images," Applied Optics, 48(19), pp. 3866-3877.
[62] Fries, D., 20 May 2015, "*Personal communication*."
[63] Chaudhuri, S., Akkerman, V., and Law, C. K., 2011, "Spectral formulation of turbulent flame speed with consideration of hydrodynamic instability," Physical Review E, 84(2).
[64] Khokhlov, A. M., Oran, E. S., Chtchelkanova, A. Y., and Wheeler, J. C., 1999, "Interaction of a shock with a sinusoidally perturbed flame," Combustion and Flame, 117(1-2), pp. 99-116.
[65] O'Byrne, S., Danehy, P. M., Tedder, S. A., and Cutler, A. D., 2007, "Dual-pump coherent anti-Stokes Raman scattering measurements in a supersonic combustor," AIAA Journal, 45(4), pp. 922-933.
[66] Hancock, R. D., Schauer, F. R., Lucht, R. P., and Farrow, R. L., 1997, "Dual-pump coherent anti-Stokes Raman scattering measurements of nitrogen and oxygen in a laminar jet diffusion flame," Applied Optics, 36(15), pp. 3217-3226.
[67] Lucht, R. P., Velur-Natarajan, V., Carter, C. D., Grinstead, K. D., Gord, J. R., Danehy, P. M., Fiechtner, G. J., and Farrow, R. L., 2003, "Dual-pump coherent anti-Stokes Raman scattering temperature and $CO_2$ concentration measurements," AIAA Journal, 41(4), pp. 679-686.
[68] Tedder, S. A., Wheeler, J. L., Cutler, A. D., and Danehy, P. M., 2010, "Width-increased dual-pump enhanced coherent anti-Stokes Raman spectroscopy," Applied Optics, 49(8).
[69] Roy, S., Gord, J. R., and Patnaik, A. K., 2010, "Recent advances in coherent anti-Stokes Raman scattering spectroscopy: Fundamental developments and applications in reacting flows," Progress in Energy and Combustion Science, 36(2).
[70] Barlow, R. S., Carter, C. D., and Pitz, R. W., 2002, "Multiscalar Diagnostics in Turbulent Flames," Applied Combustion Diagnostics, K. Kohse-Hoeinghaus, and J. B. Jeffries, eds., Taylor and Francis, New York, pp. 384-407.
[71] Kutne, P., Kapadia, B. K., Meier, W., and Aigner, M., 2011, "Experimental analysis of the combustion behaviour of oxyfuel flames in a gas turbine model combustor," Proceedings of the Combustion Institute, 33, pp. 3383-3390.
[72] Meier, W., Boxx, I., Stohr, M., and Carter, C. D., 2010, "Laser-based investigations in gas turbine model combustors," Experiments in Fluids, 49(4), pp. 865-882.
[73] Stopper, U., Aigner, M., Ax, H., Meier, W., Sadanandan, R., Stohr, M., and Bonaldo, A., 2010, "PIV, 2D-LIF and 1D-Raman measurements of flow field, composition and temperature in premixed gas turbine flames," Experimental Thermal and Fluid Science, 34(3), pp. 396-403.
[74] Cheng, T. S., Wehrmeyer, J. A., Pitz, R. W., Jarrett, O., and Northam, G. B., 1994, "Raman measurement of mixing and finite-rate chemistry in a supersonic hydrogen-air diffusion flame," Combustion and Flame, 99(1), pp. 157-173.
[75] Lin, K. C., Ryan, M., Carter, C., Gruber, M., and Raffoul, C., 2010, "Raman Scattering Measurements of Gaseous Ethylene Jets in Mach 2 Supersonic Crossflow," Journal of Propulsion and Power, 26(3), pp. 503-513.

[76] Gruber, M. R., Carter, C. D., Montes, D. R., Haubelt, L. C., Kings, P. I., and Hsu, K. Y., 2008, "Experimental studies of pylon-aided fuel injection into a supersonic crossflow," Journal of Propulsion and Power, 24(3), pp. 460-470.
[77] Ben-Yakar, A., and Hanson, R. K., 2001, "Cavity flame-holders for ignition and flame stabilization in scramjets: An overview," Journal of Propulsion and Power, 17, pp. 869-877.
[78] Grady, N. R., Pitz, R. W., Carter, C. D., Hsu, K.-Y., Ghodke, C., and Menon, S., 2012, "Supersonic Flow over a Ramped-Wall Cavity Flame Holder with an Upstream Strut," Journal of Propulsion and Power, 28(5), pp. 982-990.
[79] Gruber, M. R., Donbar, J. M., Carter, C. D., and Hsu, K. Y., 2004, "Mixing and combustion studies using cavity-based flameholders in a supersonic flow," Journal of Propulsion and Power, 20(5), pp. 769-778.
[80] Rasmussen, C. C., Driscoll, J. F., Hsu, K. Y., Donbar, J. M., Gruber, M. R., and Carter, C. D., 2005, "Stability limits of cavity-stabilized flames in supersonic flow," Proceedings of the Combustion Institute, 30, pp. 2825-2833.
[81] Wehr, L., Meier, W., Kutne, P., and Hassa, C., 2007, "Single-pulse ID laser Raman scattering applied in a gas turbine model combustor at elevated pressure," Proceedings of the Combustion Institute, 31, pp. 3099-3106.
[82] Pitz, R. W., Brown, T. M., Nandula, S. P., Skaggs, P. A., DeBarber, P. A., Brown, M. S., and Segall, J., 1996, "Unseeded velocity measurement by ozone tagging velocimetry," Optics Letters, 21(10), pp. 755-757.
[83] Pitz, R. W., Lahr, M. D., Douglas, Z. W., Wehrmeyer, J. A., Hu, S., Carter, C. D., Hsu, K. Y., Lum, C., and Koochesfahani, M. M., 2005, "Hydroxyl tagging velocimetry in a supersonic flow over a cavity," Applied Optics, 44(31), pp. 6692-6700.
[84] Stier, B., and Koochesfahani, M. M., 1999, "Molecular Tagging Velocimetry (MTV) measurements in gas phase flows," Experiments in Fluids, 26(4), pp. 297-304.
[85] Danehy, P. M., O'Byrne, S., Houwing, A. F. P., Fox, J. S., and Smith, D. R., 2003, "Flow-tagging velocimetry for hypersonic flows using fluorescence of nitric oxide," AIAA Journal, 41(2), pp. 263-271.
[86] ElBaz, A. M., and Pitz, R. W., 2012, "$N_2O$ molecular tagging velocimetry," Applied Physics B-Lasers and Optics, 106(4), pp. 961-969.
[87] Hsu, A. G., Srinivasan, R., Bowersox, R. D. W., and North, S. W., 2009, "Two-component molecular tagging velocimetry utilizing NO fluorescence lifetime and $NO_2$ photodissociation techniques in an underexpanded jet flowfield," Applied Optics, 48(22), pp. 4414-4423.
[88] Sanchez-Gonzalez, R., Bowersox, R. D. W., and North, S. W., 2014, "Vibrationally excited NO tagging by NO($A^2\Sigma^+$) fluorescence and quenching for simultaneous velocimetry and thermometry in gaseous flows," Optics Letters, 39(9), pp. 2771-2774.
[89] Kruger, S., and Grunefeld, G., 1999, "Stereoscopic flow-tagging velocimetry," Applied Physics B-Lasers and Optics, 69(5-6), pp. 509-512.
[90] Barker, P., Thomas, A., RubinszteinDunlop, H., and Ljungberg, P., 1995, "Velocity measurements by flow tagging employing laser enhanced ionisation and laser induced fluorescence," Spectrochimica Acta Part B-Atomic Spectroscopy, 50(11), pp. 1301-1310.
[91] Rubinsztein-Dunlop, H., Littleton, B., Barker, P., Ljungberg, P., and Malmsten, Y., 2001, "Ionic strontium fluorescence as a method for flow tagging velocimetry," Experiments in Fluids, 30(1), pp. 36-42.
[92] Lempert, W. R., Jiang, N., Sethuram, S., and Samimy, M., 2002, "Molecular tagging velocimetry measurements in supersonic microjets," AIAA Journal, 40(6), pp. 1065-1070.
[93] Pitz, R. W., Wehrmeyer, J. A., Ribarov, L. A., Oguss, D. A., Batliwala, F., DeBarber, P. A., Deusch, S., and Dimotakis, P. E., 2000, "Unseeded molecular flow tagging in cold and hot flows

using ozone and hydroxyl tagging velocimetry," Measurement Science & Technology, 11(9), pp. 1259-1271.
[94] Ribarov, L. A., Wehrmeyer, J. A., Pitz, R. W., and Yetter, R. A., 2002, "Hydroxyl tagging velocimetry (HTV) in experimental air flows," Applied Physics B-Lasers and Optics, 74(2), pp. 175-183.
[95] Ribarov, L. A., Wehrmeyer, J. A., Hu, S., and Pitz, R. W., 2004, "Multiline hydroxyl tagging velocimetry measurements in reacting and nonreacting experimental flows," Experiments in Fluids, 37(1), pp. 65-74.
[96] Ribarov, L. A., Hu, S. T., Wehrmeyer, J. A., and Pitz, R. W., 2005, "Hydroxyl tagging velocimetry method optimization: signal intensity and spectroscopy," Applied Optics, 44(31), pp. 6616-6626.
[97] Dam, N., Klein-Douwel, R. J. H., Sijtsema, N. M., and ter Meulen, J. J., 2001, "Nitric oxide flow tagging in unseeded air," Optics Letters, 26(1), pp. 36-38.
[98] van der Laan, W. P. N., Tolboom, R. A. L., Dam, N. J., and ter Meulen, J. J., 2003, "Molecular tagging velocimetry in the wake of an object in supersonic flow," Experiments in Fluids, 34(4), pp. 531-533.
[99] Goss, L. P., Chen, T. H., Trump, D. D., and Sarka, B., 1991, "Flow-tagging velocimetry using UV-photodissociation of water vapor," 29th AIAA Aerospace Sciences Meeting, Paper No. AIAA-1991-0335Reno, Nevada, USA,.
[100] Boedeker, L. R., 1989, "Velocity-measurement by $H_2O$ photolysis and laser-induced fluorescence of OH," Optics Letters, 14(10), pp. 473-475.
[101] Miles, R., Lempert, W., and Zhang, B., 1991, "Turbulent structure measurements by RELIEF flow tagging," Fluid Dynamics Research, 8(1-4), pp. 9-17.
[102] Miles, R. B., Grinstead, J., Kohl, R. H., and Diskin, G., 2000, "The RELIEF flow tagging technique and its application in engine testing facilities and for helium-air mixing studies," Measurement Science & Technology, 11(9), pp. 1272-1281.
[103] Noullez, A., Wallace, G., Lempert, W., Miles, R. B., and Frisch, U., 1997, "Transverse velocity increments in turbulent flow using the RELIEF technique," Journal of Fluid Mechanics, 339, pp. 287-307.
[104] Ress, J. M., Laufer, G., and Krauss, R. H., 1995, "Laser ion time-of-flight velocity-measurements using $N_2^+$ tracers," AIAA Journal, 33(2), pp. 296-301.
[105] Michael, J. B., Edwards, M. R., Dogariu, A., and Miles, R. B., 2011, "Femtosecond laser electronic excitation tagging for quantitative velocity imaging in air," Applied Optics, 50(26), pp. 5158-5162.
[106] Hsu, A. G., Srinivasan, R., Bowersox, R. D. W., and North, S. W., 2009, "Molecular tagging using vibrationally excited nitric oxide in an underexpanded jet flowfield," AIAA Journal, 47(11), pp. 2597-2604.
[107] Lahr, M. D., Pitz, R. W., Douglas, Z. W., and Carter, C. D., 2010, "Hydroxyl-tagging-velocimetry measurements of a supersonic flow over a cavity," Journal of Propulsion and Power, 26(4), pp. 790-797.
[108] Engel, V., Staemmler, V., Vanderwal, R. L., Crim, F. F., Sension, R. J., Hudson, B., Andresen, P., Hennig, S., Weide, K., and Schinke, R., 1992, "Photodissociation of water in the 1st absorption-band: a prototype for dissociation on a repulsive potential energy surface," Journal of Physical Chemistry, 96(8), pp. 3201-3213.
[109] Yuan, K., Cheng, Y., Cheng, L., Guo, Q., Dai, D., Wang, X., Yang, X., and Dixon, R. N., 2008, "Nonadiabatic dissociation dynamics in $H_2O$: Competition between rotationally and nonrotationally mediated pathways," Proceedings of the National Academy of Sciences of the United States of America, 105(49), pp. 19148-19153.

[110] Yuan, K., Cheng, Y., Cheng, L., Guo, Q., Dai, D., Yang, X., and Dixon, R. N., 2010, "Quantum state-selected photodissociation dynamics of $H_2O$: Two-photon dissociation via the C˜ electronic state," Journal of Chemical Physics, 133(13).
[111] Kulatilaka, W. D., Lucht, R. P., Hanna, S. F., and Katta, V. R., 2004, "Two-color, two-photon laser-induced polarization spectroscopy (LIPS) measurements of atomic hydrogen in near-adiabatic, atmospheric pressure hydrogen/air flames," Combustion and Flame, 137(4), pp. 523-537.
[112] Nielsen, C. B., Rettrup, S., and Sauer, S. P. A., 2006, "Two-photon absorption cross sections: An investigation of the accuracy of calculated absolute and relative values," Journal of Chemical Physics, 124(11), p. 12.
[113] Nikogosyan, D. N., Oraevsky, A. A., and Rupasov, V. I., 1983, "Two-photon ionization and dissociation of liquid water by powerful laser UV radiation," Chemical Physics, 77(1), pp. 131-143.
[114] Luque, J., and Crosley, D. R., 1999, "LIFbase: Database and spectral simulation."
[115] Goodwin, D., 2005, "*Cantera: Object-Oriented Software for Reacting Flows*,"California Institute of Technology, available at http://www.cantera.org.
[116] Ramsey, M. C., and Pitz, R. W., 2011, "Template matching for improved accuracy in molecular tagging velocimetry," Experiments in Fluids, 51(3), pp. 811-819.
[117] Zwart, P. J., Budwig, R., and Tavoularis, S., 1997, "Grid turbulence in compressible flow," Experiments in Fluids, 23(6), pp. 520-522.
[118] Briassulis, G., Agui, J. H., and Andreopoulos, Y., 2001, "The structure of weakly compressible grid-generated turbulence," Journal of Fluid Mechanics, 432, pp. 219-283.
[119] Mazellier, N., Danaila, L., and Renou, B., 2010, "Multi-scale energy injection: a new tool to generate intense homogeneous and isotropic turbulence for premixed combustion," Journal of Turbulence, 11(43), pp. 1-30.
[120] Kurian, T., and Fransson, J. H. M., 2009, "Grid-generated turbulence revisited," Fluid Dynamics Research, 41(2), p. 32.
[121] Gad-el-Hak, M., and Corrsin, S., 1974, "Measurements of nearly isotropic turbulence behind a uniform jet grid," Journal of Fluid Mechanics, 62(JAN8), pp. 115-&.
[122] Avidor, J. M., Kemp, N. H., and Knight, C. J., 1976, "Experimental and theoretical investigation of flow generated by an array of porous tubes," AIAA Journal, 14(11), pp. 1534-1540.